Vertically and Horizontally Self-assembled Magnetoelectric Heterostructures with Enhanced Properties for Reconfigurable Electronics

Xiao Tang

Dissertation submitted to the faculty of the Virginia Polytechnic Institute and State University in partial fulfillment of the requirements for the degree of

Doctor of Philosophy

In

Material Science and Engineering

Dwight D. Viehland, Chair

Jiefang Li

Alex O. Anning

Guo Quan Lu

November 15th 2019

Blacksburg, VA

Keywords: nanostructure, integrated heterostructure, magnetoelectric

Vertically and Horizontally Self-assembled Magnetoelectric Heterostructures with Enhanced Properties for Reconfigurable Electronics

Xiao Tang

ABSTRACT

Magnetoelectric (ME) materials are attracting increasing attention due to the achievable reading/writing source (electric field and magnetic field in most cases), fast response time, and larger storage density. Therefore, nanocomposites featuring both magnetostriction and piezoelectricity were investigated to increase the converse magnetoelectric (CME, α) coefficient. Among all the nanocomposites, vertically/horizontally-integrated heterostructures were investigated; these materials offer intimate lattice contact, lower clamping effect, dramatically enhanced α, easier reading direction, and the potential to be patterned for complicated applications.

In the present work, we focused on three principal goals: (a) creating two-phase vertically integrated heterostructures with different ME materials that provide much larger α, and enhanced strain-induced magnetic shape anisotropy compared with the single-phased ME nanomaterials; (b) creating a vertically integrated heterostructure with large α, lower loss, and higher efficiency; and (c) investigating the stable magnetization states that this heterostructure could achieve, and how it can be used in advanced memory devices and logic devices.

Firstly, a $BiFeO_3$-$CoFe_2O_4$ (BFO-CFO) heterostructure was epitaxially deposited on $Pb(Mg_{1/3}Nb_{2/3})O_3$-x at%$PbTiO_3$ (PMN-xPT). The resulting PMN-xPT was proven to have a large piezoelectric effect capable of boosting the CME in the heterostructure to create a much higher α.

Secondly, a novel material, $CuFe_2O_4$ (CuFO), featuring lower coercivity and loss, was chosen to be self-assembled with BFO. This low-loss could increase the efficiency of the ME effect. Also, our findings revealed a much larger α in the vertically integrated heterostructure compared to single-layer CuFO. Accordingly, the self-assembled structure represents a convenient method for increasing the CME in multiferroic materials.

Thirdly, the magnetization states for all these vertically integrated heterostructures were studied. Note that vertically integrated heterostructures are typically fabricated using materials with volatile properties. However, these composites have shown a non-volatile nature with a multi-states ($N \geq 4$), which is favored for multiple applications such as multi-level-cell.

Moreover, several self-assembled heterostructures were created that are conducive to magnetic anisotropy/coercivity manipulation. One such example is $Ni_{0.65}Zn_{0.35}Al_{0.8}Fe_{1.2}O_4$ (NZAFO) with BFO, which forms a self-assembled nanobelt heterostructure that exhibits high induced magnetic shape anisotropy, and is capable of manipulating magnetic coercivity (from 2 Oe to 50 Oe) and magnetic anisotropy directions (both in-plane and out-of-plane).

Finally, we deposited a $SrRuO_3$-$CoFe_2O_4$ (SRO-CFO) vertically integrated composite thin film on the single crystal substrate PMN-30PT, with a CFO nanopillar and SRO matrix. In such a heterostructure, the SRO would serve as the conductive materials, while CFO offers the insulated property. This unique conductive/insulating heterostructure could be deposited on PMN-PT single crystals, thus mimicking patterned electrodes on the PMN-PT single crystals with enhanced dielectric constant and d_{33}.

Vertically and Horizontally Self-assembled Magnetoelectric Heterostructures with Enhanced Properties for Reconfigurable Electronics

Xiao Tang

GENERAL AUDIENCE ABSTRACT

Multi-ferroic materials, which contain multiple ferroic orders like ferromagnetism/ferroelectricity order, were widely studied nowadays. These orders are coupled together, which could manipulate one order via another one through the coupling. Due to the achievable reading/writing source (electric field and magnetic field in most of the case), fast response time and larger storage density, magnetoelectric (ME) materials aroused most interests to-date. To be used in different applications, such as memory devices and logic devices, a high transfer efficiency, or say a high coupling coefficient, is required. However, single-phase materials have nearly neglectable ME effect. Therefore, a nanocomposite that contents both magnetostriction and piezoelectricity were investigated to increase the converse magnetoelectric (CME, α) coefficient. Amongst all the nanocomposite, a vertically integrated heterostructure was revealed, which has intimate lattice contact, lower clamping effect, dramatically enhancedα, easier reading direction, and potential to be patterned for complicated applications.

In this present work, we focused on several different aspects: (a) creating two-phase vertically integrated heterostructure with different ME materials, which provides much larger α, large strain-induced magnetic shape anisotropy comparing with the single-phased ME nanomaterials; (b): creating a vertically integrated heterostructure with large α and lower losses and higher efficiency; (c) investigate the stable magnetization states that this

heterostructure could achieve, which shows the potential of being used in advanced memory devices and logic devices.

Firstly, in this work, a $BiFeO_3$-$CoFe_2O_4$ (BFO-CFO) heterostructure was epitaxially deposited on the $Pb(Mg_{1/3}Nb_{2/3})O_3$-x at%$PbTiO_3$ (PMN-xPT), which could boost the CME in the heterostructure to create a much higher α. Then, a novel materials $CuFe_2O_4$ (CuFO), was chosen to be self-assembled with BFO, which has lower losses and higher efficiency of the ME effect.

Secondly, several self-assembled heterostructures were created, such as $Ni_{0.65}Zn_{0.35}Al_{0.8}Fe_{1.2}O_4$ (NZAFO) with BFO, which manipulated the magnetic coercivity (from 2 Oe to 50 Oe) and magnetic anisotropy directions (Both in-plane and out-of-plane). And a heterostructure: $SrRuO_3$ with CFO, created a vertically integrated heterostructure, could be used as patterned electrodes in different applications.

Moreover, magnetization states were studied in all these vertically integrated heterostructures. A multi-states ($N \geq 4$) was revealed, which was favored by multiple applications such as multi-level-cell or logical devices.

Finally, we deposited a $SrRuO_3$-$CoFe_2O_4$ (SRO-CFO) vertically integrated composite thin film on the single crystal substrate PMN-30PT, with a CFO nanopillar and SRO matrix. In such a heterostructure, the SRO would serve as the conductive materials, while CFO offers the insulated property. This unique conductive/insulating heterostructure could be deposited on PMN-PT single crystals, thus mimicking patterned electrodes on the PMN-PT single crystals with enhanced dielectric constant and d_{33}.

ACKNOWLEDGMENTS

Firstly, I would thank my advisors, Dr. Dwight Viehland and Dr. Jiefang Li for giving this precious opportunity to work at Virginia Tech. And, I am wholeheartedly grateful for their support, both mentally and financially. Without these supports, I cannot finish my projects easily.

I would also give my gratitude to Dr. Viehland for his professional advises and guidance for my project and dissertations. Dr. Viehland, not only provides his wisdom and thoughts during the research period but also provides his suggestions of attitudes and passions for the work that I have done. I have been inspired so much during the study in his group.

I really appreciate the help from Dr. Li, who is specialized in the experimental equipment and designs helped a lot for my projects. Also, her propounding thoughts help me to enhance the skills of scientific knowledge.

I would also thanks Dr. Alex Aning, Dr. Guo-Quan Lu, who is my committed member, for their encouragement, support, and suggestions.

Also, Dr. Chung Ming Leung provided so many useful technical suggestions about the applications of the project.

I would also like to thank Min Gao and Junran Xu, my colleagues at Virginia Tech, who give many scientific and life supports during the time period of my study.

Finally, I am especially grateful to my mother, who gives warm support for me to study aboard. Thanks to her kindhearted mental support, I could study at Virginia Tech without any hesitation.

Table of Contents

LIST OF FIGURES

LIST OF TABLES

CHAPTER 1: INTRODUCTION

1.1. Multiferroic Materials.

Ferroic orders, including ferroelectrics, ferromagnetic and ferroeleastics, are critical to ferroic materials[1], as shown in Figure 1.1[2]. Multiferroic materials continue to attract attention for their tremendous applications potential in the information industry—notably, for use in multi-state information storage devices and new types of sensors. Indeed, they are widely studied for use in a variety of applications[1,3-6]. Multiferroic materials facilitate the transference of different energies between different orders, which could create a tuning effect through the use of different input sources[7]. Therefore, investigating multiferroic materials with strong coupling behaviors will be important for the development of micro devices such as microelectromechanical systems (MEMS) devices and high-density information storage media, to name a few.

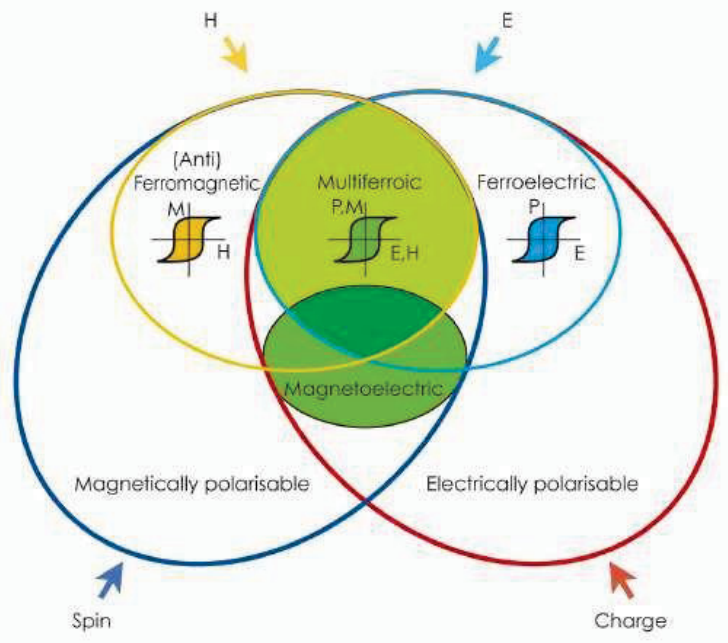

Figure 1.1. Multi-ferroric orders. Galdi, A. Magnetic, orbital and transport properties in LaMnO3 based heterostructures, Université de Caen; Università degli studi di Salerno, (2011), with fair use.

1.1.1. Definition, advantages, and applications.

Multiferroic materials refer to a special class of materials that simultaneously possess two or more ferroic-order parameters (e.g., magnetic, electric or piezo-elastic), thereby providing an effective way for controlling magnetism by electric fields[8]. These different orders can be coupled between each other, which creates a tuning effect between different input sources[3], as shown in Figure. 1.2[6]. These twinned or even tripled orders could be forced to switch to another equivalent state by a driving input source[9] such as an electric field (E)[10], a magnetic field (H)[11], or via the application of mechanical stress (σ)[12]. Thus, with the heightened interest in the potential of multiferroic materials, researchers are examining the impact of antiferroic ordering, as evidenced in the antiferromagnetic materials[9].

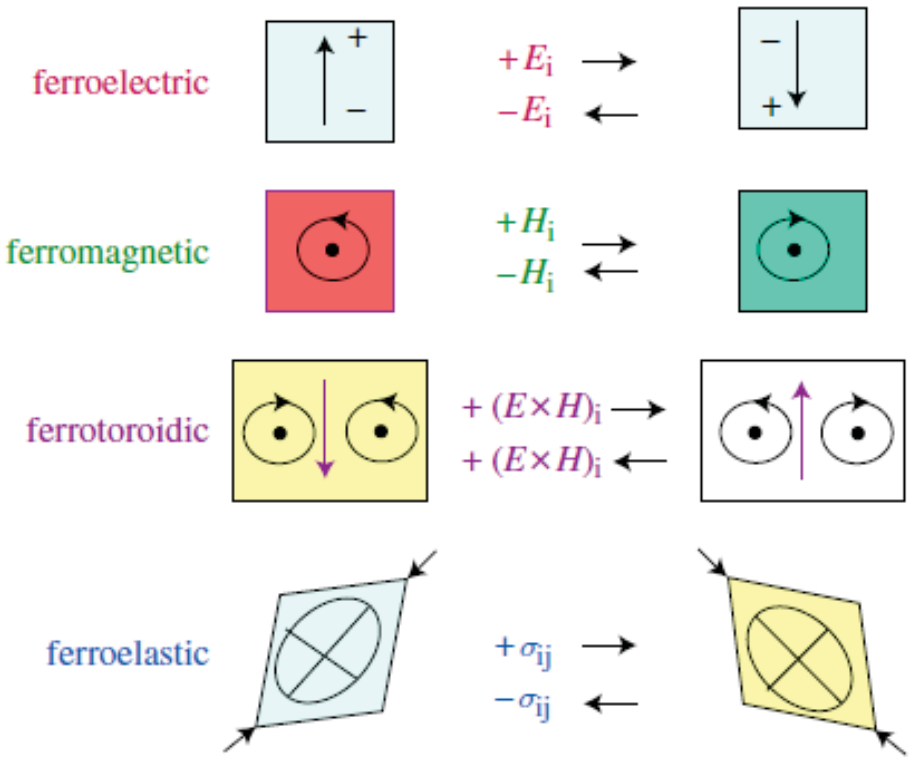

Figure 1.2. Different ferroric orders and the input sources of control. Velev, J. P., Jaswal, S. S. & Tsymbal, E. Y. Multi-ferroic and magnetoelectric materials and interfaces. Philos Trans A Math Phys Eng Sci 369, 3069-3097, with fair use.

Multiferroic materials feature specific characteristics—principally having to do with their structure and symmetry requirements[9,13]. In particular, the structure of multiferroic materials must feature a magnetic interaction between the element ions within the lattice structure[14]. This magnetic interaction facilitates the exchange interaction of magnetic orders, which results in the coupling effect[15]. The symmetry group of multiferroic materials requires a non-central symmetric lattice structure with spontaneous polarization[16] (shown in Fig. 1.3[17]), which can potentially be driven by the input of different sources[9].

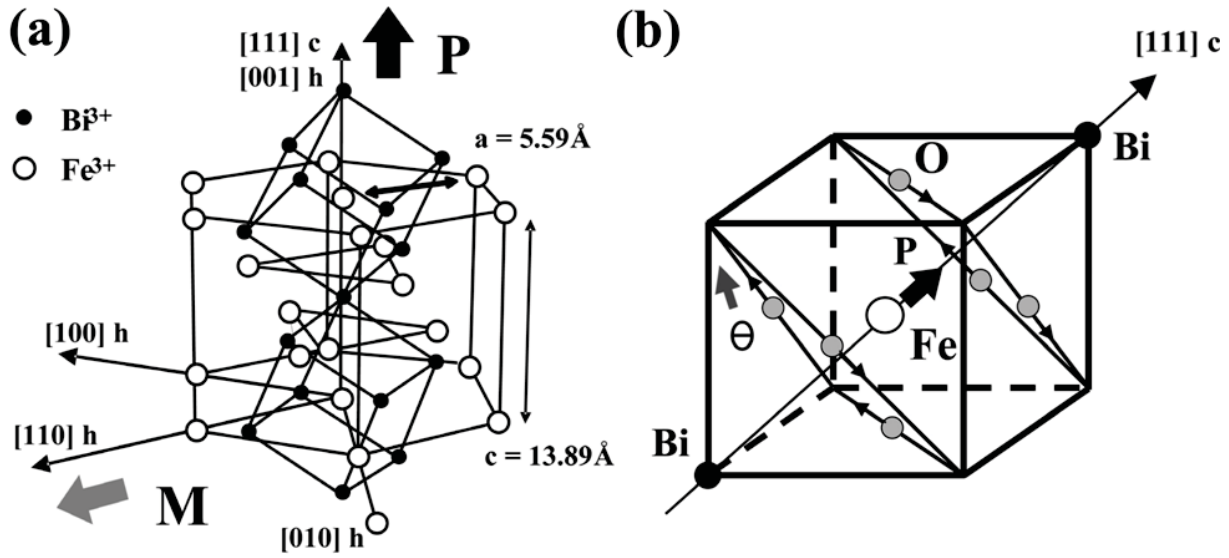

Figure 1.3. $BiFeO_3$ lattice with spontaneous polarization, showing a piezoelectric effect. Jeong, Young Kyu, et al. "R3c-R3m octahedron-tilting transition in rhombohedrally-distorted BiFeO3 multiferroics." Journal of the Korean Physical Society 58.4 (2011): 817-820, with fair use.

Multiferroic materials feature numerous advantages, such as control of fields with no media requirements[11,18], enhanced longevity[19], rapid read/write speed[20], low power consumption (passive)[21], quick response times[22] and different magnetic states[23]. These advantages increase the potential of multiferroic material to be used in wide range of applications. These include their incorporation in memory devices such as electric-field-controlled magnetic random access memory[24]—or to be more specific, in field-controlled magnetoelectric (ME) random access memory (MeRAMs)[20]—in logic devices[25], and even in synapse-like learning devices[26]. Well before these advanced applications became known, researchers and engineers have long been interested in the complex interplay between magnetism and electricity and how to put it to work in actual class of materials—the multiferroics[27-32]. The original concept of the multiferroic materials was defined in the 1860s by James Maxwell, a pioneer of electromagnetism, and in the four seminal equations that now bear his name[33]. Later, Hulin et al.[32] investigated the coupling

interactions between ferromagnetic and ferroelectric orders. Just a half-century later, Dzyaloshinskii et al.[30] developed a physics model that described the coupling of different orders, which is known as the Dzyaloshinskii-Moriya interaction. From then on, the exploration of materials with multiferroic properties exploded. By following predictions based on the physics model, several single-phase multiferroic materials were identified, such as Cr_2O_3 by Astrov et al.[29] and Folen et al.[31]. One can credit Schmid et al.[9] for isolating the ferromagnetoelectric material, Ni-I Boracite. While advances in multiferroic studies were slow to take root due to the time-consuming process of identifying suitable materials, such studies began to flourish beginning in the twentieth century[34-36], which is marked by the discovery of materials such as $BiFeO_3$ (BFO)[34] and $PbTiO_3$ (PTO)[37] and $TbDyFe_2$ (TDF)[38]. Spurred on by increasingly sophisticated fabrication techniques, more and more multiferroic materials have been developed and investigated.

1.1.2. Magnetoelectricity.

Among all the ferroic orders, one combination rises to the top due to its many advantages. As proposed by Hulin et al[32], this combination refers to the coupling between the ferromagnetic and ferroelectric orders. These two orders, containing the response between electric polarization P and magnetic field H, making the transformation between M and P[4]. The conversion of these two orders is known as magnetoelectricity. Accordingly, the magnetic-induced electric polarization change is known as the magnetoelectric effect (ME); and E-induced magnetization change is referred to as the converse magnetoelectric (CME) effect[39], as shown in Figure 1.4[6].

In general, ME materials are easy to fabricate for industrial applications: the induced and output of the sources are the E and H fields with no media requirements for tranportation and transferring at speed of light[5]. Additionally, magnetization changes could be non-volatile—

meaning that the magnetization level would remain constant without maintaining a driving force, which in most cases is E[40]. Moreover, in most cases, magnetization is able to stay at two or more different states, increasing its potential of being used in memory devices or even logical devices[10,23], as illustrated in Figure 1.5[23].

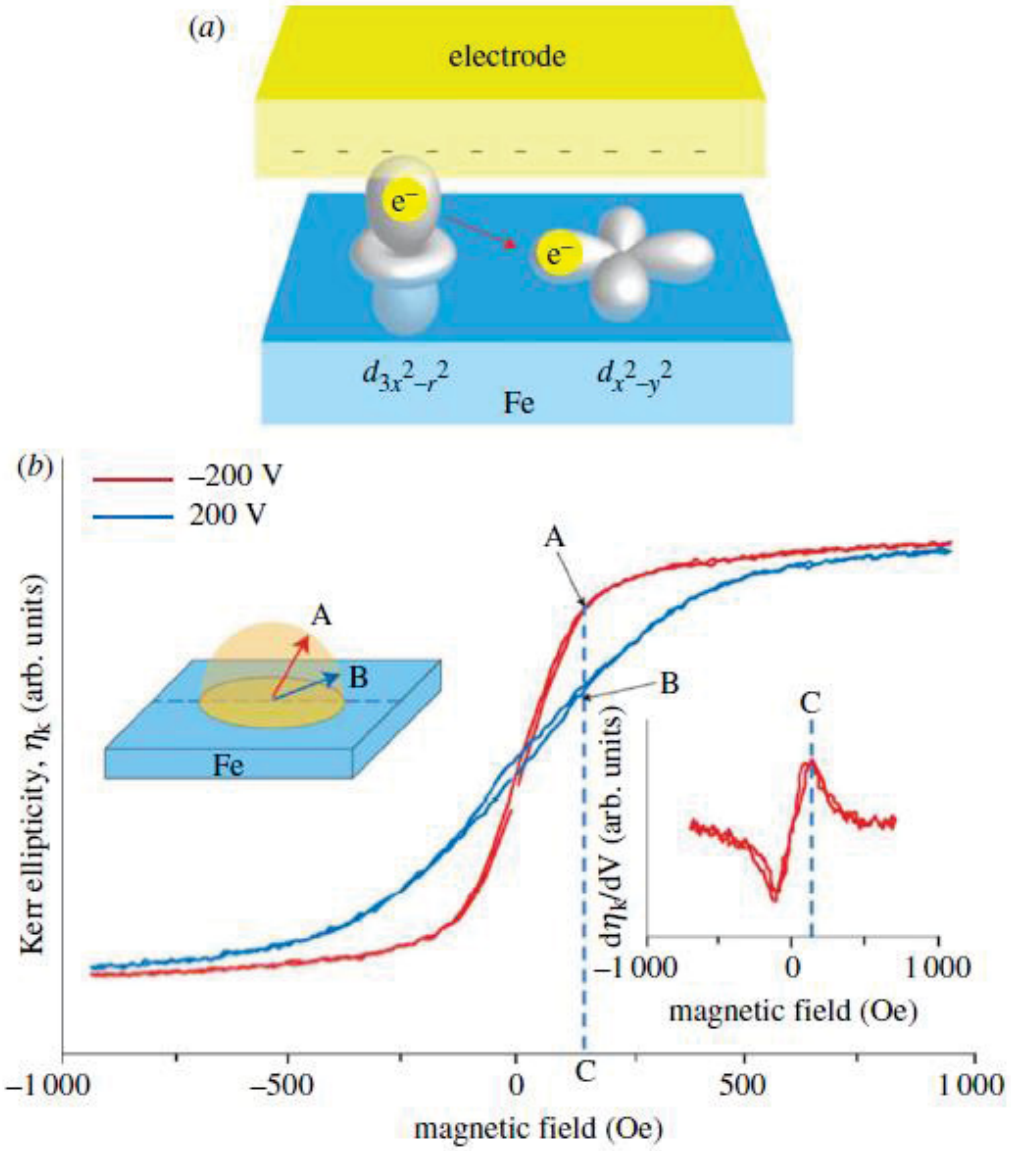

Figure 1.4. Electric field induced M-H hysteresis loop changes. Velev, J. P., Jaswal, S. S. & Tsymbal, E. Y. Multi-ferroic and magnetoelectric materials and interfaces. Philos Trans A Math Phys Eng Sci 369, 3069-3097, doi:10.1098/rsta.2010.0344 (2011), with fair use.

The theoretical model for ME effect was developed many years ago and has been intensively studied since that time. As illustrated by Eerenstein et al.[3], the driving force F could be written as:

$$-\mathrm{F}(\mathrm{E},\mathrm{H}) = \frac{1}{2}\varepsilon_0\varepsilon_{ij}E_iE_j + \frac{1}{2}\mu_0\mu_{ij}H_iH_j + \alpha_{ij}E_iE_j + \frac{\beta_{ijk}}{2}E_iH_iH_j + \frac{\gamma_{ijk}}{2}H_iE_iE_j + \cdots \quad (1.1)$$

Where ε_0 and μ_0 represent the permittivity and permeability of the free space, respectively; ε_{ij} is the second-rank tensor in non-ferroic materials; and μ_{ij} is relative permeability. In the equation, the first-term of the right hand side indicates the electrical response to E; the second term describe the contribution of H; the third term gives the free energy expansion of linear ME coupling; and the fourth term contain the high-order linear to quadratic ME coupling coefficient. These contributions together indicate the total contribution of the ME effect. From this theory, one can determine the derivative for magnetically-induced P and electrically-induced M, which is important for calculating ME coupling.

$$P_i = \alpha_{ij}H_j + \frac{\beta_{ijk}}{2}H_iH_j \quad (1.2)$$

and

$$\mu_0 M_i = \alpha_{ij}E_j + \frac{\lambda_{ijk}}{2}E_kE_j \quad (1.3)$$

In reality, P and M are mostly described by resultant rather than the field. This resultant E and H could be an estimated approximated value, which could significantly simplify the calculation.

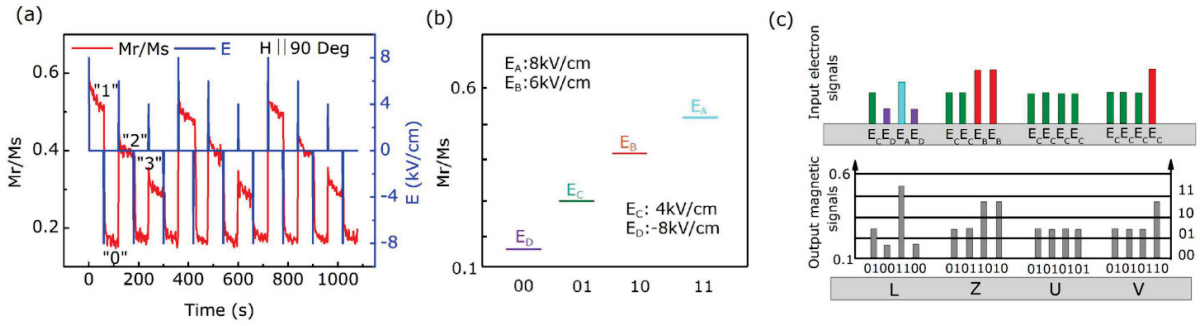

Figure 1.5. Different E-induced magnetization states, and its application as memory devices. Wei, Y. et al. Four-state memory based on a giant and non-volatile converse magnetoelectric effect in the FeAl/PIN-PMN-PT structure. Scientific Reports 6, 30002, doi:10.1038/srep30002 (2016), with fair use.

Normally, ME coupling could be described as a specific number, with a unit of $\mathrm{mV}Oe^{-1}cm^{-1}$[41], which is widely used for comparing different ME materials. However, in some cases, the direct ME effect is hard to calculate quantitatively because of the difficulty of achieving a localized H field. Conversely, the localized E field is much easier to achieve. Therefore, we selected the converse magnetoelectric effect (CME, or α_{CME}) to be used to perform the quantitative calculations, as shown in equation (1.4)[42].

$$\alpha = \mu_0 \frac{\Delta M}{\Delta E} \tag{1.4}$$

where μ_0 is the permeability of free space, and α is expressed in units of s/m. This calculation could result in numerical values for CME which then facilitate the comparison of different materials.

1.1.3. Traditional single-phase ME materials.

Although ME materials feature various advantages, the number of single-phase materials that exhibit both ferromagnetic and ferroelectric order is extremely limited[43]. And even worse, the coupling coefficient is almost negligible in single-phase ME materials[44]. Single-phase ME materials can be found in several structure classes: perovskite oxides, hexagonal manganites, orthorhombic fluorides, spinel, boracite, and others[43,44], in Table 1.1.

Table 1.1. Common single phase ME materials. AFM: anti-ferromagnetic, FM: ferromagnetic, FE: ferroelectric.

Compound	Structure	Magnetic ordering	Ferroelectric ordering
$BiFeO_3$	perovskite	AFM	FE
$Ni_3B_7O_{13}I$	boracite	AFM/FM	FE
$EuTiO_3$	perovskite	FM	FE
$TbMnO_3$	perovskite	AFM	FE
$HoMnO_3$	hexagonal	AFM	FE
YMn_2O_5	orthorhombic	AFM	FE
Fe_3O_4	inverted spinel	AFM	FE
$CoCr_2O_4$	spinel	AFM	FE
CdV_2O_4	spinel	AFM	FE

In these different classes, perovskite is the most popular class for single-phase materials[13]. Common perovskite oxides such BiFeO3 (BFO) and TbMnO3 (TMO) have been well studied in the literature, which routinely describe their weak ferromagnetic and ferroelectric orders[34-38]. In these perovskite oxides, ferroelectricity is normally afforded by the non-centrosymmetric center B-sites of the ABO_3 perovskite oxides, as illustrated in Fig. 1.3[45]. The ferromagnetic order is also provided by the B-site, which results from the partially filled spin shell of the ions[46].

Efforts are ongoing to increase ME coupling in single-phase materials. The most intuitive method for increasing ferromagnetic order is to substitute the B-site, which can create two different cation types, as illustrated as $A(B_{1-x}B'_x)O_3$, Such as $Mn(Nd_{0.7}Sr_{0.3})O_3$[47], and $Sn(Ba_xSr_{1-x})O_3$[48],

as shown in Figure 1.6[48]. These substituted ions could impact the radius average of the A position, which in turn will influence FM and AFM interactions within the crystals. Another common way for increasing ME coupling within single-phase materials is to choose a promising A-site in ABO_3 perovskite materials[46]. In particular, a strong candidate element for the A-site is Pb[49] because it is easily polarized, such as $\mathrm{Pb}(Fe_{2/3}W_{1/3})O_3$[49].

However, even after implementing these ion modifications within the lattice, the ME coupling effect is still unacceptably weak[50,51], only 1-20 $\mathrm{mV}Oe^{-1}cm^{-1}$. This approach is impractical for most applications due to weak coupling effects: the generated signals are undetectable in this case. This means that single-phase ME materials are generally unsuitable for most ME coupling studies and devices. In contrast, the coupling effects between FM and FE orders give these materials a bright future. In summary, a method is needed to dramatically increase ME coupling to replace single-phase materials.

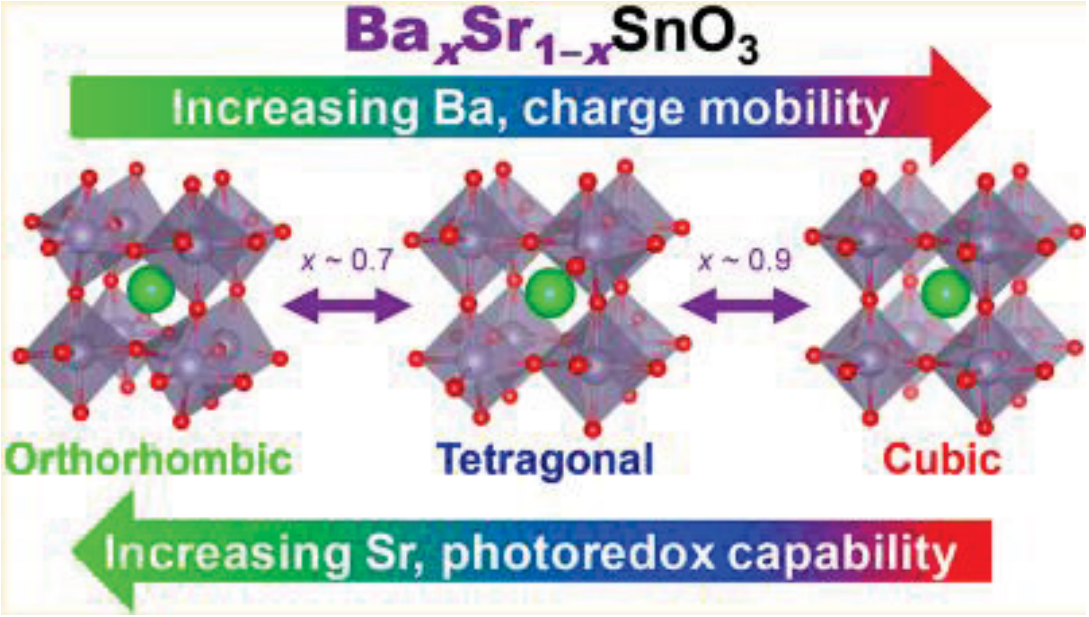

Figure 1.6. Sr substituted BaSnO3 perovskite. Wong Z M, Cheng H, Yang S W, et al. Computational Design of Perovskite Ba x Sr1–x SnO3 Alloys as Transparent Conductors and Photocatalysts[J]. The Journal of Physical Chemistry C, 2017, 121(47): 26446-26456, with fair use.

1.1.4. Multi-phase ME materials with different heterostructures

Because ME coupling in single-phase materials is almost negligible, a new method must be developed to significantly increase the ME coefficient for various applications and studies. Because the FE and FM orders are generally weak in single-phase materials, composites that feature strong FE and FM orders was proposed, and a large ME effect was expected for these composites. As shown in Figure 1.7[52], a magnetostrictive layer was bonded with another piezoelectric layer. When the E or H field excites the corresponding FM/FE layer, strain was generated and then transferred to another layer to create an ME response output via the bond layer. This significantly increases the ME coupling coefficient, from 1-20 mV$Oe^{-1}cm^{-1}$ in single-phase materials to about 100 mV$Oe^{-1}cm^{-1}$ reported[53].

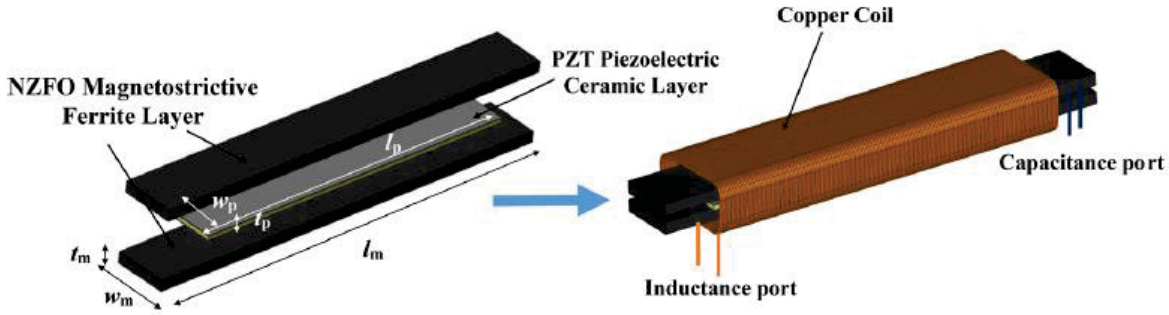

Figure 1.7. Composites that contain both FE and FM materials. Leung, C. M. et al. Highly efficient solid-state magnetoelectric gyrators. Applied Physics Letters 111, 122904, doi:10.1063/1.4996242 (2017), with fair use.

In these laminated composites, the ME effect can be determined by the produce tensor property[4], as shown in the equation below:

$$ME_{H\,effect} = \frac{magnetic}{mechanical} \times \frac{mechanical}{electric} \tag{1.5}$$

$$ME_{E\,effect} = \frac{eletric}{mechanical} \times \frac{mechanical}{magnetic} \tag{1.6}$$

Therefore, the ME effect in these laminated composite is an extrinsic property instead of an intrinsic property for single-phase materials. Accordingly, the ME coefficient depends on the microstructure and interaction across the sample. However, the bonding layer could significantly dissipate the strain transformation, therefore limiting the ME coefficient. In order to solve this problem, a new laminate technique was proposed, which is known as epitaxially growth laminate structure. This epitaxial growth layer facilitates the growth of an FM layer lattice-by-lattice on the surface of the FE layer, or vice-versa[54], as shown in Figure 1.8[6]. This approach affords significantly

more intimate contact between the FE and FM layers, creating more efficient strain transformation, and therefore, a much larger ME coefficient, ~ 400 mV$Oe^{-1}cm^{-14}$.

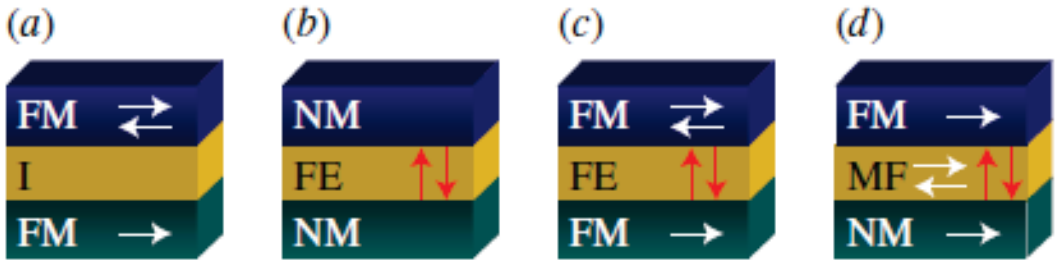

Figure 1.8. Epitaxially growth FM and FE laminate composites. Velev, J. P., Jaswal, S. S. & Tsymbal, E. Y. Multiferroic and magnetoelectric materials and interfaces. Philos Trans A Math Phys Eng Sci 369, 3069-3097, doi:10.1098/rsta.2010.0344 (2011) , with fair use.

Various epitaxial growth nanocomposites have been reported, such as multi-layer (labeled as 2-2), particles in matrix (labeled as 0-3), and vertically integrated nanopillars (labeled as 1-3 or 3-1)[55-59], as shown in Figure 1.9, (a)-(c)[4]. However, (2-2) and (0-3) heterostructures often suffer from several disadvantages, notably clamping effects and large leakage currents[10]. Accordingly, the (1-3) heterostructure is favored for scientific and industrial purposes due to dramatically smaller clamping effect.

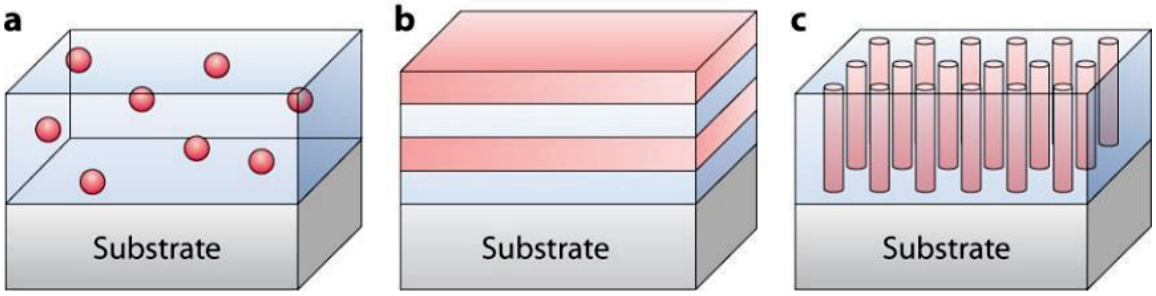

Figure 1.9. Several epitaxial growth nanocomposites. From (a)-(c): (0-3), (2-2) and (1-3). Nan, C. W., Bichurin, M. I., Dong, S. X., Viehland, D. & Srinivasan, G. Multiferroic magnetoelectric composites: Historical perspective, status, and future directions. Journal of Applied Physics 103, 031101, doi:Artn 031101, with fair use.

1.1.5. Self-assembled (1-3)/(3-1) heterostructures

The (1-3) structures have aroused significant attention from both scientific researchers and industrial developers. Vertically-integrated nanopillar heterostructures that combine magnetostrictive and piezoelectric phases have been found to possess significant ME couplings[58,60]. Moreover, these heterostructures provide a much larger contact area between the matrix and nanopillar phases, allowing for intimate lattice contact and significantly reduced clamping effects with substrates[39,61]. This type of (1-3) heterostructure uses the transfer of strain between piezoelectric and magnetostrictive phases to enlarge the E-field dependence of the magnetization (M)[39]. Vertically integrated (1-3) heterostructures also feature high magnetic shape anisotropy because of their nanopillar geometry[45].

Previously[45], the nanopillar structure of BFO-CFO vertically integrated layers was shown to pin the rotation of magnetic domains possibility for N>2 remnant magnetization states. In fact, there have been reports of N≥ 4 different magnetic states in BFO-CFO/PMN-PT upon removal of E[10,39,62,63]. This pinned domain rotation can result in non-volatile magnetization in CFO nanopillars.

When the composition of PT in PMN-PT crystal locates near the morphotropic phase boundary (MPB), the volatile properties become unpredictable. For example, single CFO layers deposited on PMN-30PT have been shown to display volatile magnetization changes[63], in contrast, Mn-doped CFO deposited on PMN-30PT exhibits non-volatile changes[64]. The unpredictability of these induced property changes hinders their potential for industrial applications. As noted in the literature, BFO-CuFO on PMN-33PT[65] and BFO-CFO on PMN-30PT[66] exhibit non-volatile changes. We attribute this outcome to the fact that PMN-33PT and PMN-30PT are close to the MPB; thus, such (1-3) heterostructures might display non-volatility, even though they consist of phases that individually feature volatile ones.

There are several methods used to fabricate (1-3) or (3-1) heterostructures. In the traditional approach, Li et al.[67] used focused ion beam (FIB) to deposit an AO layer on top of the BFO layer. Then, the researchers attached a regular hole-array that was cut by the FIB, after which a layer of nanosized cobalt ferrite ($CoFe_2O_4$) particles was deposited on top. Finally, the pattern and surplus CFO was dissolved using an NaOH solution. The entire process is shown in Figure 1.10[67]. Similarly, photolithography was been used to etch the pattern on the surface and then deposit the materials[68].

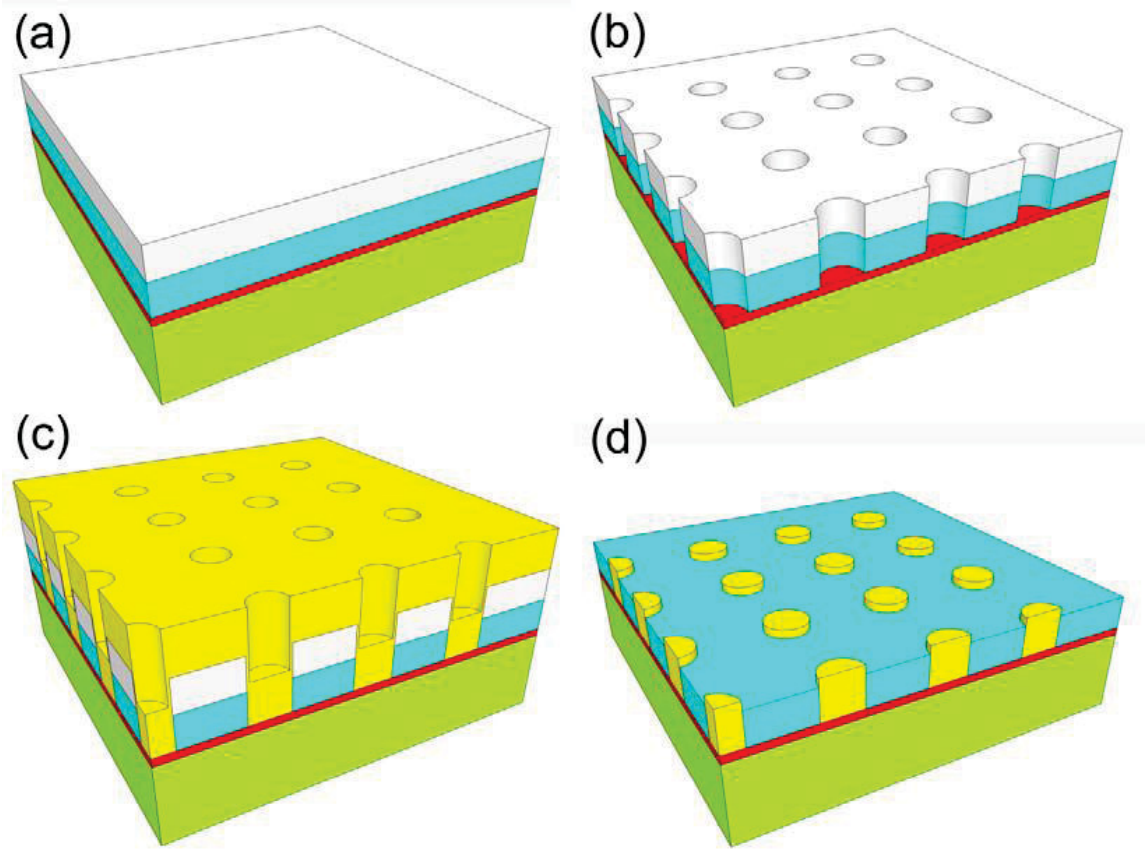

Figure 1.10. Flow chart of patterned ME composite. Yan, L. Two phase magnetoelectric epitaxial composite thin films, Virginia Tech, (2009), with fair use.

The downside is that these methods suffer from a range of drawbacks: the high cost for the fabrication, the long duration for the fabrication time, and the fact that the intimate contact between the matrix and nanostructures may be damaged. Therefore, a new method was proposed involving self-assembled heterostructures[69,70]. As indicated by the name, this method does not require any specific manufacturing procedures, as in the FIB-patterned method. For some perovskite and spinel materials such as BFO and CFO, the intrinsic lattice parameters are rather similar, resulting in the possibility of epitaxial compatibility. And due to the wettability and surface energy of these

two different materials, they will automatically segregate and form a nanopillar embedded in a matrix along the (100) direction[71], or nanobelt embedded in matrix along the (110) direction[72].

In summary, the (1-3) or (3-1) heterostructures are appropriate for numerous applications requiring multiple magnetic states, and are compatible for a wide variety of materials. Accordingly, for this investigation, (1-3) heterostructures were used to fabricate composites with a significantly higher ME coefficient, more stable magnetic states, better aligned anisotropy due to the induced shape and geometry, and wider application usage. Moreover, we developed self-assembled heterostructures using different materials, thereby creating multiple nanopillar/nanobelt heterostructures. This heterostructure was characterized and measured for a range of different properties. These (1-3) composites demonstrated very high ME coupling in the BFO-CFO heterostructures, maintained a desirable balance between high magnetostriction and low losses in BFO-$CuFe_2O_4$ (CuFO) / BFO- $Ni_{0.65}Zn_{0.35}Al_{0.8}Fe_{1.2}O_4$ (NZAFO) composites, and demonstrated the potential to be used for memory devices such in a multi-level-cell.

1.2. Materials in This Work

1.2.1. PMN-PT substrate crystals.

As already noted, ferroelectric materials play an important role in the fabrication of ME composites. Indeed, the higher ME-coupling multiferroic composites requires materials with both a large piezoelectric effect and a large magnetostrictive effect. This means that a large piezoelectric coefficient (d_{33}) and electromechanical coupling coefficient (k_{33}) are required for a larger piezoelectric effect. To date, piezoelectric materials with high d_{33} have been widely studied. Materials containing lead (Pb), as stated above, have a potentially higher piezoelectric response due to the easily polarized A-site[49]. Therefore, a growing body of research is focusing on the study

of lead-based piezoelectric materials, such as $PbZrTiO_3$ (PZT)[73,74]. PZT is a material with large spontaneous polarization, and therefore features large piezoelectric and electromechanical coupling coefficients. However, PZT suffers from degradation effects in certain applications[73], and the longevity of PZT thin films is questionable[74]. In the 1980s, $Pb(Mg_{1/3}Nb_{2/3})\ O_3$ (PMN) was investigated with a larger d_{33}[75]. However, the break down strength of this PMN material is rather small[76], making it challenging to be used in applications. Therefore, a new $PbTiO_3$ (PT)-doped PMN was developed that exhibited both dramatically enhanced d_{33} and a relatively long lifetime[77,78]. Moreover, by controlling the concentration of PT in the PMN-PT, the piezoelectric constant could be manipulated due to the fact that the structure phase of the PMN-PT was altered.

Morphotropic phase boundary (MPB) refers to the phase transition between the tetragonal and the rhombohedral ferroelectric phases as a result of varying the composition or as a result of mechanical pressure[78]. Near the MPB of 30-35 at% PT in PMN-PT materials, the structural phase may be mixed. When an E field is applied, the PMN-PT phase is able to shift from rhombohedral (R) to tetragonal (T), creating a large piezoelectric effect[62], as shown in Figure 1.11[78]. This composition manipulation not only provides a larger d_{33}, but can also alter other properties of the PMN-PT, such as volatility. PMN-PT is reported to be volatile when at% PT was less than 32%, and reported to be non-volatile when at%>35%[78]. The fact that PMN-PT can be customized for advanced industrial applications increases its attractiveness.

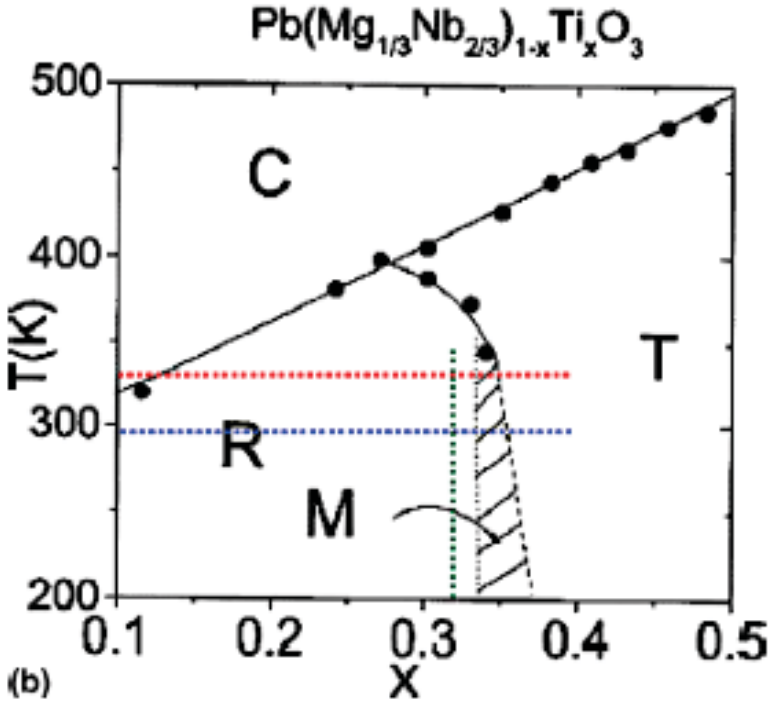

Figure 1.11. Phase diagram of PMN-PT materials. McLaughlin, E. A., Liu, T. & Lynch, C. S. Relaxor ferroelectric PMN-32%PT crystals under stress and electric field loading: I-32 mode measurements. Acta Materialia 52, 3849-3857, doi:10.1016/j.actamat.2004.04.034 (2004), with fair use.

The PMN-PT piezoelectric materials demonstrate a high piezoelectric response. Accordingly, researchers have shown that when a magnetostrictive layer was epitaxially deposited on a PMN-PT substrate, a nanocomposite with large ME coupling effect was created[63]. PMN-PT also can be fabricated as single-crystal materials[79], which means that PMN-PT is also suitable for use in the epitaxial growth method. Moreover, PMN-PT shares a similar lattice parameter with common magnetostrictive spinel materials such as CFO and NZFO. Given the many advantages of PMN-

PT, it shows potential for use in non-volatile memory devices or in volatile random access memory (RAM). As such, PMN-PT the potential to become a universal material for ME materials.

1.2.2. $BiFeO_3$ perovskite.

According to the literature, BFO perovskites demonstrate both the piezoelectric effect and the magnetostrictive effect with an ABO_3 structure[70,80]. As shown in Figure 1.12, the piezoelectric response of BFO is somewhat negligible[69], especially when compared to other materials (notably PMN-PT) in previous section. BFO is a perovskite material with a rhombohedral (R) structure[10]. Because the α, β, and γ value are pretty close to 90°, BFO can be considered to be a nearly cubic structure, which is known as pseudocubic[11]. BFO has a lattice parameter of 3.96Å, and the ferroelectric properties are associated with Bi ion displacement[80]. The ferroelectric polarization lies along the <111> direction, which is the diagonal of the lattice.

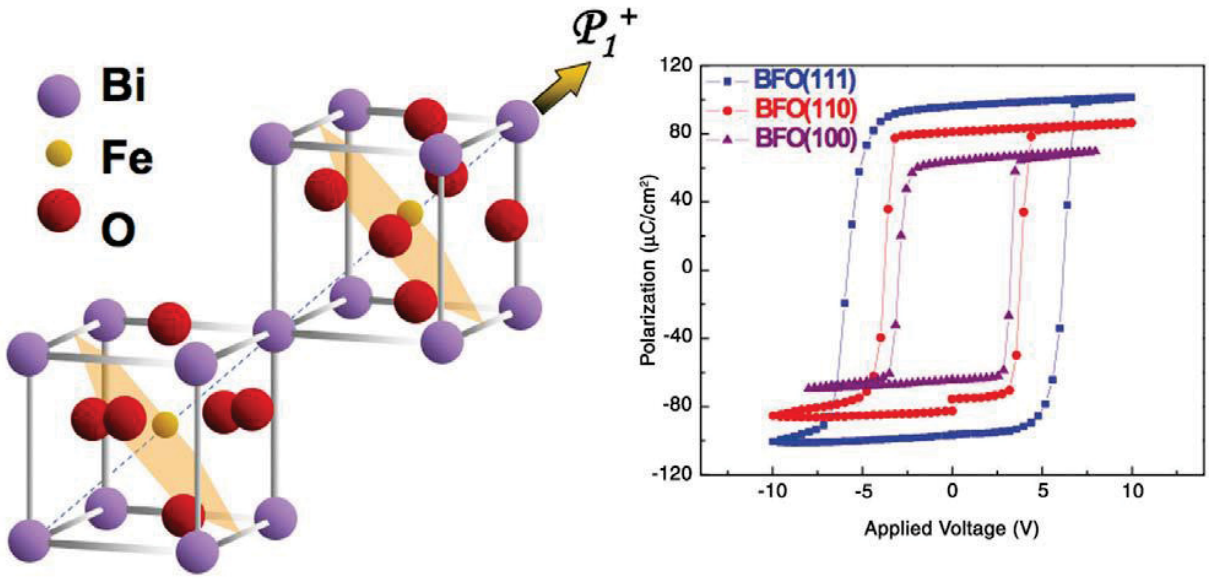

Figure 1.12. The structure of BFO and piezoelectric resonance of BFO thin film. Chu, Y.-H., Martin, L. W., Holcomb, M. B. & Ramesh, R. Controlling magnetism with multiferroics. Materials Today 10, 16-23 (2007) , with fair use.

Recent studies have attempted to use the ferroelectric effect of BFO by combing it with magnetostrictive materials—for example, CFO or NZFO—to create a large ME coupling effect. To date, several approaches incorporating BFO/CFO bi-layer laminates have been investigated[81,82]. The presence of this bilayer enhances the possibility of achieving a high ME coupling coefficient. On the downside, however, this method suffers from the clamping effect, which considerably decreases the coupling between FE and FM layers, resulting in a significantly reduced ME coefficient[18]. To increase the coefficient, the use of self-assembled (1-3) structures of BFO and CFO has been investigated[58,59,70]. Notably, (1-3) or (3-1) heterostructures provide significantly higher magnetic anisotropy, which makes ME coupling more promising. The reported CME is about 10^{-10} s/m BFO-CFO/STO[83]. Moreover, the BFO matrix when compared with the PMN-PT substrates still shows a nearly negligible piezoelectric response.

Prior studies have involved depositing BFO-CFO on STO, which merely provides the lattice match with the BFO-CFO, but has no impact on the piezoelectric response. As such, the piezoelectric response of the heterostructure completely relies on the BFO matrix, which is minimal. Due to the thickness of BFO-CFO heterostructures, when an E-field was applied on the thin film, serval leakage current were produced that hindered the enhancement of the ME coupling of BFO-CFO/STO. Wang et al.[66] previously reported a CFO/PMN-PT laminate structure featuring high ME coupling. In this case when an E field is applied to the heterostructure, it is actually applied to the PMN-PT substrates, which leads to a significantly reduced leaking problem and enhanced ME coupling on the CFO layer. Thus, the incorporation of PMN-PT makes ME coupling much stronger for thin film PMN-PT heterostructures. In this case, introducing the PMN-PT into the BFO-CFO self-assembled structure seems reasonable. And because the piezoelectric effect of BFO is much smaller compared with PMN-PT, the E-field-induced strain in a BFO-CFO/PMN-PT heterostructure is mainly due to the domain reorientation in the PMN-PT substrate, unlike that in BFO-CFO/STO heterostructures[66,84,85]. Based on the well-studied behavior of BFO in BFO-CFO systems, BFO was selected for this project. The main impetus for identifying BFO as the matrix phase is that it provides strain for the heterostructures, and successfully forms a self-assembled (1-3) heterostructure. For this purpose, similar matrix materials such as $BiTiO_3$ can be also used in the future.

1.2.3. Magnetostrictive spinels.

There are numerous magnetostrictive materials that possess a large magnetostrictive coefficient (λ_m). However, spinel-class materials, denoted as AB_2O_4, which have similar lattice structures and parameters with perovskite, such BFO and BiTiO3 (BTO), are widely studied and investigated for their (1-3) heterostructure. In particular, (1) perovskite and spinel share similar lattice parameters that can guarantee epitaxial growth on single-crystal substrates, and (2) the wettability of the perovskite and spinel are rather similar, which results in forming a nanopillar/nanobelts structure instead of segregated laminated structure[69]. The normal spinel lattice structure of $MgAl_2O_4$ is shown in = Figure 1.13[86]. Generally, spinel materials feature a tetragonal or cubic phase structure, which is compatible with BFO for the (1-3) heterostructures[87]. Several spinel materials were selected for this project, as described in the following sections.

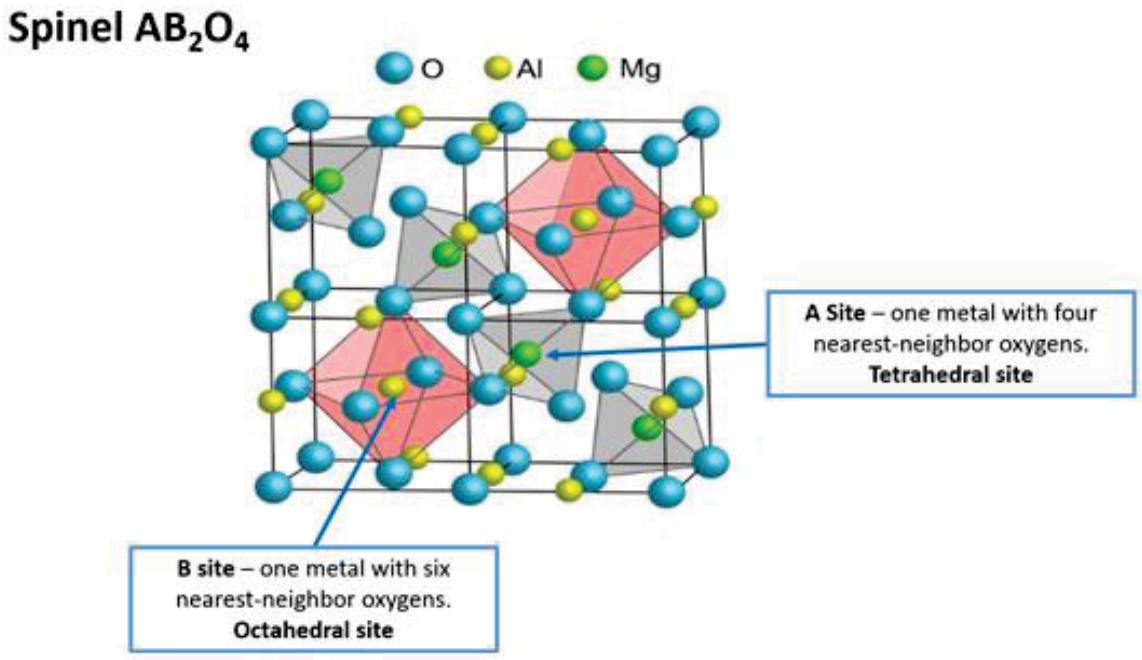

Figure 1.13. Lattice schematically illustration of spinel materials. CDTi. http://www.cdti.com/spinel/, with fair use.

$CoFe_2O_4$ (CFO), Cobalt Ferrite.

CFO is a common magnetostrictive material within the spinel class. CFO has a $T_c = 520℃$, and a cubic lattice structure at room temperature, which has a $a_c = 8.392Å$[88], as shown in Figure 1.14. Given the fact that CFO has a relatively large magnetic coercivity (~5000Oe)[61], it can be considered to be a soft magnetic material. The spinel ferrite CFO has a large λ_m, which is about -360 ppm[70], The magnetic parameters of CFO are listed in Table 1.2[67]. Since cobalt ferrite has a high saturation magnetization, which imparts high storage density, these magnetostrictive materials are widely used as data-storage media—for example in high-density hard-disk recording media, random access memories, and even magnetic fluids. Moreover, CFO has also been widely studied as a magnetostrictive material in the vertically or horizontally integrated heterostructure.

By integrating the large magnetostrictive coefficient and the developed unique heterostructures of CFO, ME coupling could be dramatically enhanced.

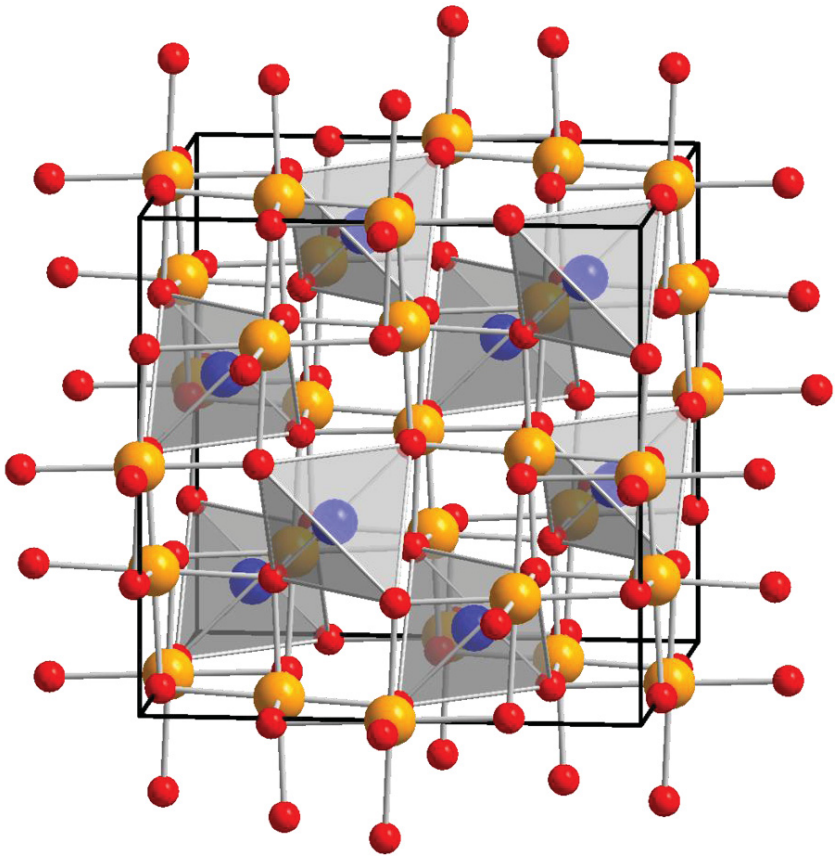

Figure 1.14. The lattice structure of CFO.

Table 1.2. Magnetic parameters of CFO: magnetocrystalline coefficients K_i (mJ/m^3), magnetostrictive constant λ (ppm), and saturation magnetization M_S (10^5 A/m). Yan, L. Two phase magnetoelectric epitaxial composite thin films, Virginia Tech, (2009), with fair use.

K_1	λ_{100}	λ_{110}	λ_{111}	λ_s	M_s
0.1	-590	-60	120	-110	3.5

$CuFe_2O_4$ (CuFO), Copper Ferrite.

Although some magnetostrictive materials such as CFO have large λ_m, and high coercivity, some disadvantages must be noted. The mechanical quality factor (Q) is a parameter that describes energy loss per cycle[89,90]. Since energy loss was involved, the Q factor can also be used as a criteria of efficiency[91,92]. When the Q factor is large, it implies higher efficiencies and lower losses. Additionally, the energy of the magnetic materials could be described as the area within the M-H loop[93]. With respect to CFO, because it has a high saturation magnetization and coercivity, the area within the M-H loop was quite large, which indicates high losses and low efficiency—which is a feature not conducive for advanced industrial applications.

Copper ferrite ($CuFe_2O_4$, CuFO) is also a spinel ferrite. Unlike CFO, it has a tetragonal (T) structure when slowly cooled from its Curie temperature (T_c=427℃)[94,95]. The c/a ratio of CuFO is 1.06, with lattice parameters of $a_T = 8.202$Å and $c_T = 8.730$Å[94], which are similar to CFO, thus making them compatible with self-assembled with BFO materials. The lattice parameters are also fairly compatible with the PMN-PT substrate single crystals as well.

Moreover, the magnetic coercivity of CuFO has been reported to be about 100-200 Oe[94-97], which is dramatically lower than that of CFO (~5000Oe)[61]. That means that the losses associated

with CuFO are smaller than that of CFO—potentially offering higher Q factors and efficiencies. The magnetostriction coefficient of CuFO was reported to be $\lambda_m = 110ppm$[98] as shown in Table 1.3. Although this is only 1/3 of CFO, this number can be considered to be large as well.

Recently, epitaxially grown CuFO was deposited on $MgAl_2O_4$ (MAO)[97], which shows low losses. This also enhances the potential of good epitaxially grown BFO-CuFO thin film on PMN-PT substrates due to the similar lattice parameters of MAO and PMN-PT single crystals.

Even though it is difficult to find a balance between high magnetostriction and low losses by using single-phase CuFO materials in many cases, introducing the (1-3) heterostructures shows promise in significantly expanding magnetostriction. This approach represents a new method for balancing high Q factor and high magnetostriction—not only for CuFO, but also for many other spinel ferrites.

Table 1.3. Magnetostriction coefficient of CuFO. Arai, K. I. & Tsuya, N. Observation of Magnetostriction in Cu Ferrite Single Crystals. physica status solidi (b) 66, 547-552, doi:10.1002/pssb.2220660217 (1974) , with fair use.

Quenching T (K)	T (K)	λ_{100} (ppm)	λ_{111} (ppm)
820	295	-108.0	13.8
	77	-92.5	28.1
900	295	-87.3	9.8
	77	-113.9	19.7

$Ni_{0.65}Zn_{0.35}Al_{0.8}Fe_{1.2}O_4$ (NZAFO), Aluminum doped Nickle Zinc Ferrite.

In order to identify that balance between a high Q factor and a large magnetostriction, a material with low losses with a high Q factor is needed. The nickel-zinc ferrites, which exhibit minimal losses and relatively large magnetostriction coefficient, have captured the attention of researchers and scientists[99]. For example, Emori et al.[99] recently reported the novel spinel crystal $Ni_{0.65}Zn_{0.35}Al_{0.8}Fe_{1.2}O_4$ (NZAFO). This material features high magnetostriction with small losses; additionally, the coercivity of NZAFO is fairly small (~2 Oe), thereby imparting a fairly high Q factor[89,91]. Accordingly, this material can be utilized in many applications such as multi-level memory devices[100,101] or for magnetoelectric (ME) random access memory (MeRAMs)[10]. However, when compared with CuFO the coercivity is even smaller, which means it suffer from weaknesses such as high data density[102] and a higher reading resolution requirement[103].

On the other hand, NZAFO and CFO, CuFO are all spinel magnetic materials. After introducing the heterostructures, magnetic anisotropy could be significantly alternated due to the fact that the (3-1) heterostructures induce large shape anisotropy, resulting in a dominated anisotropy effect in self-assembled heterostructures. Thus, NZAFO with its similar lattice parameters as CFO and CuFO, has potential for use in BFO-NZAFO heterostructures, which would enable the manipulation of magnetic anisotropy and coercivity, resulting in an attractive composite for future applications.

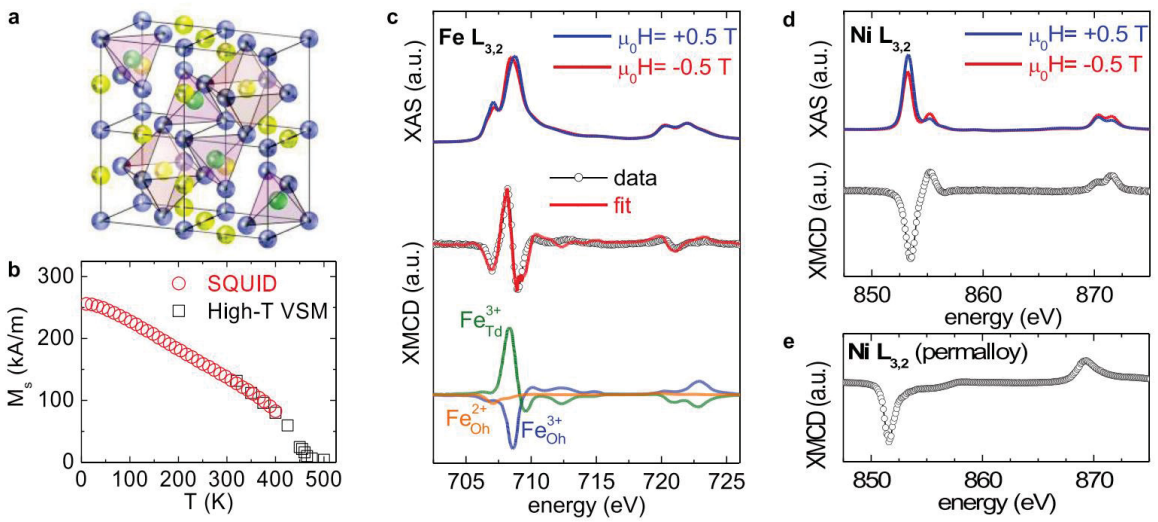

Figure 1.15. The lattice structure of NZAFO, and the evidence of low losses and high-quality factor. Emori, S. et al. Coexistence of Low Damping and Strong Magnetoelastic Coupling in Epitaxial Spinel Ferrite Thin Films. Adv Mater 29, doi:10.1002/adma.201701130 (2017), with fair use.

1.2.4. Significance and objectives of this work.

Because of the achievable reading/writing source (e.g., electric field and magnetic field), rapid response time, and larger storage density, magnetoelectric (ME) materials continue to be of interest to scientists and engineers. Therefore, nanocomposites featuring both magnetostriction and piezoelectricity were investigated to increase the converse magnetoelectric (CME, α) coefficient, and ME coupling coefficient.

However, the single-phase ME materials are limited given that the ME coupling effects in these materials are somewhat small. In contrast, composites made up of piezoelectric and magnetostrictive materials represent a simple and easier way to enhance ME coupling. Amongst all the variety of nanocomposites, vertically/horizontally integrated heterostructures that feature strong lattice contact, lower clamping effect, dramatically enhanced α, and easier reading directions, show promise for advanced applications. This heterostructure also affords the

possibility for identifying a balance between the magnetostriction coefficient and a higher Q factor, thereby enabling the fabrication of materials with a high ME coupling coefficient and enhanced efficiency. Also, the pinned rotation of the magnetic domains helps to create more stable magnetic states, as well as helps to create non-volatile properties with only volatile materials.

The current investigation features five specific goals and objectives:

1. Create two-phase vertically integrated heterostructures using different ME materials—the goal of which is to provide a much larger α and larger strain-induced magnetic shape anisotropy in comparison with the single-phased ME nanomaterials.
2. Create a vertically integrated heterostructure with large α and lower losses and higher efficiency.
3. Investigate the stable magnetization states that this heterostructure could achieve, and thus reveal their potential for use in advanced memory devices, logic devices and patterned electrodes.
4. Investigate the non-volatility of the (1-3) heterostructures on even PMN-PT substrates with volatile piezoelectric response, and the potential applications of these (1-3) heterostructures.
5. Elucidate the anisotropy manipulation of these (1-3) heterostructures.

CHAPTER 2: EXPERIMENTAL METHODS

2.1. Manufacturing and Perpetration of the Samples.

Because the quality of the single crystal is critical for epitaxially grown thin films, the preparation of the fabrication process is critical for the final sample. Epitaxially grown thin film require a smooth surface on which to close pack the films. Therefore, polishing becomes critical in the fabrication process.

2.1.1. Polishing of the PMN-PT

PMN-PT crystals must be polished for the successful formation of self-assembled heterostructures. In this project, relief-polishing techniques were chosen to polish the PMN-PT substrate to a level of 1.5nm roughness. For the polishing process, a Bueler MiniMet 1000[104] was used, as shown in Figure 2.16. The sample was first waxed on the heated sample holder, which was about 70℃. After fixing the sample to the holder, the sample holder was cooled under tap water for 2 min. Finally, the sample was polished and smoothed using 1500-grit sandpaper. A check for flatness was conducted using a glass slide as recommended.

The sample was then fine polished using the four steps listed in Table 2.4. All processes used 50rpm rotation speed and 5 pounds pressure. After the final cleaning step, the sample holder was heated to 70℃, after which the sample was removed and ultrasonicated in acetone for 20 min. By utilizing this process, the sample roughness could be reduced to as small as 1.5nm, as shown in Figure 2.17. At that 1.5nm level, it is possible to identify the different domains of PMN-PT on the surface, which indicated good surface quality.

Figure 2.16. MiniMet 1000 polisher. Buehler. <https://www.buehler.com/minimet-1000-semi-automatic-grinder-polisher.php>, with fair use.

Table 2.4. Fine polishing steps using MiniMet 1000.

Process	Polish Cloth	Polish Media	Particle size (μm)	Time (min)
Lapping	Chem cloth	Diamond suspension	3	15
Polishing	Nylon cloth	Diamond suspension	1	15
Fine polishing	Final finishing cloth	Colloidal silica	0.04	4
Particle cleaning	Final finishing cloth	Colloidal silica	0.04	4

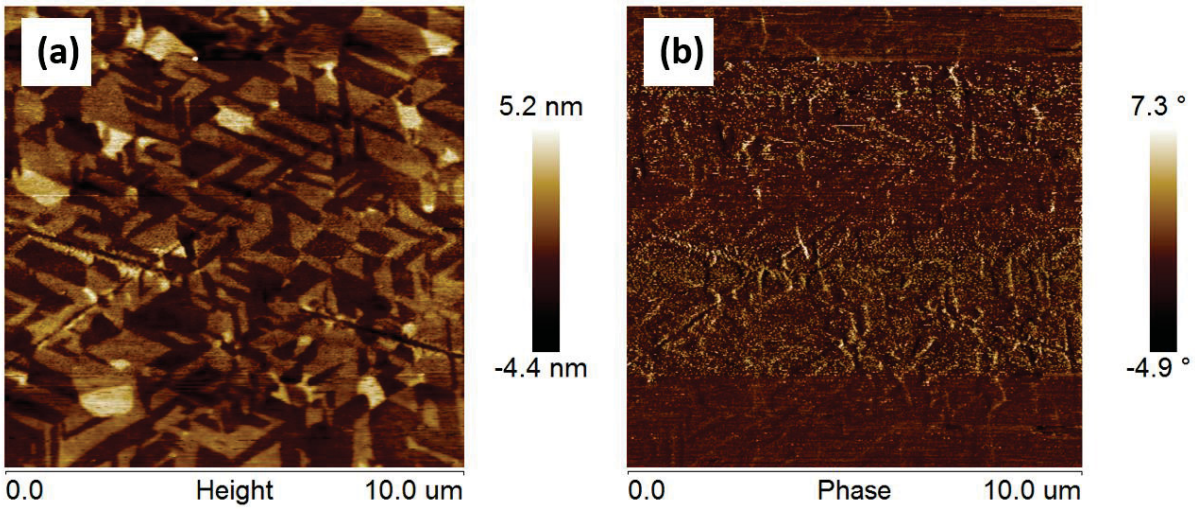

Figure 2.17. Polished PMN-30PT surface. (a) 2d information. (b) Phase information.

2.1.2. Pulsed laser deposition

There are many techniques for fabricating an epitaxially grown thin film, including chemical vapor deposition (CVD) and physical vapor deposition (PVD)[45]. Pulsed laser deposition (PLD), which is conceptually simple, belongs to the physical vapor deposition type. This method uses a high-power pulsed laser beam that is directed toward a sample material within a high-vacuum chamber. The materials are then struck by the laser and vaporized by the high-energy beam, becoming a plasma plume. Subsequently, the plasma is deposited on the desired substrates, as shown in Figure 2.18[105]. There are several advantages of PLD for growing an epitaxially thin film on single crystals. For instance, the ejection of the materials from the target is constant if the energy and repetition rate are fixed; accordingly, a range of similar samples can be easily created using PLD, which cannot be achieved using CVD[105]. Moreover, PLD is also preferred due to its versatility in that a range of different materials can be deposited in a wide variety of gases over a broad range of gas pressures. It is fast, meaning that high-quality samples can be grown in a relatively short time (e.g., 10-15 minutes)[58].

A PLD system usually features a high-power laser generator, an ultra-high vacuum chamber, and a vacuum-support system. In this project, a laser LPX305i form Lambda Physik with KrF radiation was used. The wavelength of the laser generator was set at 248nm, and the pulse duration was 30ns. The energy of the laser beam and the repetition rate can be adjusted from 500-1000mJ and 1-20Hz, respectively.

Although PLD is a relatively simple and straightforward approach, setting the correct parameters are still important for high-quality thin films. Those parameters include repetition rate, spot energy density, target-to-substrate distance, deposition temperature, base vacuum level and working gas pressure. In this project, the spot energy density was usually 1.2-1.5 mJ/mm^2, the

repetition rate ranged from 3Hz to 10Hz, and the target-to-substrate distance ranged from 2.5-3 cm. The base vacuum level was approximately 10^{-6} Torr, and the working pressure ranged from 90-150 mTorr. Normally, one deposition will include using different targets in order to create an electrodes layer beneath the thin-film sample.

In considering the various material parameters for the PLD deposition, soft materials such as $SrRuO_3$ often use small spot-energy density and large target-to-substrate distance because the materials are easily struck from the target. However, for hard materials such as ferrites and perovskites, the energy requirement is much larger. Moreover, because the harder materials are not as readily struck from the targets, the target-to-substrate distance usually will be much smaller. In this project, the deposition temperature ranged from 650℃ to 700℃. At this high temperature, the BFO will not be vaporized, and the materials still maintain high movability to mix and form a self-assembled structure.

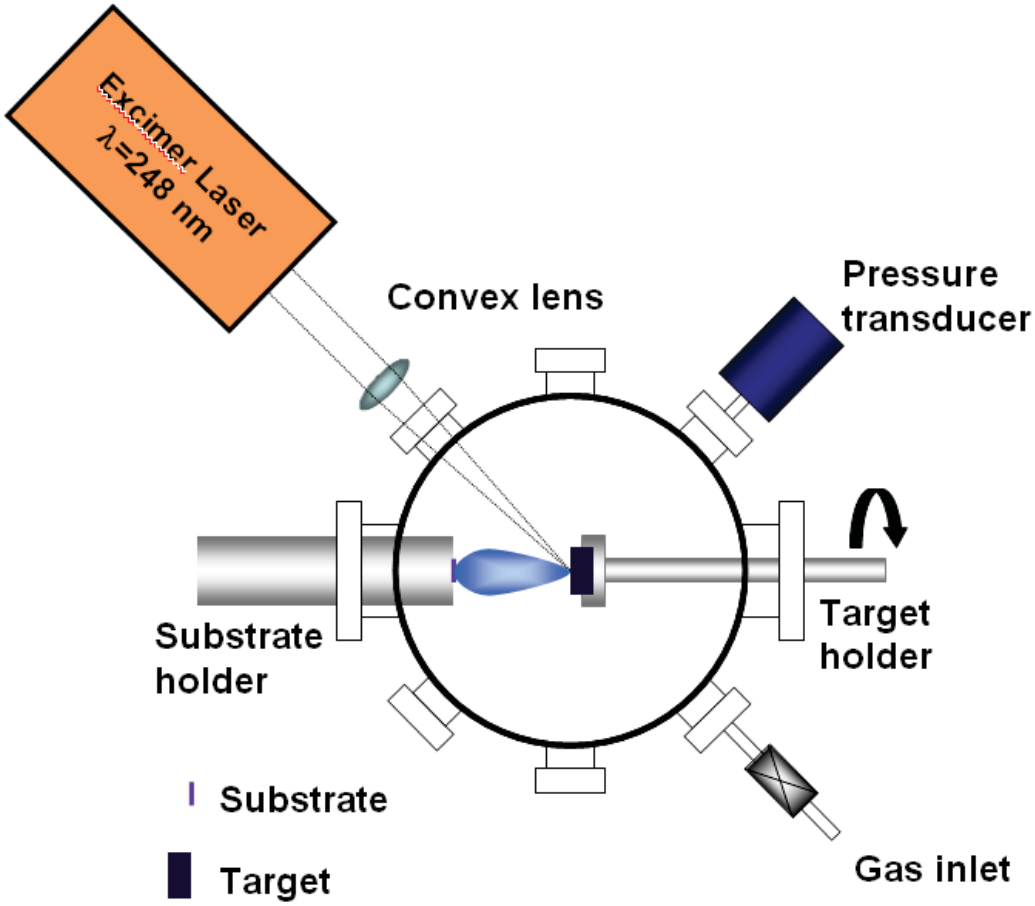

Figure 2.18. Schematic figure of PLD. Chan, N.-y. Study of barium strontium zirconate titanate thin films and their microwave device applications, The Hong Kong Polytechnic University, (2010) , with fair use.

2.1.3. Switching pulsed laser deposition.

Typically, if a self-assembled heterostructure is required for a project using the PLD method, mixed two-phase targets are mandatory. In instances when a new self-assembled structure or a new film composition is needed, a new target is required. However, these targets are quite expensive due to the purity and structure requirements of the deposition.

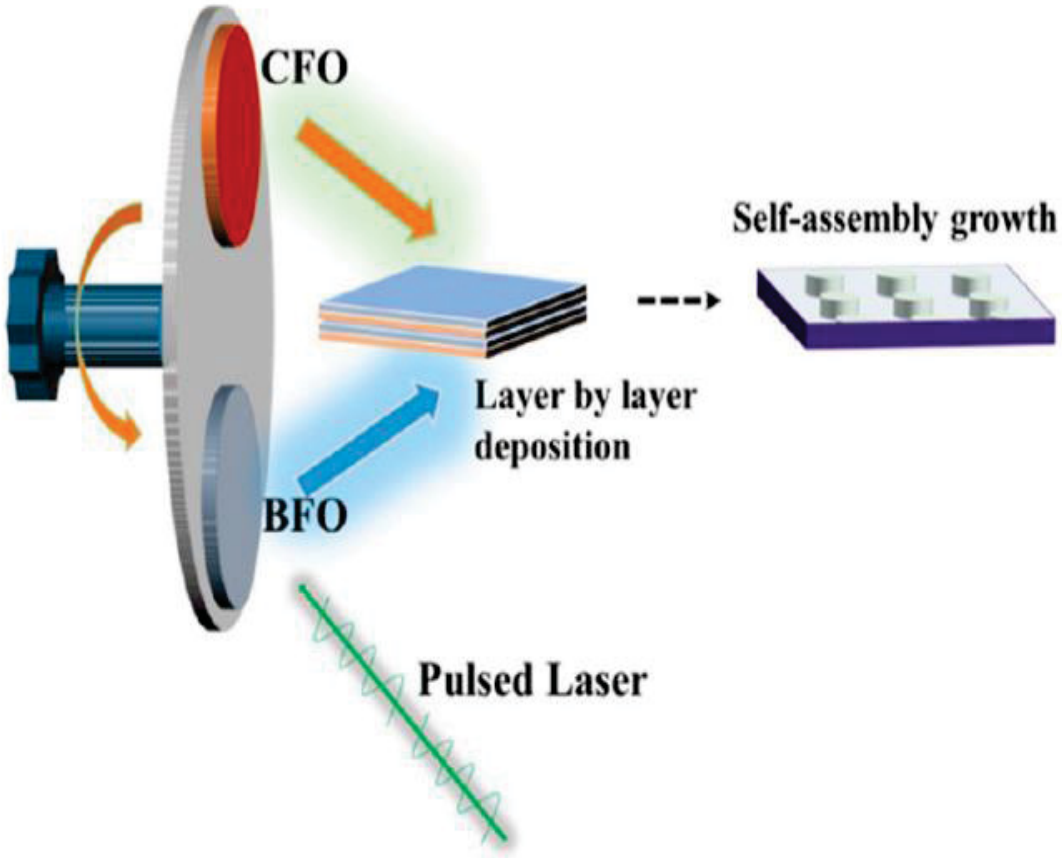

Figure 2.19. Schematic of SPLD. Li, L. et al. Direct Observation of Magnetic Field Induced Ferroelectric Domain Evolution in Self-Assembled Quasi (0-3) BiFeO3-CoFe2O4 Thin Films. ACS Appl Mater Interfaces 8, 442-448, doi:10.1021/acsami.5b09265 (2016) , with fair use.

Recent studies have shown the usefulness of a new technique called fast switching deposition for the deposition of ferrite layers, as shown in Figure 2.19[106]. This technique switches the targets during pulsed laser deposition. Linglong et al.[106] have shown that if two single-phase targets are frequently switched, the time will be insufficient for the two individual phase layers (in their case, BFO and CFO) to fully cover the substrates. By utilizing fast switching deposition, a layer-by-layer structure was prevented; instead, a two-phase mixed BFO-CFO nanopillar structure was identified. Switching PLD (SPLD) is a feasible method for creating a self-assembled structure, which is convenient for controlling composition. SPLD is also an economical and practical method that can be used for different self-assembled heterostructures of differing compositions and thickness requirements. Therefore, it is widely used in heterostructure thin-film structures[56].

2.2. Characterization Techniques

The epitaxial growth of thin films feature different advantages such as closed-pack induced high ME effects; on the other hand, this means the required high sample quality. In addition to the importance of the quality of the epitaxial growth—referring to the single crystallinity of the thin film that grows on the single crystal substrates—surface quality is also important due to the self-assembled heterostructure surface features. Finally, the ME properties of the sample need to be carefully examined as well.

2.2.1. Scanning Probe Microscopy (SPM)

SPM, which was developed in 1981[67], is a microscopy technique that forms images of surface morphology using a physical probe that sweeps and scans the sample. By changing the tip and the connection of the control unit, SPM can be used for different aspects, including atomic force microscopy (AFM), magnetic force microscopy (MFM) and piezoresponse force microscopy (PFM)[67]. AFM focuses on obtaining height and morphology information from a surface, PFM is used to gather piezoelectricity information, and MFM scans the magnetic domains on the sample surface. In this project, AFM and MFM measurements were obtained using the Vecco 7300 AFM/MFM/PFM instrument.

AFM measurements

AFM gathers the surface morphology information by 'touching' or 'feeling' the surface via a very small tip, which then forms an image on the monitor, as shown in Figure 2.20[107]. Although AFM is similar to the SPM technique, the former is focused on gathering topographic information, and could ultimately achieve true atomic resolution[107]. There are many advantages associated with utilizing an AFM, including the ability to achieve 3D information, easy sample preparation, and easy set up without any conditional requirements. Moreover, it can be extended by introducing functional modes.

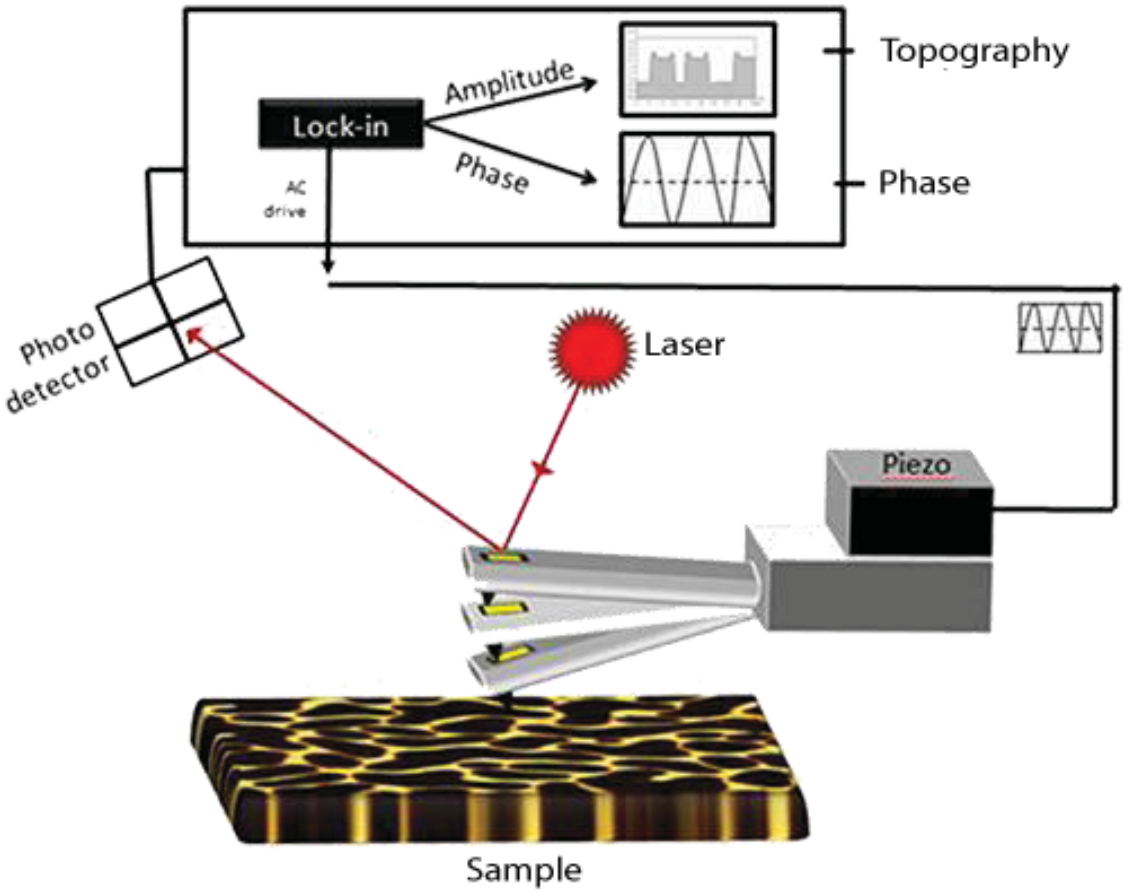

Figure 2.20. Schematic illustration of AFM. Giessibl, F. J. Advances in atomic force microscopy. Reviews of modern physics 75, 949 (2003) , with fair use.

In terms of functionality, a sharp tip is mounted on the scanning head, referred to as the xyz scanner. This scanner allows the tip to move three-dimensionally. During scanning, a bias voltage V is applied to the sample. The tip comes very close to the surface, and when the distance reaches several angstroms a current will appear due to the tunneling effect between tip and sample, which could be used for the feedback for z-axis information. For recording morphological information, the tip moves at x- and y-axes and the z-axis information is monitored and recorded to form an image. The z-axis information is recorded by a cantilever or force sensor[107]. For sensing surface

information, the materials that make the tip should be rigid and hard. After the tip moves up and down during scanning, a laser beam is illuminated on the back side of the cantilever. When the tip moves, the laser beam is reflected and captured by a photodetector in the main control unit of AFM. By recording and interpreting resulting data, height information can be captured and shown on the monitor.

AFM measurements not only collect height information, but also record phase information. During scanning, the tip moves at the resonance frequency. If the materials that form the surface are uniform, the tip should not vibrate on other frequencies. However, if the surface is not uniform—which is often the case when the surface is formed by different materials with differing elastic stiffnesses—the vibration of the tip will be altered. The vibration shifting could cause a phase shift in the laser beam, which is also recorded by the program. Although quantitative analysis of this phase shifting is almost impossible, the phase image shows different materials with different elastic constant, which typically will indicate the different materials.

There are various modes to consider when obtaining AFM measurements: contact mode, non-contact mode, tapping mode, or mixed mode. For now, the contact mode is rarely utilized due to the high possibility of damaging the tip. Moreover, contact or non-contact mode can create a dragging effect, which gives wrong information for the surface, as shown in Figure 2.21[107]. Nowadays, tapping mode is often chosen because of tip protection, non-dragging effect, avoiding surface damage, and the ability to gather reliable data.

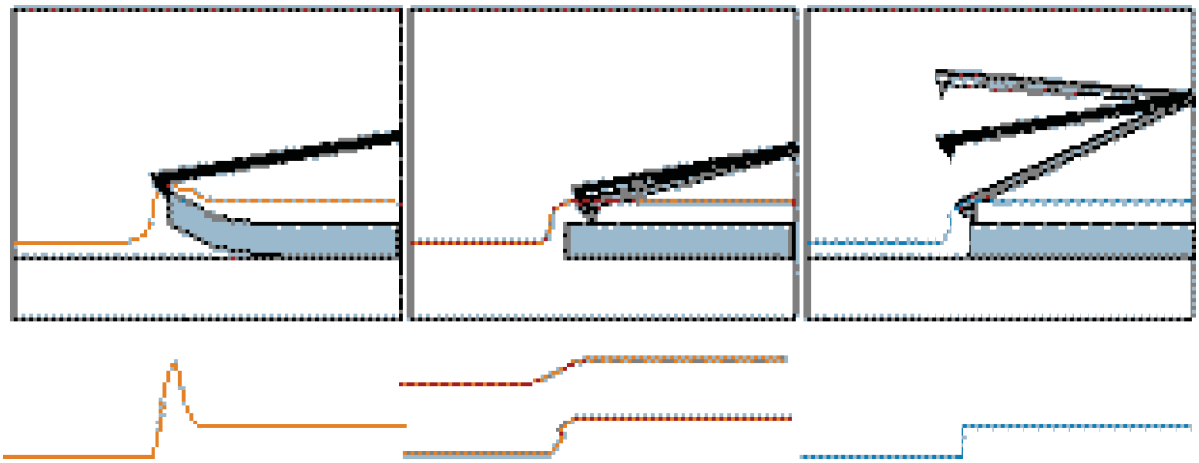

Figure 2.21. Illustration of different modes of AFM. Giessibl, F. J. Advances in atomic force microscopy. Reviews of modern physics 75, 949 (2003) , with fair use.

MFM measurements

MFM is a mode of non-contact SPM. After the invention of the AFM technique, users realized that if the tip was formed using ferromagnetic materials, the local scaled magnetic signal could be detected during scanning[108], as shown in Figure 2.22[109]. Thus, MFM is an important and intuitive tool for imaging near-surface magnetic signals MFM only works under non-contact mode. And due to the lift-up tips, the surface topographic information is almost nonexistent, which means that the obtained data represents the local response of the magnetic signal on the sample surface. Therefore, MFM can be used to directly record information on the magnetic domains of the sample surface, which represents a valuable technique for visualizing magnetic domains.

It must be noted that quantitative analysis of the information gathered by the MFM is also impossible, as it is not possible to quantify the strength of the magnetic domains. Instead, data is recorded as the orientation of the magnetic domains. For this investigation, we are trying to determine how induced electric fields changes the orientation of magnetic domains. When

applying the electric field by using the conductive tip, the magnetization is changed because of the ME effect, which is then reflected in the MFM canning images.

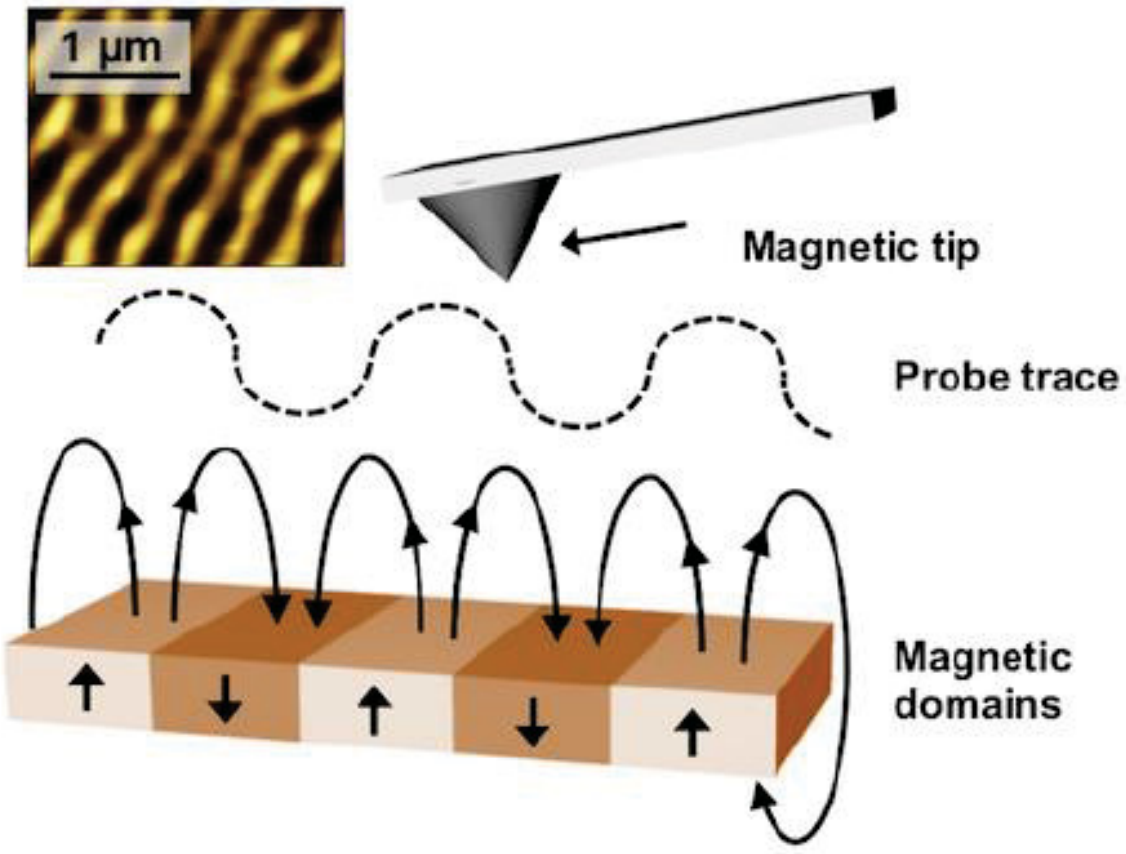

Figure 2.22. Schematic illustration of MFM measurement. Idigoras, O. et al. FEBID fabrication and magnetic characterization of individual nano-scale and micro-scale Co structures. Nanofabrication 1 (2014) , with fair use.

2.2.2. X-ray Diffraction scan (XRD)

XRD is widely used for examining crystal structure, lattice parameters and the epitaxial quality of samples. Using the XRD technique, an x-ray is incident to a sample, and the output incident x-rays will be diffracted by the crystal structure within the sample to many specific directions[110]. By collecting angle and intensity data of diffracted x-rays, the lattice information can be translated. While there are many methods for collecting lattice information, XRD is still the most economical and fastest approach. In the single-crystal XRD measurement technique, the sample is mounted on a goniometer that can move and rotate at any angle and direction. The sample is then illuminated by an X-ray beam, generating a diffraction pattern, which can be cached by the detector. This helps to locate the orientations of the substrate and epitaxial thin film. The diffracted and incident beams follow the Bragg's Law[110]:

$$2d\sin\theta = n\lambda \tag{1.7}$$

Where d is the spacing between diffracting panels, θ is the incident angle, λ is the wavelength of the beam.

In this project, a PANalytical X'Pert high-resolution XRD was used, as shown in Figure 2.23[111]. This XRD system carries a two-bounce monochromatic, triple-windowed detector, and a triple-circled cradle. This XRD was utilized under 45kV and 40mA, and the λ was under 1.5406Å (Cu Kα).

Figure 2.23. PANalytical X'Pert high-resolution XRD. Dodd, J., Yazami, R. & Fultz, B. Phase diagram of Li x FePO4. Electrochemical and Solid-State Letters 9, A151-A155 (2006) , with fair use.

2.2.3. Vibrating sample magnetometer (VSM)

Magnetic properties represent the key features for monitoring the ME properties of the multiferroic materials. Normally, the methods of measuring the magnetic moments can be divided into three classes: force measurement with H field, magnetic induction measurements, or other indirect measurements[112]. Among these methods, a magnetic induction measurement represents the one with highest resolution and easiest setup system[113]. In this method, a magnetic sample is placed in an electromagnet, then forced to vibrate with a vibrating head. During the sinusoidal vibration in the H-field, the magnetic change will affect the vibration of the head. By recording the change of vibration, the magnetization moment of the sample can be interpreted as an M-H loop. In this project, a Lakeshore VSM 7300 was chosen. Another MicroSense Model 10 was also used for the angular-dependent remnant magnetization change in this study.

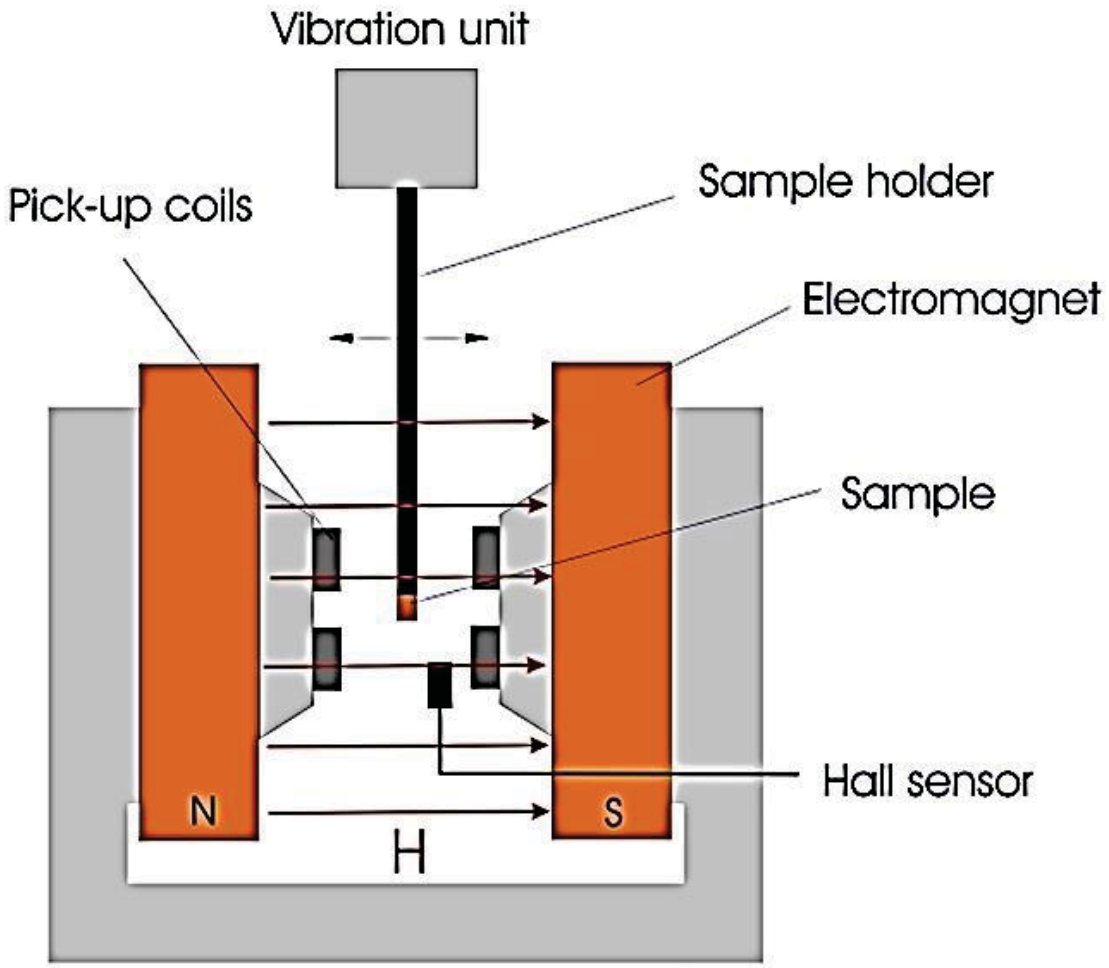

Figure 2.24. Schematic illustration of VSM. Rafique, M. Study of the Magnetoelectric Properties of Multiferroic Thin Films and Composites for Device Applications, COMSATS Institute of Information Technology, Islamabad-Pakistan, (2014) , with fair use.

2.2.4. Transmitting electronic microscopy (TEM)

TEM is a microscopy method that transmits an electron beam through a sample and then records the information[114]. TEM provides cross-sectional information that can be captured quite easily; diffraction patterns can be recorded as well. If an energy-dispersive measurement is introduced in the system, elemental information can be also recorded by the detector. Therefore, the transmitting electronic microscopy is a useful way to see the formation of a self-assembled structure through the entire thickness. In this project, a JEOL TEM 2100 was used operating at 200kV. A selected area diffraction pattern and X-ray spectra were used for the elemental and crystalline study.

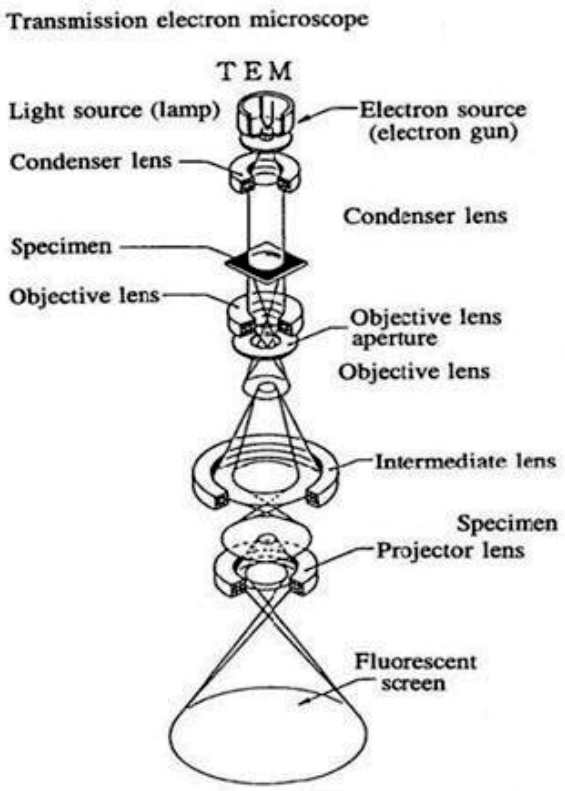

Fig 1

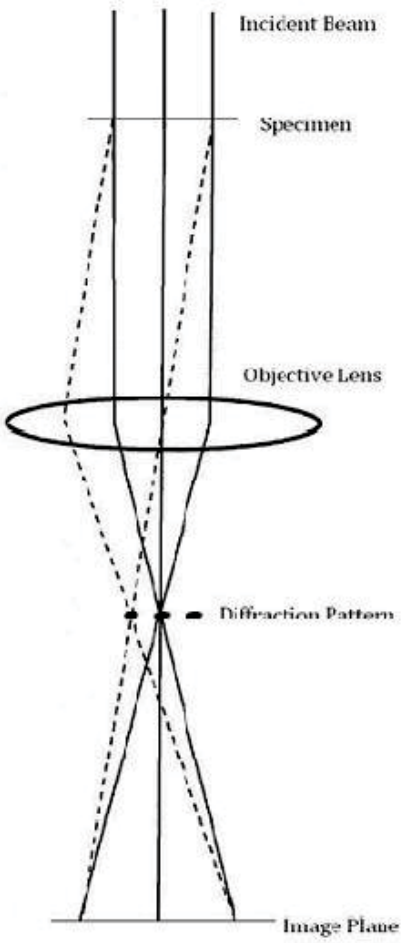

Fig 2

Figure 2.25. Schematic illustration of TEM. Wang Z L. Transmission electron microscopy of shape-controlled nanocrystals and their assemblies[J]. 2000, with fair use.

TEM requires a finely prepared sample in order to obtain high-quality data and images. Therefore, the preparation of the TEM sample represents a critical step in the process. In this project, the sample was lifted up by the focused ion beam (FIB, FEI Helios 600 NanoLab), which utilizes the ion beam to cut and lift the sample; it then uses the ion beam to polish the sample to obtain a fine cross-section.

2.2.5. Selected area diffraction patterns (SADP)

SADP is a method that records the diffraction pattern of the transmitted beam of a selected cross-sectional area. This measurement is much like the XRD measurement, and it follows the Bragg's law as mentioned in the above sections. However, unlike XRD, SADP is able to record the crystallinity data associated with a selected area, which can be the nanostructures in the self-assembled thin film, or the thin film with the substrates. In this project, SADP was performed utilizing a Philips EM 420- electron microscope working at 120kV.

2.2.6. Energy dispersive X-ray spectroscopy (EDS)

Energy dispersive X-ray spectroscopy (EDS) is a standard method for identifying and quantifying elemental compositions in a very small sample of material (even a few cubic micrometers).[114] In this methods, the atoms on the surface are excited by the electron beam, emitting specific wavelengths of X-rays that are characteristic of the atomic structure of the elements. An energy dispersive detector (a solid-state device that discriminates among X-ray energies) can analyze these X-ray emissions. Thus, an elemental map can be obtained and the chemical composition of the nanostructures can be determined as well. In this project, we utilized a Philips EM 420- electron microscope working at 120kV.

CHAPTER 3: BFO-CFO/PMN-PT VERTICALLY INTEGRATED HETEROSTRUCTURES WITH E-FIELD ACCESSIBLE MULTI-STATE MAGNETIZATION HAVING GIANT MAGNETIZATION CHANGES

3.1. Overview of BFO-CFO/PMN-PT Nanopillar Heterostructures.

Cobalt ferrite ($CoFe_2O_4$, CFO) is a well-known magnetostrictive material featuring large magnetic anisotropy[39,61,115]. Nanopillar heterostructures of BFO-CFO have been epitaxially deposited on $SrTiO_3$ (STO) [106,116-118]. STO substrates have close lattice parameter matching with both phases of the BFO-CFO layer, thereby facilitating the presence of intimate lattice contact in the (1-3) heterostructure[119]. This intimate lattice contact transfers E-field-induced strain in the piezoelectric phase to the magnetostrictive one, resulting in induced magnetization changes in the nanopillars. As a consequence, (1-3) heterostructures possess significantly larger ME coefficients compared with single-phase ME materials[60]. Furthermore, lateral strain control is limited beyond a critical thickness ($\sim$100nm), above which the strain may fully relax[60]. Accordingly, (1-3) heterostructures can have significantly reduced thickness effects, resulting in thicker films with higher ME coupling. Wang et al.[39] showed that by controlling the size, shape, and volume-fraction ratio of the CFO nanopillar phase, the magnetic properties could be tailored. The nanopillar morphology was shown to contribute to the shape anisotropy, which can constrain the rotation of the magnetization direction.[39] This feature may offer an approach toward facilitating a new multi-state magnetization that is dependent on electric field history.

Moreover, compared with the PMN-PT substrates, the BFO matrix still has a nearly negligible piezoelectric response. Prior studies have only examined the deposition of BFO-CFO on STO, which just provides the lattice match with the BFO-CFO with no piezoelectric response. As such, the piezoelectric response of the heterostructure is fully reliant on the BFO matrix,

meaning that it is negligible. Due to the thickness of the BFO-CFO heterostructure, when an E-field was applied on the thin film, several leakage current will produced, thereby hindering the enhancement of the ME coupling of the BFO-CFO/STO. Wang et al.[66] previously reported a CFO/PMN-PT laminate structure featuring high ME coupling. In this instance when an E field is applied on the heterostructure, it is actually applied on the PMN-PT substrates, which leads to a significantly reduced leaking problem and enhanced ME coupling on the CFO layer. Thus, the PMN-PT makes the ME coupling much stronger for thin-film/PMN-PT heterostructures. Accordingly, introducing PMN-PT into a BFO-CFO self-assembled structure seems reasonable. And because the piezoelectric effect of BFO is much smaller compared PMN-PT, the E-field-induced strain in BFO-CFO/PMN-PT heterostructures is mainly due to the domain reorientation in the PMN-PT substrate, unlike that in BFO-CFO/STO heterostructures[66,84,85].

Here, we report a self-assembled two-phase vertically integrated BFO-CFO/$SrRuO_3$/PMN-38PT heterostructure via pulsed laser deposition (PLD). This BFO-CFO heterostructure possesses large magnetization changes in the CFO nanopillars through the application of a DC electrical bias (E_{DC}) to the substrate. A giant ME coefficient has been obtained. It was also found feasible to access multiple ($N \geq 4$) stable magnetization states with memory.

3.2. Experiment Method

A 65%BFO-35%CFO composition ratio was chosen for the substrates. All thin films were deposited by PLD. PMN-38PT (100) single-crystal substrates were grown by the Shanghai Institute of Ceramics at the Chinese Academy Sciences, and polished according to the protocol described in Section 2.1.1. Prior to the deposition, the substrates were cleaned with acetone and alcohol via ultrasonication. First, a 10nm SRO layer was deposited on the PMN-xPT (x=33, 35.5

and 38) at 700°C, 1.5 J/cm^2 energy density and 150 mTorr O_2 atmosphere. After annealing under 700 °C and 150 mTorr O_2 atmosphere for 30min, a 200nm BFO-CFO heterostructure was deposited at 650°C, 1.2 J/cm^2 energy density and 90 mTorr O_2 atmosphere. The sample was then annealed at 700°C and 100 Torr O_2. Crystal structures were determined by X-ray diffraction (Philips X'Pert system) scans. Magnetic hysteresis curves were recorded using a vibrating sample magnetometer (VSM, Lakeshore 7300 series). Atomic force microscopy (AFM) and magnetic force microscopy (MFM) images were obtained (Dimension 3100, Vecco), which were used to study the film surface quality and magnetic domain structures.

3.3. Surface Quality of the BFO-CFO/PMN-PT Nanopillar Heterostructures

Figures 3.26 (a) and 1 (b) provide AFM and MFM images for a BFO-CFO/SRO/PMN-38PT heterostructure. Part (a) shows an AFM image evidencing that a self-assembled square-like nanopillar morphology embedded in a matrix formed; and Part (b) provides an MFM image of the phase signal, demonstrating that different nanopillars have dark and light contrasts, indicating that the magnetic domain orientations do not have a preferred distribution amongst equivalent directions.

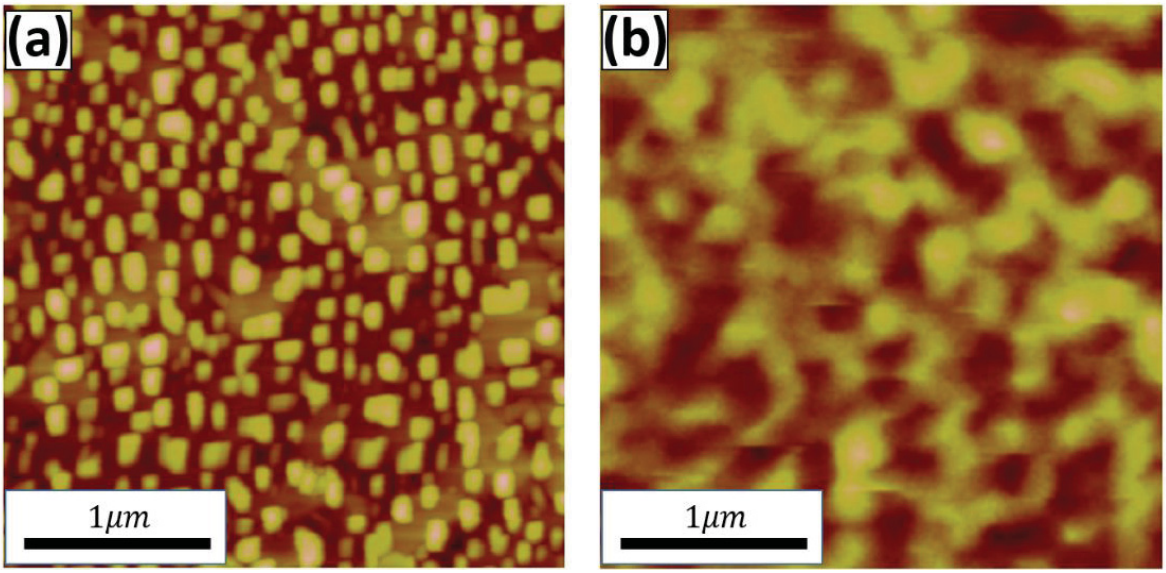

Figure 3.26. (a) AFM image shows square nanopillars embedded in a matrix, and (b) MFM phase image indicating magnetic domain orientations.

Figure 3.27 shows the AFM and related MFM images for the BFO-CFO/SRO/PMN-38PT sample. Part (a) confirms that self-assembled square-like nanopillars were obtained. In Part (c), magnetic domain signals, which are reflected by the phase signals, were observed as a dark and light contrast for the different nanopillars, indicating randomly oriented magnetic domains, principally because the sample was not poled prior to the MFM measurements. Part (d) provides an MFM phase diagram poled by positive and negative E-fields. Here, one can see an obvious difference between before and after E poling, and this difference is further confirmed by Part (b), which shows a line data for the phase data. Within the poled area, the line indicating after-poling has certain differences with the corresponding before-poling line. The positive poling makes the magnetic phase signal more negative, and the negative poling makes the signal more positive. However, outside the poling area the line figure is not significantly different between before and after poling. When an E-field is applied by the MFM tip, the BFO in the composite responds to

the signal with polarization. Then, the CFO nanopillar responds to the polarization with magnetic domain tilting, causing a change in the magnetic phase signal.

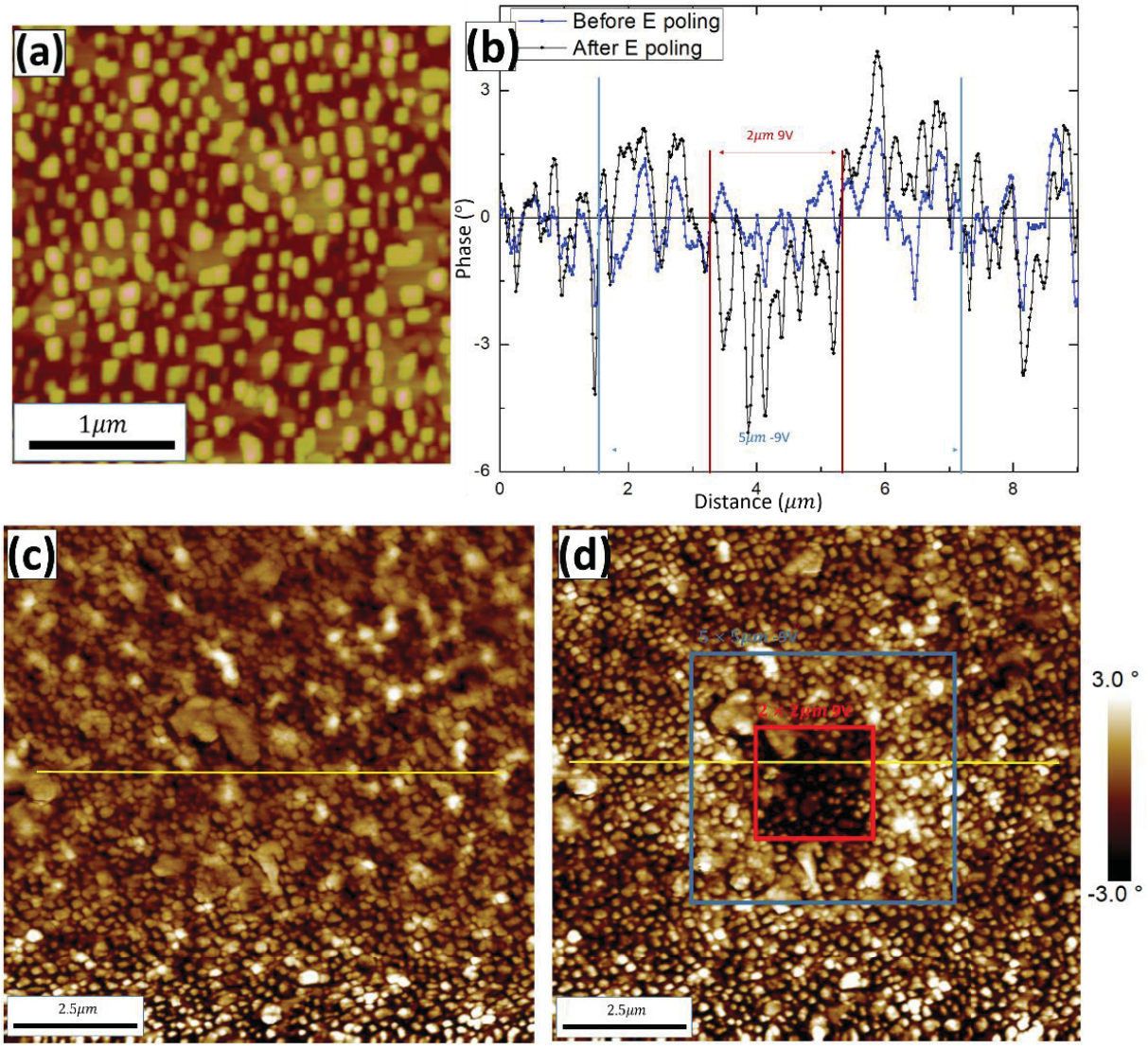

Figure 3.27. AFM & MFM images for BFO-CFO/SRO/PMN-38PT. (a): AFM image. (b): Line figure for the phase data comparison, labeled as yellow lines in the (c) and (d). (c): MFM phase image for BFO-CFO/SRO/PMN-38PT, before E poling. (d): MFM phase image for BFO-CFO/SRO/PMN-38PT, after E poling.

3.4. Epitaxy of the BFO-CFO/PMN-PT Nanopillar Heterostructures

Figure 3.28 provides an XRD line scan for a BFO-CFO/SRO/PMN-38PT heterostructure, illustrating that the stable phase of PMN-38PT substrates has a T structure with d-spacings of a_T=4.046 Å and c_T=4.002 Å. The results provided in this figure also confirm that the BFO-CFO nanocomposite layer grows epitaxially on PMN-38PT. The 2θ value for the (400) CFO peak was 43.17° and the analogous value for the (200) BFO peak was 45.71°, which corresponds to d-spacings of 8.376Å and 3.967Å, respectively. Compared with bulk BFO (3.960 Å[85]) and CFO (8.392 Å[88]), CFO undergoes a -0.179% strain (compressive) and BFO undergoes a 1.640% strain (tensile) along the OP direction.

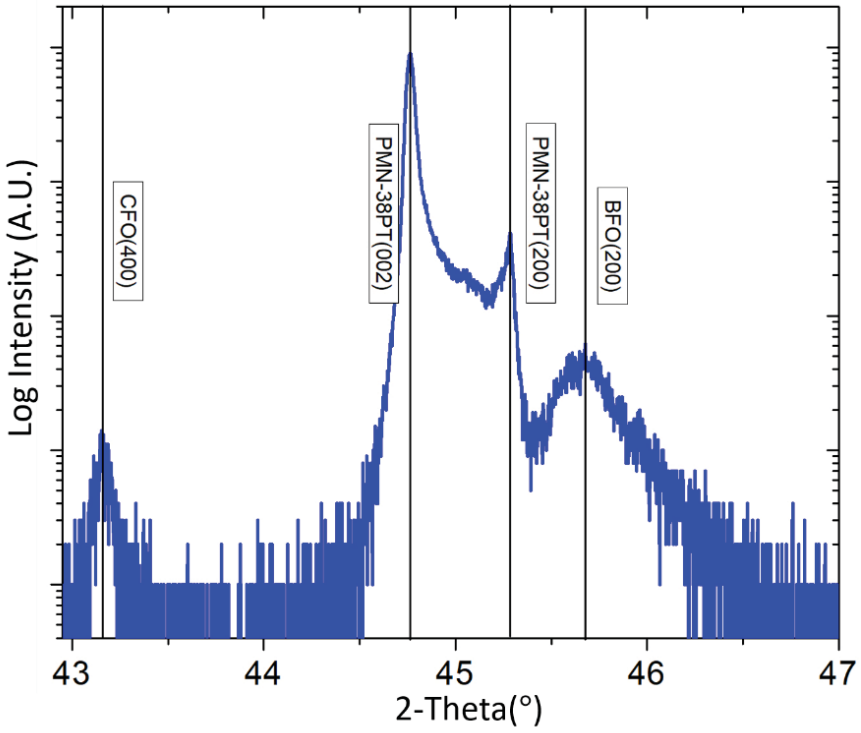

Figure 3.28. For BFO-CFO/SRO/PMN-38PT heterostructure, (a) 2θ scan showing an epitaxial growth BFO-CFO heterostructure

3.5. Magnetic Properties of the BFO-CFO/PMN-PT Nanopillar Heterostructures

Magnetization measurements were then obtained in response to an E_{DC} applied to the substrate. The electric field was applied along the out-of-plane direction. Figures 3.29 (a) and (b) show the M-H loops under various E_{DC} along the OP and IP directions, respectively. From these data, it can be clearly seen that the easy axis of the CFO nanopillars lies along the OP direction. This result is a reflection of the shape anisotropy of the nanopillar structure, which is much thicker than it is wide. As shown in the insert of Figs. 2 (a) and (b), the remnant magnetization (M_r) increases along OP with increasing E_{DC}. Furthermore, M_r decreases with increasing E_{DC} along IP, although the change is small. This is due to the combination of the anisotropy of the magnetostriction coefficient of CFO (λ_{CFO})[120] and the piezoelectric coefficient of PMN-xPT. The E-field-induced strain in the BFO-CFO/PMN-PT heterostructure is mainly due to the domain reorientation in the PMN-PT substrate, unlike that in BFO-CFO/STO heterostructures[66,121,122].

The BFO matrix has an important role to play in imparting a large shape anisotropy to the CFO nanopillars. With an increase of the aspect ratio of the CFO nanopillars, the shape anisotropy is significantly enhanced[39], altering the easy axis from IP to OP directions. From the right hand axis of Figure 3.29 (c), it can be seen that the PMN-38PT substrate undergoes a compressive stress along the OP direction under E_{DC}, resulting in the BFO-CFO nanocomposite layer experiencing tensile stress along IP. Since $\lambda_{CFO} < 0$, under a tensile IP stress, the easy axis of the CFO will rotate towards the OP direction[123]. As a consequence, the nanopillars will experience an increase in M_r with increasing E_{DC}, and, vice-versa, a lower M_r along the IP.

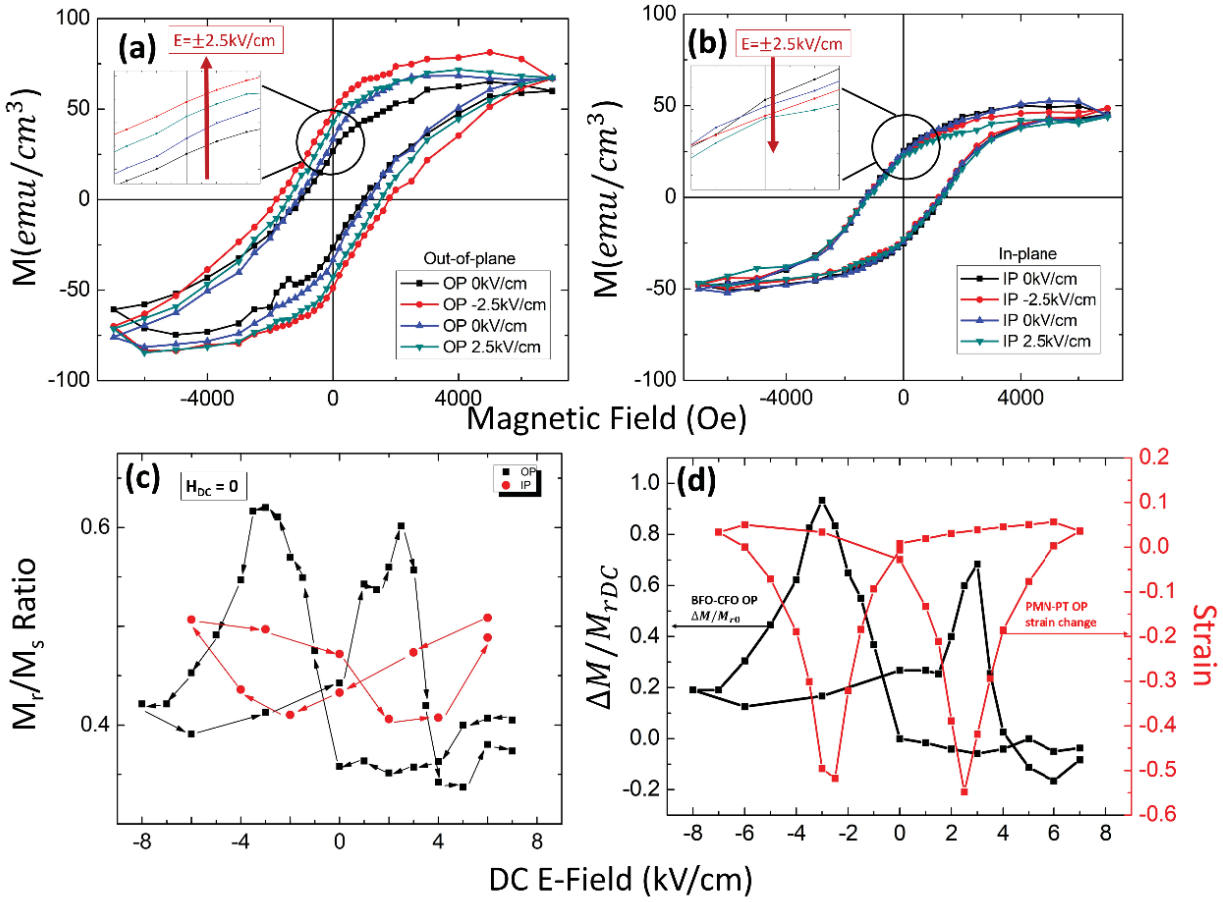

Figure 3.29. Magnetization measurements for BFO-CFO/SRO/PMN-38PT. (a): M-H loop under different E_{DC}, out-of-plane. (b): M-H loop under different E_{DC}, in-plane. (c): M_r/M_s ratio with changing E_{DC}, both out-of-plane and in-plane directions. (d): PMN-38PT substrate strain change with E_{DC} (right axis), and $\Delta M/M_{ro}$ (left axis) of BFO-CFO/SRO/PMN-38PT as a function of E_{DC}. The DC electric field E_{DC} was applied out-of-plane in all measurements.

The remnant-to-saturation (M_r/M_s) magnetization ratio in response to E_{DC} ($-7\text{kV/cm} < E_{DC} < 7kV/cm$) applied to the PMN-38PT substrate is shown in Fig. 3.29 (c). Data are given for E_{DC} applied along the OP and IP directions. As can be seen in Fig. 3.29 (c), the M_r/M_s ratio as a function of E_{DC} exhibited a clear butterfly-like shape, similar, but inverted to the $\varepsilon - E$ response of the PMN-38PT substrate. The highest values of the M_r/M_s ratio were 0.62 under $-3kV/cm$ and 0.60 under $2.5kV/cm$. As shown in Fig. 3.29(c), after E_{DC} reached -7kV/cm, the M_r/M_s ratio approached a stable plateau at a value of ~ 0.40. Even if the applied E_{DC} was decreased to zero, the M_r/M_s values were maintained. Similarly, after it reached $+7\text{kV/cm}$, M_r/M_s approached a stable plateau at a value of ~ 0.35. The IP direction had an opposite trend compared to the OP, exhibiting smaller changes in the M_r/M_s ratio with increasing E_{DC} that were inverted with respect to the OP data. This inversion occurs because the easy magnetization axis is aligned with the OP direction, imparting to the IP axis relatively lower values for both M_r and coercivity.

Next, $\Delta M = M_{rDC} - M_{r+o}$ (the difference between M_r under $E_{DC} \neq 0$ and M_r under $E_{DC} = 0$ after positive E_{DC}) was calculated. To normalize the change of ΔM, the value of $\Delta M/M_{rDC}$ verses E_{DC} was calculated as shown in Fig. 3.29(d) on the left axis. $\Delta M/M_{rDC}$ verses E_{DC} applied along the OP direction had the same inverted butterfly-like shape as the data for the M_r/M_s ratio. Also, $\Delta M/M_{rDC}$ as a function of E_{DC} displayed similar values above the electric coercive field of PMN-38PT (see right axis in Fig. 3.29 (d)), which were slightly greater than zero. The highest value of $\Delta M/M_{rDC}$ (~ 0.90) was found near $E_{DC} = -3\text{kV/cm}$, which corresponds to the electric coercive field under negative polarity. This confirms that BFO-CFO/SRO/PMN-38PT heterostructures experienced their largest E_{DC}-induced ME coupling under reverse polarization. The maximum value of $\Delta M/M_{rDC}$ ($\sim 90\%$) is notably higher than the largest value (66%) previously reported for a single CoFeB layer on PMN-30PT[24].

Figure 3.30 (a) shows the induced magnetization response to changes in E_{DC} as a function of time taken along the OP direction while $H_{DC} = 0$. Data are given at various E_{DC} values between 1kV/cm and 3kV/cm, beginning from a condition where the CFO nanopillars had been previously magnetized. In Figure 3.30(a), six distinguishable states were induced under different positive (1, 2, 3kV/cm) and negative (-1, -2, -3kV/cm) E_{DC} values. The largest response was found for $E_{DC} = -3kV/cm$, which corresponds to the point of maximum M_r/M_s in Figure 3.29(c). The magnetization direction with positive or negative E_{DC} did not switch, but increased in value following a trajectory corresponding to the M-H loop (see Fig. 3.29(a)). After removing E_{DC}, two stable magnetization states were accessible depending on the E_{DC} direction.

These data in Fig. 3.30 (a) reveal strong coupling between the PMN-PT substrate and the BFO-CFO nanocomposite layer. The magnetic domains in the nanocomposite layer may rotate under $E_{DC} < 3\text{kV/cm}$, resulting in good E_{DC} tunable properties. The converse magnetoelectric coefficient (α) was then calculated from the data shown in Fig. 3.30 (a), using the equation: $\alpha = \mu_0 \frac{\Delta M}{\Delta E}$, where μ_0 is the permeability of free space, and α is in units of s/m. The value of α was estimated to be $1.3 \times 10^{-7}\ s/m$, again taken under $H_{DC} = 0$ in a previously magnetized state. This magnetization coupling coefficient is much higher than that previously reported (about 10^{-10} s/m) for $BiFeO_3$-$CoFe_2O_4$/$SrRuO_3$/$SrTiO_3$ heterostructures[83], and is close to values reported by Eerenstein et al.[124] for LSMO/PMN-PT (2×10^{-7}s/m). However, this prior investigation found those high values only over a limited temperature range[124]. Our results confirmed a large magnetoelectric coupling tunable under E_{DC}, which could be used over a wide range of temperatures below 375K.

Two different magnetization values were found to be stable upon removing E_{DC}, whose values were dependent on E_{DC} histories (see Fig. 3.30 (a)). To better illustrate these two states, the

value of the M_r/M_s ratio is shown as a function of E_{DC} in Fig. 3..30(b). We note that these data were obtained under $H_{DC} = 0$, beginning from a previously magnetized condition to M_r. The two different stable values of the M_r/M_s ratio found on removal of E_{DC} were $M_{-r0}/M_s = 0.31$ (after negative E_{DC}) and $M_{+r0}/M_s = 0.17$ (after positive E_{DC}), as illustrated by dashed lines in Fig. 3.30(b). After subsequent application of different E_{DC} (between 1 and 3kV/cm), these values did not change. The M_r/M_s ratio between M_{-r0} and M_{+r0} was 0.14. Previously in Fig. 3.29 (c), the difference in the M_r/M_s ratio value was shown to be $M_{-r0}/M_s - M_{+r0}/M_s = 0.46 - 0.35 = 0.11$, which is close to the value of 0.14. The trends were also consistent with the data in Fig. 3.29(d), where it can be seen upon removing E_{DC} that the E-induced strain relaxed, but its value under $E_{DC} = 0$ was different between positive and negative bias sweeps. The highest M_r/M_s ratio value was found to be ~ 0.60 at $E_{DC} = -3kV/cm$. The original state (M_0) was slightly larger than zero, which was due to equipment measurement error. These two different stable magnetization states accessible by E_{DC} offer a unique multi-state magnetization for logic and memory devices. The semi-volatile nature of the magnetostriction of the CFO nanopillars is due to changes in the phase stability of the PMN-PT substrate.

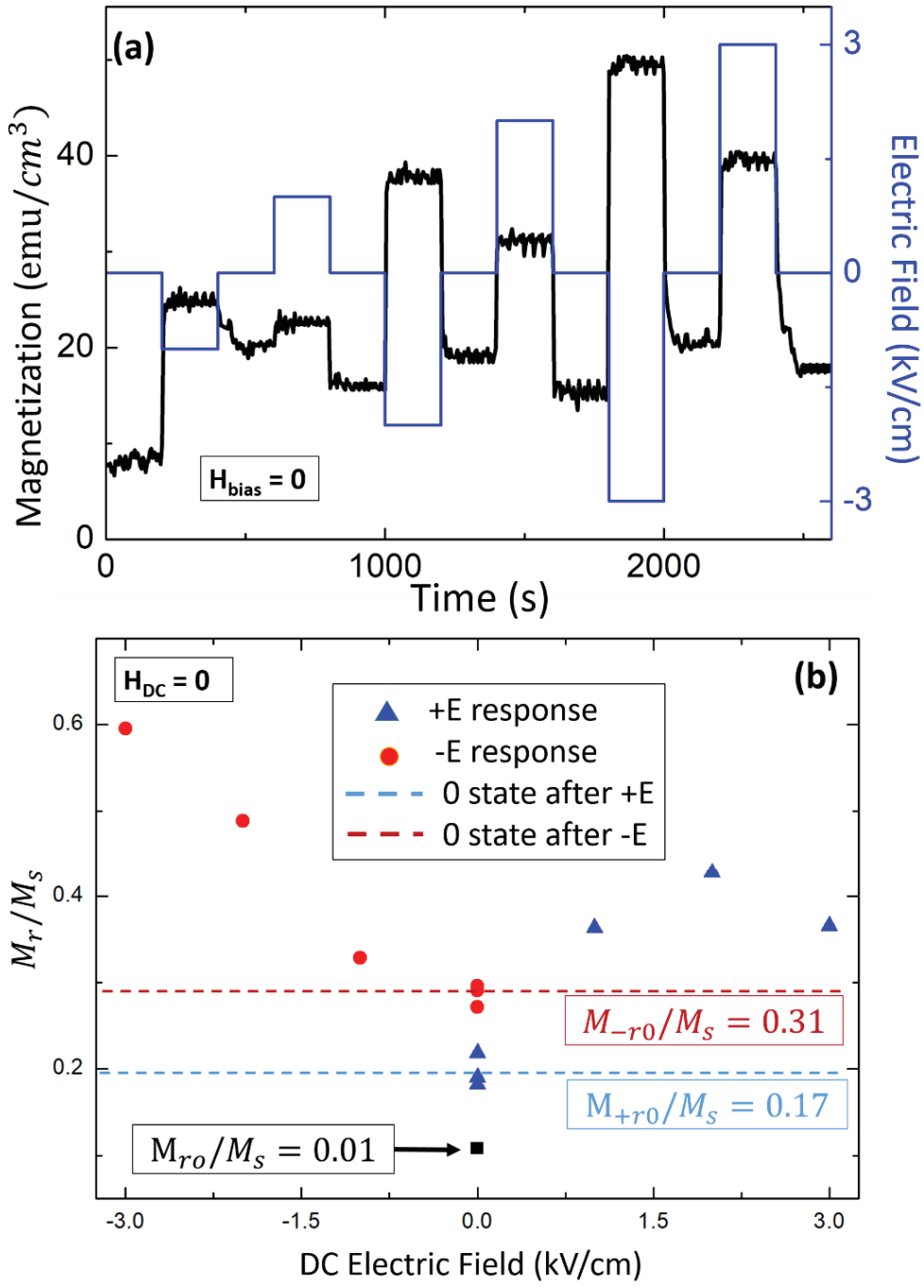

Figure 3.30. (a): Time vs. magnetization measurement under different magnetic fields. (b): Calculated M_r/M_s ratios under different E_{DC} and $H_{DC} = 0$ Oe, data are shown for both increasing and decreasing E-field sweeps.

These M_r/M_s ratio data clearly reveal three different states before and after E_{DC} (under $H_{DC} = 0$): M_{r0}, M_{+r0} and M_{-r0}, as shown in Fig. 3.31. These states correspond to the previously magnetized condition, beginning from M_{r0}. As also shown in Fig. 3.31, the dual combination of H_{AC} (or H_{DC}) followed by E_{DC} allow access to two additional oppositely magnetized states: $\overline{M_{+r0}}$ and $\overline{M_{-r0}}$. Thus, four or more ($N \geq 4$) stable remnant magnetization states can be accessed by E_{DC} in addition to M_{r0}. Prior studies of single-phase magnetostrictive thin films on PMN-PT, such as CoNi/PMN-32PT[40], have shown only two stable magnetization states. It should be noted, however, that one study of FeAl/PIN-PMN-PT heterostructures[23] reported four different states on removal of E_{DC} and H_{DC} that were accessed by $E_{DC} > 4kV/cm$. We note that our investigations were conducted in a vertically integrated, two-phase ME layer on PMN-PT for $E < 3kV/cm$. This vertically integrated heterostructure with multistate ($N \geq 4$) values was tunable by E_{DC} is more applicable for integrated memory and logic in comparison to the layer-by-layer ones. These multi-state heterostructures feature a high number of magnetic nanopillars and offer multiple stable magnetization states, which are accessible by E_{DC}. Moreover, they consume little power on changing states (i.e., they are passive). Thus, these multi-state heterostructures have the potential for neuromorphic-like applications.

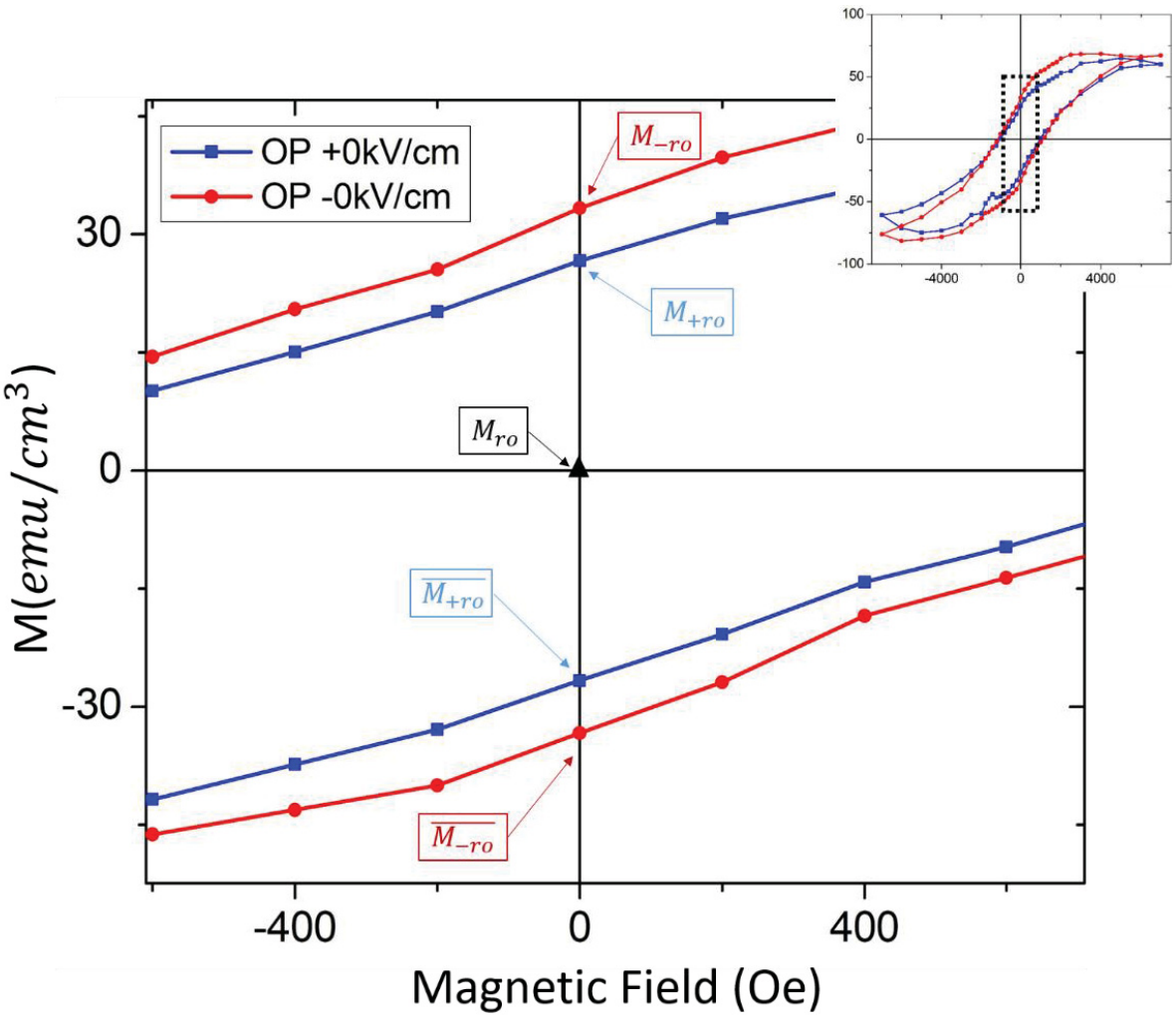

Figure 3.31. Enlarged M-H loop, showing magnetization states that accessible by different field histories. The enlarged portion is shown in the dashed square area in the insert at upper right corner.

3.6. BFO-CFO on Different Composition of PMN-PT

There are several approaches to further improve E-field-induced coupling and to increase the number of stable magnetization states. One is the composition of the PMN-xPT substrate and its proximity to the morphotropic phase boundary (MPB). Our substrates were in the T-phase field with x=38. However, compositions closer to the MPB (x=35) have monoclinic (M), tetragonal (T), rhombohedral (R) and orthorhombic (O) phases that are close in energy[79]. In this case, application of E_{DC} results in induced phase transformations, where the induced phase remains metastable on removal of E_{DC}; for example, the R→O phase transformation evident in PMN-32PT[78]. The availability of these metastable phases near the MPB offers the possibility of additional multistate magnetization values with E_{DC} for BFO-CFO/PMN-PT heterostructures. The second approach for improving E-field-induced coupling and increasing the number of stable magnetization states is by modifying the composition of the two-phase BFO-CFO target, which for this study was determined to be 65at%BFO/35at%CFO. By changing the composition of the BFO-CFO target, the aspect ratio of the CFO nanopillars could be modified, which would result in a change in the shape anisotropy (K_{shape}). A previous report has shown that by increasing the aspect ratio of the CFO nanopillars (from 3:1 to 5:1), the values of M_r and H_C along OP could be significantly increased. Increasing K_{shape} could also help stabilize additional non-volatile multi-state magnetization values[39].

Fig. 3.32 shows the AFM and related MFM images for the BFO-CFO/SRO/PMN-x%PT sample. Fig. 3.32 (a) to (c) confirms that self-assembled square-like nanopillars were obtained using the PLD technique. The MFM images shown in Fig. 3.32 (e) to (f) illustrate the presence of magnetic signal from these nanopillars, which are similar to those obtained in previous work from our group[66]. From the images, one can see that the magnetic signals observed as a dark and light

contrast for the different nanopillars are different, indicating randomly oriented magnetic domains because the sample was not poled prior to the MFM measurements.

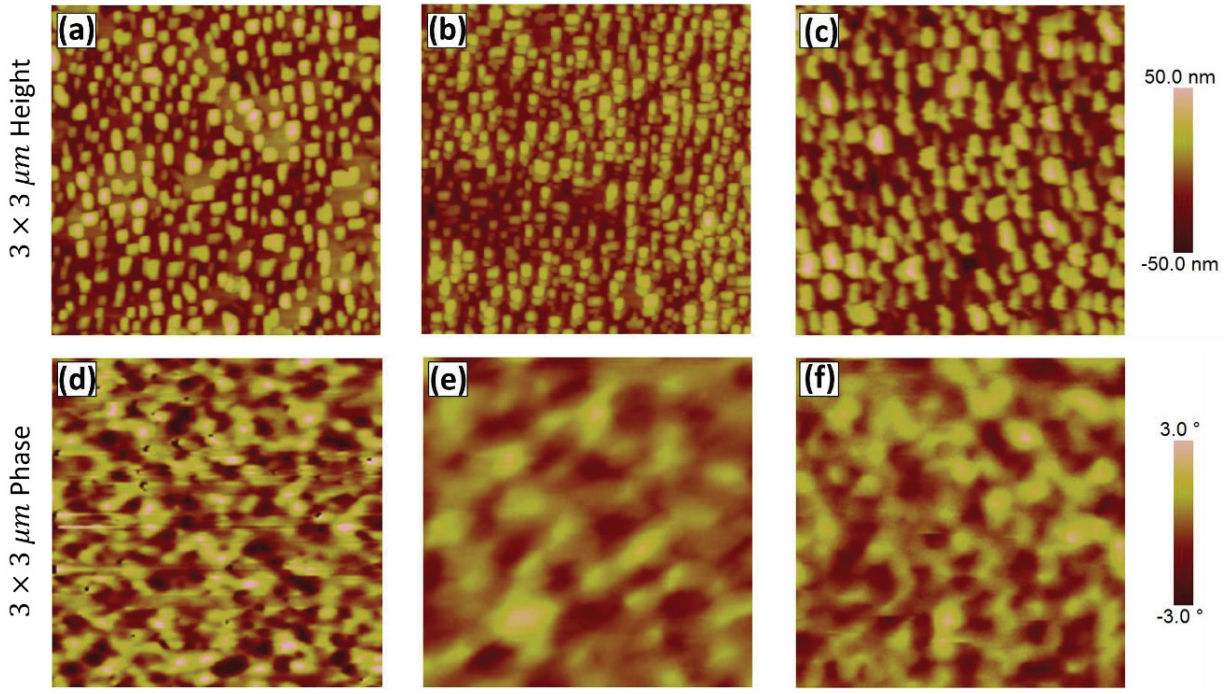

Figure 3.32. (a), (b) and (c), BFO-CFO heterostructures AFM images on PMN-33PT, PMN-35.5PT and PMN-38PT substrates, respectively.

For the PMN-x%PT, the XRD scan in Fig. 3.33 shows a T phase structure, which corresponds with the 'a' and 'c' ferroelectric domains in the PMN-PT substrates[125]. According to Rewadee et al.[126], PMN-x%PT single crystal becomes tetragonal when x% is greater than 32%. However, PMN-33PT and PMN-35.5PT are landing around the morphotropic phase boundary (MPB), and the composition is a mixture of monoclinic B and tetragonal phase[79]. The results illustrated in Fig. 3.33 uphold this conclusion. From the Fig. 3.33 we can see that the peaks for the CFO and BFO on different PMN-PT substrates have different d-spacing values, which correspond with the strain

coupling on different substrates. The degrees and d-spacing information are listed in Table 3.5. The calculation in Table 3.5 is based on $\varepsilon = (d_m - d_0)/d_0$, where d_m is the measured d-spacing, d_0 is the bulk d-spacing (d_0 for CFO is 8.392 Å[88], for BFO is 3.960 Å [85]). In Table 3.5 we can see that the strain for the CFO is different on the three different substrates: PMN-35.5PT, PMN-38PT, and PMN-33PT in order of decreasing strain. These data are also reflected in the 0kV/cm M-H loop for the three samples (see Fig. 3.34 (a)-(b)). For the (100) CFO, the magnetostrictive coefficient was negative along the (100) direction [127]. Thus, when d spacing along the OP direction (this is the measured direction from XRD) increases, the IP direction will undergo a compressive strain. This compressive strain in combination with the negative magnetostrictive coefficient will cause the domains to move from the OP to the IP direction[128]. From the original M-H loop one can see that the PMN-35.5PT sample, which has the highest strain along the OP direction, also has the lowest coercivity along the OP direction. This finding indicates that the domains are oriented in the IP direction.

Table 3.5. Lattice parameters for BFO, CFO peaks on different PMN-xPT substrates.

		Degree (°)	d-spacing (Å)	FWHM (°)	Strain (%)
PMN-33PT	CFO	43.15	8.379	0.144	-0.143
	BFO	45.89	3.952	0.461	1.255
PMN-35.5PT	CFO	43.01	8.365	0.346	-0.310
	BFO	46.20	3.927	0.346	0.615
PMN-38PT	CFO	43.17	8.376	0.010	-0.179
	BFO	45.71	3.967	0.269	1.640

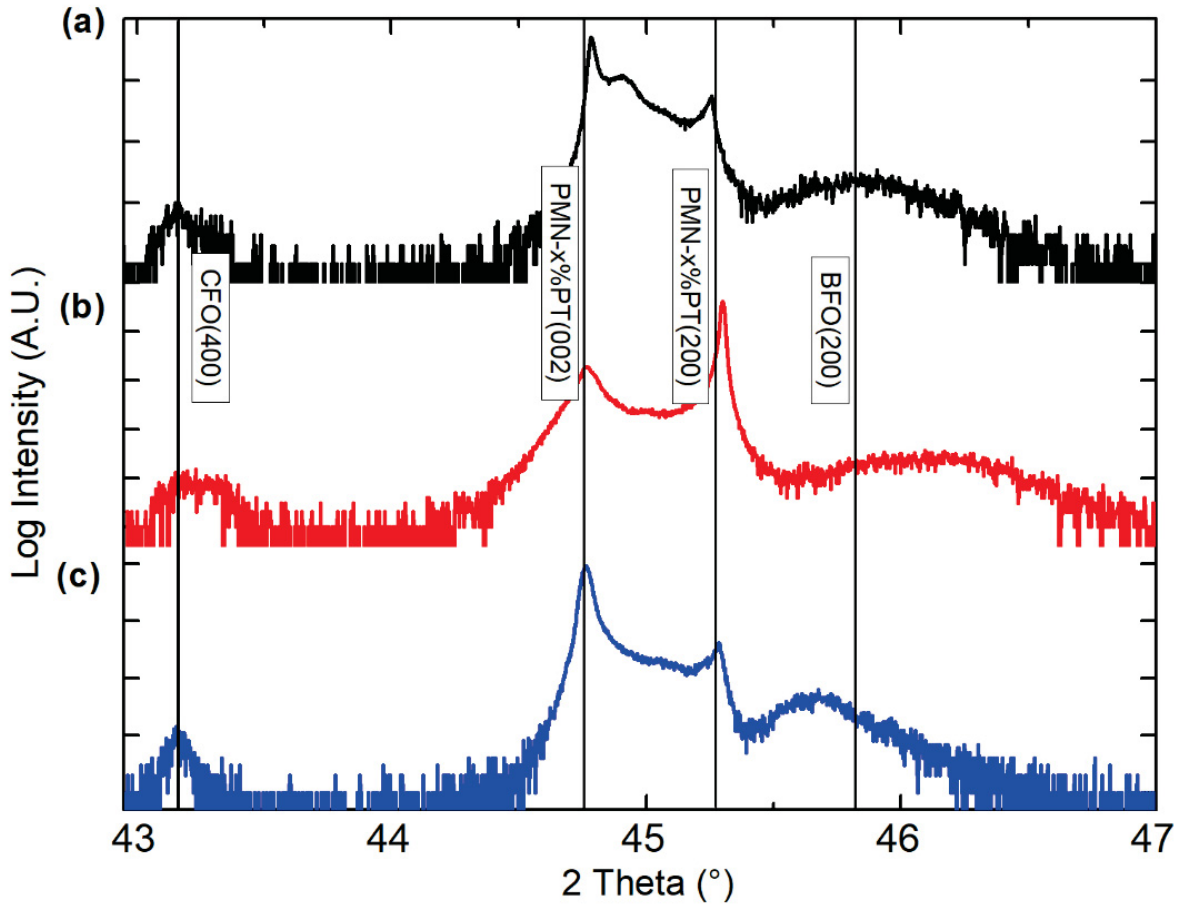

Figure 3.33. 2θ scan for BFO-CFO/SRO/PMN-x%PT. (a) PMN-33PT, (b) PMN-35.5PT, (c) PMN-38PT.

Another interesting field of inquiry is to see how the presence of an E-field affects magnetization in these PMN-x%PT samples. To study this influence, a real-time magnetization measurement was conducted. Specifically, E-fields were applied in the out-of-plane direction and magnetization was measured using a VSM, as shown in Fig. 3.34. The electric field was first ramped up to 6kV/cm, then decreased to -6kV/cm, and finally was ramped back to 6kV/cm again to form a loop for the OP direction. For the IP direction, the E field was ramped up to 2kV/cm, then was decreased to -2kV/cm, and finally was ramped back to 2kV/cm. The corresponding directions are shown by the arrows in Fig. 3.34 (d)-(f). In order to clearly show the change, selected results are shown in Fig. 3.34 (a)-(c). As indicated in these figures, only the M-H loops displaying the maximum change under certain E-fields were chosen to elaborate the magnetization change.

From these figures, one can see that remnant magnetization was altered via the introduction of an E-field for the PMN-33PT, PMN-35.5PT, and PMN-38PT samples. Normally, the easy axis lies in the in-plane direction for the thin-film heterostructures, because the thickness is much smaller than the width for a single-phase sample[129]. However, the nanopillar structure features much larger thickness than width within each nanopillar. Therefore, the OP direction is the easy axis for BFO-CFO/PMN-x%PT heterostructure, and the magnetic domains tend to flip upside-down in a nanopillar. As an outcome of this reversal in domain flipping, there are not many magnetic domains moving around the IP direction, which causes minor magnetization change around the IP direction. And the domains tend to flip to the OP direction due to the introduction of an E-field and a reduction in domains at the IP direction.

In order to illustrate E-field-introduced magnetization change clearer, the M_r/M_s ratio for the different samples were plotted, as shown in Fig. 3.34 (d)-(f). The IP direction M-H loop figures, as shown in the upper-left insert of Fig. 3.34 (a), (b) and (c), did not undergo a significant change

with the introduction of an E-field. The applied OP voltage created a tensile strain along the IP direction, which will transfer to the CFO layer. This E-field-induced transfer can significantly impact magnetic properties—notably, coercivity (H_c) and remnant magnetization (M_r)[123,130]. As illustrated in Fig. 3.34 (d)-(f), we can see that the PMN-x%PT substrates are under compressive stress along the OP direction with applied E-field, which induces tensile stress along the IP direction for these BFO-CFO two-phase systems. Therefore, a negative magnetostrictive coefficient for the CFO along the (100) direction will resist the easy axis along the IP direction, which creates a larger M_r[123].

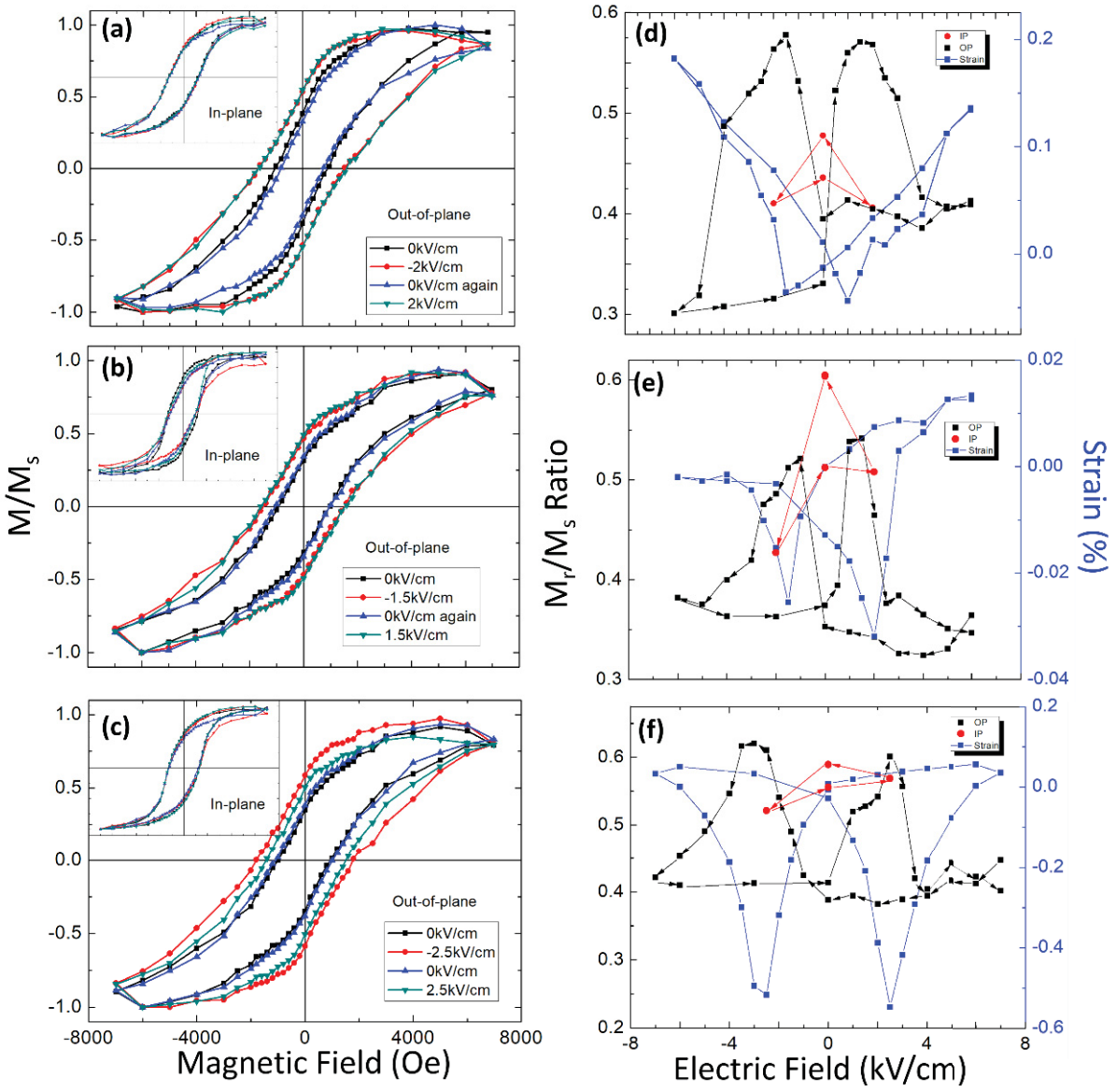

Figure 3.34. Magnetization measurements for BFO-CFO/SRO/PMN-x%PT. (a)-(c): M-H loop under different E-fields for PMN-33PT, PMN-35.5PT and PMN-38PT respectively. (e)-(f): Mr/Ms ratio for PMN-33PT, PMN-35.5PT and PMN-38PT, respectively.

3.7. Summary

In summary, self-assembled nanopillar BFO-CFO two-phase layers have been deposited on SRO buffered PMN-xPT (100) substrates (x=33, 35.5, 38). The epitaxial growth of the vertical two-phase layers was confirmed by XRD, and a dense nanopillar surface was observed in AFM/MFM images. Large magnetization changes under applied E_{DC} were found along the easy magnetization axis, where the M_r/M_s ratio exhibited a butterfly loop with E_{DC}. The value of $\Delta M/M_{rDC}$ was calculated, and the maximum was found to be $\sim 90\%$. The converse magnetoelectric coupling coefficient was calculated to be 1.3×10^{-7}s/m. Real-time changes in the magnetization with E_{DC} were measured, and multiple stable magnetization states ($N \geq 4$) were found on the removal of field. These heterostructures shows the potential to have multiple magnetic states and thus would be appropriate for incorporation in high-density memory devices.

CHAPTER 4: NANOSTRUCTURE-ENHANCED MAGNETOEELTRIC PROPERTIES AND REDUCED LOSSES IN SELF-ASSEMBLED EPITAXIAL CUFO-BFO/PMN-33PT CRYSTALS

4.1. Overview of CuFO/PMN-PT and BFO-CuFO/PMN-PT

Magnetoelectric materials offer several potential advantages in various applications[23,61,115]. One important feature for these devices is the mechanical quality factor (Q), which is often used as a measure of energy loss per-cycle[89,90] and/or the efficiency[91,92] with higher Q values generally implying higher efficiencies and lower losses. Although some bulk magnetostrictive materials such as $CoFe_2O_4$ feature large magnetostriction (λ_m), they also experience relatively high losses[127]. Prior studies investigating epitaxially-deposited single-crystal magnetostrictive thin films on substrates have attempted to achieve both high Q and high λ_m[75,97], but these goals have been difficult to achieve simultaneously[97]. Nonetheless, Howe et al.[99] recently reported an optimum tradeoff between high Q and λ_m for NiZnAl-ferrite.

As noted in the previous section, the (1-3) heterostructures have many advantages, especially in terms of their high ME coupling[58,60], as well as magnetic shape anisotropy due to the nanopillar geometry[39,45,61]. Although the spinel ferrite CFO has a large λ_m, it also displays high coercivity that leads to high losses and low Q[102,131]. High losses dramatically reduce energy/power efficiency and decrease the usefulness of their tunable features[90,92]. Traditional BFO-CFO (1-3) heterostructures have been studied (and shown in the Chapter 3. However, CFO has a much larger coercivity field, which leads to a much higher loss and low Q factor. A lower loss spinel ferrite is needed in such nanopillars to overcome these limitations.

Copper ferrite ($CuFe_2O_4$, CuFO) has been shown to demonstrate low loss and high Q-factors at the ferromagnetic resonance (FMR) frequency, as mentioned in Chapter 2. However, the

magnetostriction of the layers has not been sufficiently studied. Such CuFO thin films deposited on $MgAl_2O_4$ (MAO) could suffer from both mechanical clamping effects and current leakage, resulting in reduced magnetostriction. In addition, CuFO features a lattice parameter that might allow matching to BFO for vertical integration, as well as to $Pb(Mg_{1/3}Nb_{2/3})_{1-x}Ti_xO_3$ (PMN-xPT) as a substrate. Thus, it offers an approach for fabricating ME heterostructures with reduced loss potential, and significant λ_m and ME exchange.

Here, we report a self-assembling two-phase vertically integrated BFO-CuFO heterostructure, which was epitaxially deposited on $SrRuO_3$ buffered $Pb(Mg_{1/3}Nb_{2/3})_{0.68}Ti_{0.32}O_3$ (SRO/PMN-33PT) substrates by SPLD. These BFO-CuFO heterostructures were found to possess relatively large magnetization changes with E, indicating that the CuFO layer had significant λ_m values. This is in contrast to CuFO layers on PMN-33PT, which demonstrate little to no dependence of M on E_{DC}. Multiple remnant magnetization states were also identified upon removal of E_{DC}, which were dependent on electric history.

4.2. Experimental Method

Single-layer CuFO and vertically integrated CuFO-BFO layers were epitaxially deposited on PMN-33PT substrates by PLD. Self-assembled thin films were deposited by SPLD. BFO and CuFO targets were purchased from Kurt J. Lesker Company, and both were >99.9% in purity. Single-crystal PMN-33PT (100) substrates were grown at the Shanghai Institute of Ceramics, Chinese Academy Sciences, and polished according to the process detailed in Section 2.1.1. Prior to deposition, the substrates were cleaned with acetone and alcohol via ultrasonication. First, a 30nm SRO layer was deposited on PMN-33PT at 700℃, using an energy density of 1.5 J/cm^2 and an O_2 atmosphere of 150 mTorr, which was followed by annealing at 700℃ and 150 mTorr O_2 for

10min. Single CuFO layers were deposited at 700°C using an energy density of 1.2 J/cm^2 and an O_2 atmosphere of 150 mTorr for 50min. Self-assembled CuFO-BFO layers were deposited as a volume fraction of about 40:60. First, a BFO single layer was deposited at 700°C using an energy density of 1.2 J/cm^2 and an O_2 atmosphere of 150 mTorr for 2 min 48s. The target was then switched to CuFO, and deposition was conducted for 2min 12s at 700°C, 1.2 J/cm^2 and 150 mTorr to form a bilayer structure. This procedure was repeated 10 times, forming a film with a total thickness of about 130nm. The sample was then annealed at 700°C and 100 Torr O_2. Atomic force microscopy and magnetic force microscopy images were obtained (Dimension 3100, Vecco) to study the film surface quality and magnetic domain structures. Cross-sectional samples were fabricated by focused ion beam (FIB, FEI Helios 600 NanoLab). Cross-sectional images, selected area electron diffraction patterns (SADP) and x-ray spectra (EDS) were obtained using transmission electron microscopy (JEOL 2100). Crystal structures were determined by X-ray diffraction (Philips X'Pert system) and SADP. Magnetic hysteresis curves were recorded by a vibrating sample magnetometer (VSM, Lakeshore 7300 series).

4.3. Single Phase CuFO/PMN-PT and Nearly Neglectable ME Effects

Figure. 4.35 summarizes the structure and ME properties of the CuFO/SRO/PMN-33PT heterostructures. Part (a) provides a cross-sectional TEM image, which exhibits formation of a single layer with no apparent nanostructures. Part (b) shows a SADP taken along the [010] zone axis. The red circled spot in the figure clearly illustrates that an epitaxial CuFO single layer was formed on top of the PMN-33PT substrate. The PMN-33PT lattice parameters calculated from Fig. 4.35(b) were 4.03Å, which is similar to previous reports[78,79]. A splitting along the (400) zone can be seen in the SADP, which are the CuFO (004) and (400) peaks. This evidences that the CuFO

layer had a tetragonal (T) structure, which is different than the cubic (C) one recently reported for CuFO on $MgAl_2O_4$ (MAO)[97]. The lattice parameters of CuFO were determined from the splitting to be $(a_{T-CuFO}, c_{T-CuFO}) \cong (8.26, 8.67)$Å. This is similar to, but not exactly the same as, the bulk CuFO lattice parameter of $c_T = 8.73$Å[132]. The CuFO layer undergoes a compressive strain along the c-axis of ~0.68%.

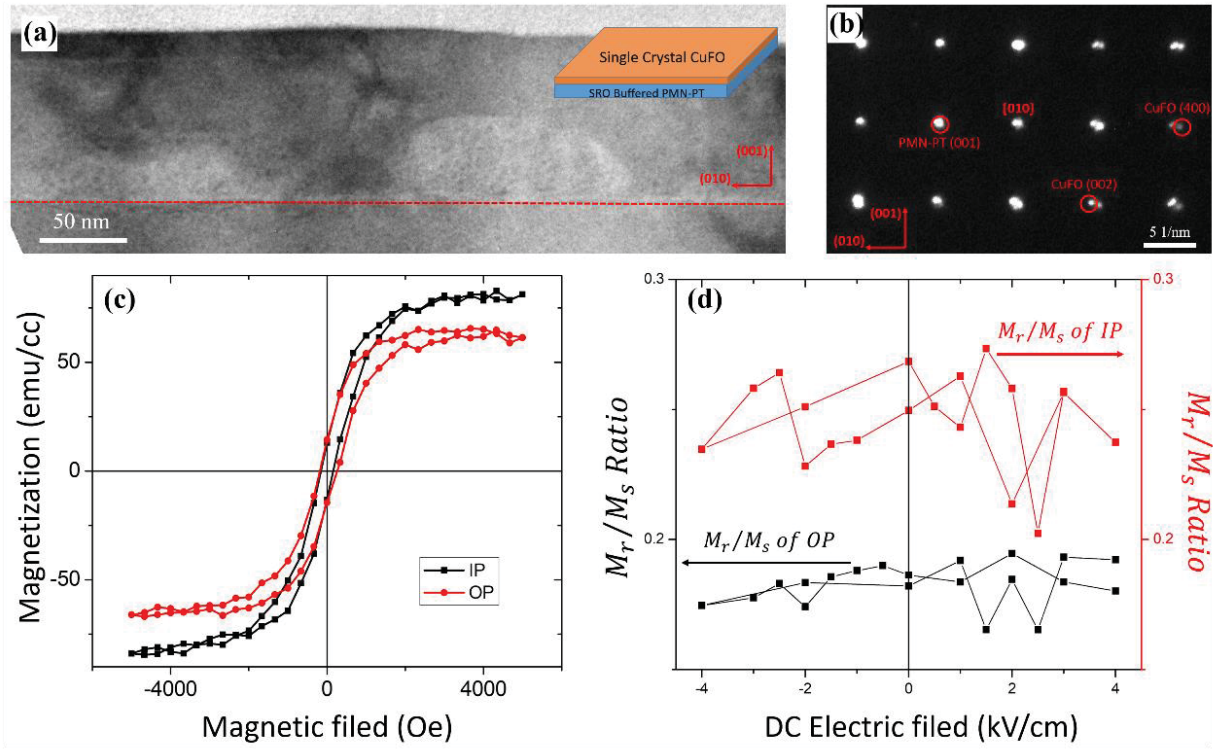

Figure 4.35. (a) TEM cross-section image of single crystal CuFO/SRO/PMN-33PT heterostructure. Insert figure at up right corner shows a schematic of this heterostructure. (b) Electron diffraction pattern of this cross-section. (c) VSM data for this single layer CuFO/SRO/PMN-33PT, both IP and OP directions. (d) E-field dependence of magnetization of CuFO/SRO/PMN-33PT, both IP and OP directions.

Figure 4.35 (c) shows a magnetic hysteresis loop for CuFO/SRO/PMN-33PT, along both in-plane (IP) and out-of-plane (OP) directions. The easy axis of the magnetization aligned along the IP, and exhibited a typical M-H hysteresis loop. The saturation magnetization was $M_s \approx 60 - 70\, emu/cm^3$, and the remnant magnetization was $M_r \approx 15\, emu/cm^3$. Zhang et al.[97] previously reported epitaxial growth of CuFO films on MAO with $M_s \sim 60\, emu/cm^3$ and $M_r \sim 20\, emu/cm^3$, similar to those reported here on PMN-33PT. The coercivity of our films was $H_C \approx 150\, Oe$ along both the IP and OP directions. The value of H_C along the easy axis was previously reported to be ~30-40 Oe for CuFO powders[133], ~23 Oe for a 50nm CuFO single-crystal films[97], and ~250 Oe for 450nm single-crystal films[96]. Figure. 4.35 (d) shows an M-H loop for CuFO/SRO/PMN-33PT under various applied DC electric fields (E_{DC}), taken along the OP and IP directions. As can be seen in the figure, the magnetization was essentially independent of E_{DC} over the range of 0 to 4kV/cm, where PMN-33PT is known to experience significant E-field-induced strain. This finding demonstrates that the CuFO has little magnetoelectric coupling, thereby indicating negligible magnetostriction.

These results demonstrate that CuFO layers can be epitaxially deposited on PMN-33PT. The CuFO layers have a similar T crystal structure, lattice parameters, and M_r and M_s values as bulk crystals. However, the heterostructures clearly demonstrated the lack of magnetoelectric exchange, and thus, by inference, the CuFO magnetostriction is very small. These results are discussed here because the nanostructures of vertically-integrated layers on the same substrate will be reviewed in order to show how they are capable of imparting these missing characteristics to the heterostructure.

4.4. Surface Quality of the BFO-CuFO/PMN-PT Nanocomposite

Figure. 4.36 (a) provides an AFM image of a BFO-CuFO film surface. One can clearly see a nanostructure topography embedded in a matrix. The morphology consisted of an apparent mixture of nanopillars (surface dimensions of about $100\text{nm} \times 100\text{nm}$) and nanobelts (surface dimensions of about $10^3\text{nm} \times 100\text{m}$). The nanopillars and nanobelts appeared to have similar geometries and aspect ratios, wherein the pillars lay vertical to the substrate plane and the belts horizontal. This mixed nanobelt-nanopillar morphology appeared to be stable, as shown in Fig. 4.37. Similar AFM topographies were obtained for heterostructures annealed over a significantly longer period (60min).

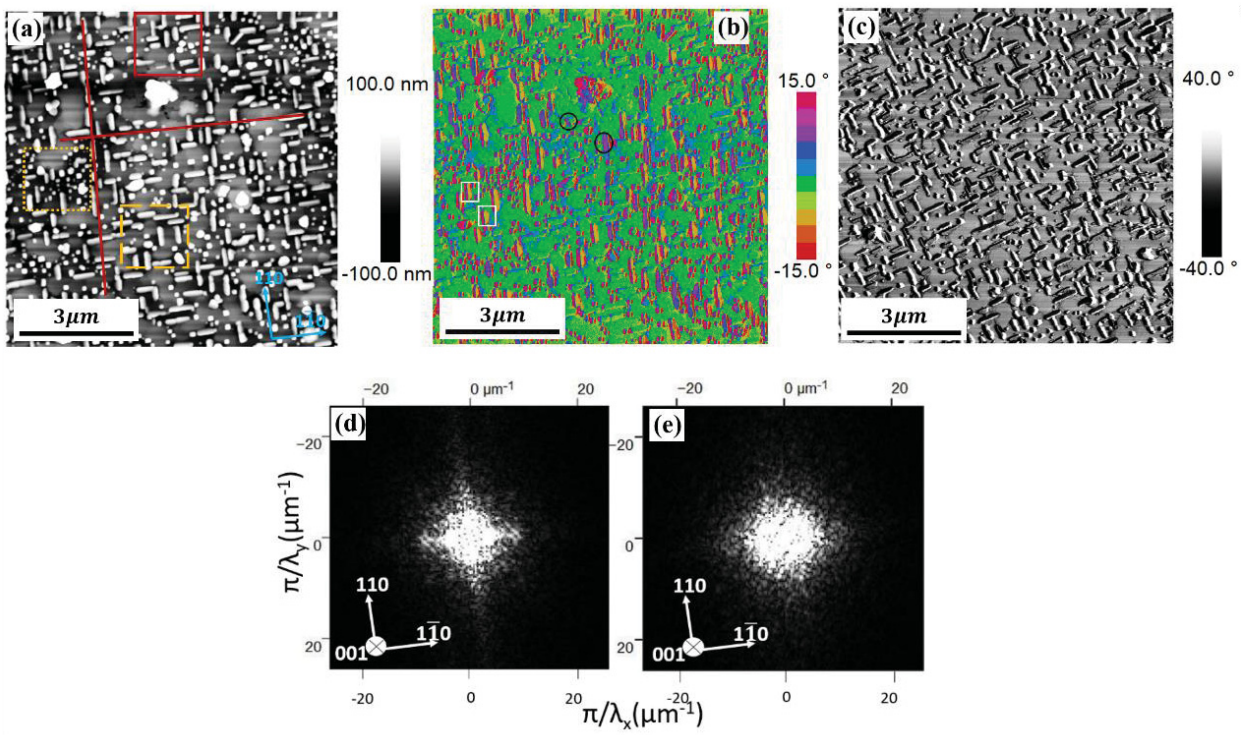

Figure 4.36. (a): Height information of nanopillar structure topography. (b): Magnetic phase signal of MFM scan, showing different magnetic domains in different nanopillars, and matrix without significant magnetic phase signal. (c): Phase image shows different materials of nanopillar (black or white color) and matrix (grey color). (d) & (e): FFT analysis. (d): FFT of yellow dashed area in Fig. 1(a), and (e): FFT of yellow dotted area.

Figure. 4.36 (b) shows corresponding MFM images for the phase response. As identified in Fig. 4.36 (b), the black circled area has a positive phase signal, whereas the white squared area has a negative phase signal. These represent the magnetic signal contributions from different magnetic domain orientations within the nanostructure. The sample was not yet poled by a magnetic field, and the magnetic domains in the CuFO nanopillars were oriented amongst symmetry equivalent directions. Most of the area was covered by the matrix phase, which is shown as green to blue colors in the phase image. These regions represent low contrast areas close to the noise level in the

scale bar, which impart negligible contributions to the magnetic signal[106]. Presumably, this is due to the fact that the BFO phase magnetic signal is small. An AFM phase image scan is shown in Fig. 4.36 (c), which helps to distinguish the presence of the two phases on the surface. The AFM phase image plots a contour of the surface layer stiffness. Such contrast can be used to distinguish different phases and their distributions on the surface. In Fig. 4.36(c), it can be seen that the phase signals of the nanopillars/nanobelts were either dark (close to $-40°$ in the scale bar) or white (close to $+40°$). This result is totally different from the matrix area, which is illustrated as grey in the image (middle of scale bar).

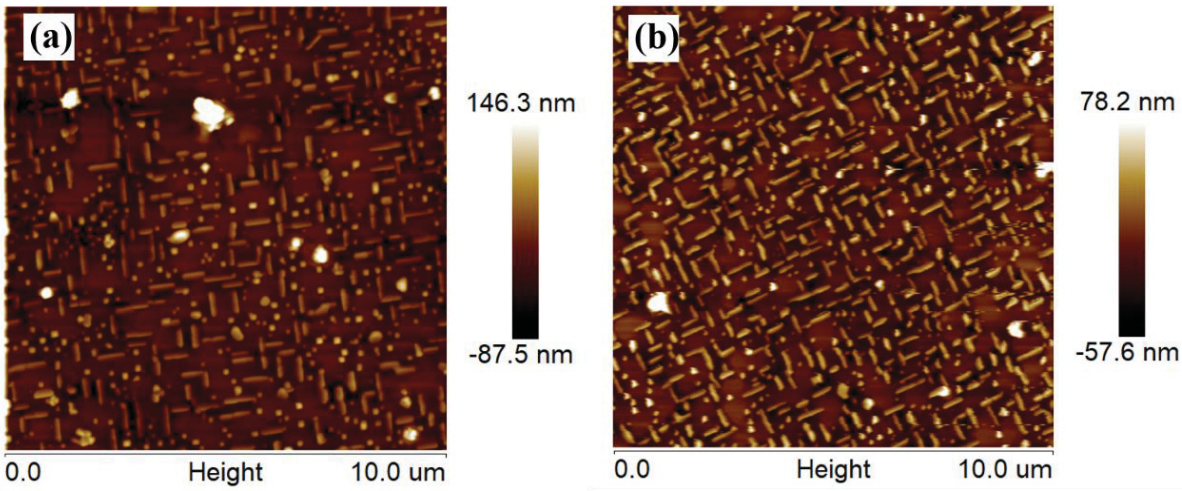

Figure 4.37. Surface structure for BFO-CuFO/SRO/(100)PMN-33PT under different annealing time. (a): Anneal for 30min. (b) Anneal for 60min.

Next, we considered the distribution of the nanobelts and nanorods, as shown in Fig. 4.36 (a), which was quite regular across the surface. The belts were elongated along the <110> and <$1\bar{1}0$> family of directions. Additionally, they were somewhat regularly spaced, with a tendency to align with neighboring belts. Fine red lines are given in the image to guide the eyes to the rectilinear regularity of the nanobelt morphology. Vertical nanorods with a square shape appeared to collect within areas surrounded by the nanobelts, and had some tendency to align with respect to each other along the <001> directions, as illustrated by a fine red box in the image. A fast Fourier transform (FFT) image that corresponds to the domain distribution is given in Figure 4.36 (d) & (e), where π/λ_x and π/λ_y are the wave-vectors along the x- and y- directions, respectively. Fig. 4.36 (d) was taken from the area covered by the dashed yellow box, which is a region containing mostly nanobelts. The FFT image can be seen to be strongly oriented along the <110> and <$1\bar{1}0$> directions, demonstrating a significant degree of self-organization of the nanobelts into a quasi-periodic morphology. The average inter-spacing between nanobelt features π/λ_x and π/λ_y was determined to be about 174nm. We next obtained a FFT from the area defined by a dotted yellow box, which corresponds to a region containing mostly nanorods, as shown in Fig. 4.36 (e). The FFT image revealed some degree of orientation along the <001> direction, in addition to a halo that was quite diffuse and symmetric about the x- and y-axes.

4.5. Cross-sectional Study of the BFO-CFO/PMN-PT Nanocomposite

A cross-sectional image of the nanopillars and nanobelts was then obtained by TEM, as given in Fig. 4.38 (a). From the figure, we can see that the vertically integrated two-phase layer of the heterostructure consisted of nanopillars and nanobelts. The edge of the thin film layer was distinct, exhibiting no inter-diffusion of film and substrate. The image shows that the nanobelts and nanorods extend throughout the thickness of the film from the substrate, and that the nanobelts are uniform regions rather than closely spaced nanorods. These results clearly demonstrate that the distribution of CuFO in BFO consists of a mixed morphology between nanorods vertically integrated from the substrate and nanobelts laying in the plane. From Fig. 4.38 (a), one can also observe that the nanopillars and nanobelts of CuFO extend out from the surface of the BFO matrix. This stretching-out of nanopillars has commonly been observed for vertically-integrated nanocomposites[134]. However, in the case of CuFO nanostructures, the analogous extension was nearly half of the matrix thickness, which may be driven by relaxation of epitaxial strain due to the large lattice mismatch with the BFO matrix. As shown by the red dashed line in Fig. 4.38 (a), the CuFO nanostructures also exhibited a particular faceted angle with respect to the matrix, which was about 55 to 60°. This angle may reflect a balance of wettability and strain interactions between nanostructures and the matrix[70].

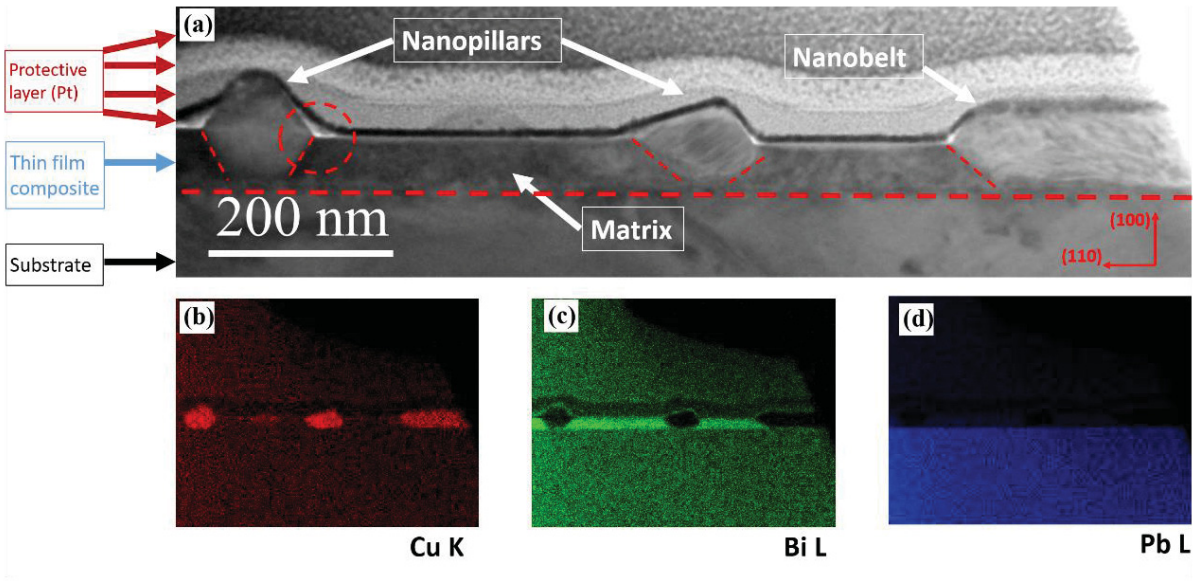

Figure 4.38. Cross-section images taken by TEM. (a): Cross-section bright filed image containing 2 nanopillars and a nanobelt. (b). EDS mapping for element Cu, (c) Bi and (d): Pb.

In order to determine the composition of the nanobelts, nanorods, matrix, and substrate, energy-dispersive x-ray spectroscopy (EDS) was performed on the sample. EDS plots for each of these regions are given in Figures 4.38 (b)-(d). According to the results shown in Fig. 4.38 (b) and (c) one can see that there is no elemental Cu in the matrix phase, and no elemental Bi within the nanopillar/nanobelt phase. These plots thus demonstrate that the composition of the nanobelts and nanorods are CuFO, that the matrix is BFO, and that no secondary phases form at the interfaces between the nanostructures and the matrix. The EDS plot in Fig. 4.38 (d) demonstrates the presence of elemental Pb in the substrate composition; moreover, consistent with the bright field image, the heterostructure film was clearly distinct from the PMN-33PT substrate. Fig. 4.39 also shows EDS mapping for the element Sr. The buffer layer SRO lies in-between the thin-film heterostructure and substrate, which again demonstrated no mixed phases.

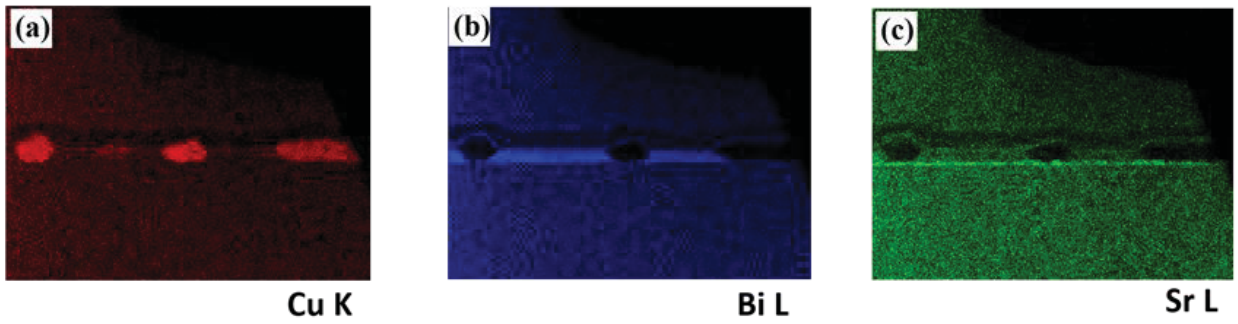

Figure 4.39. EDAX mapping for different elements: (a) Cu, (b) Bi and (c) Sr.

4.6. HRTEM and Epitaxy of the BFO-CFO/PMN-PT Nanocomposite

Figure 4.40 provides a high resolution TEM (HRTEM) image taken from the area labeled by the dashed red circle in Fig. 4.39 (a). The HRTEM image shows an area having both a CuFO nanopillar and BFO matrix, where the boundary between them is labeled by a red dashed line. The separation of the two phases was clear, demonstrating no inter-diffusion of the BFO and CuFO phases or secondary phase formation at the boundaries. The HRTEM image also evidences the lattice periodicity of both phases. Two pairs of white dashed lines in Fig. 4.40 (a) illustrate the d-spacings of the CuFO and BFO ($d_{CuFO} = 4.20$Å), which corresponds to the CuFO (002) plane, and $d_{BFO} = 3.87$Å, which is that for the (001) BFO. These values are consistent with those of bulk CuFO and BFO phases. The image reveals registry of the lattice phases across the interphase interfaces, demonstrating good epitaxy between CuFO and BFO phases in the self-assembled layer. The insert in the lower left corner of Fig. 4.40 (a) shows a dark field image taken from a CuFO nanopillar. This image reveals the presence of an array of nanotwins along the (001) direction, which were about 5-10nm in width and 50nm in length. Such high twin wall densities can only arise when the twin wall energy is $\gamma \to 0$. This energy relaxing can play an important role in

softening the elastic constant and relaxing elastic energy[135,136], and in stabilizing the self-assembled nanostructure.

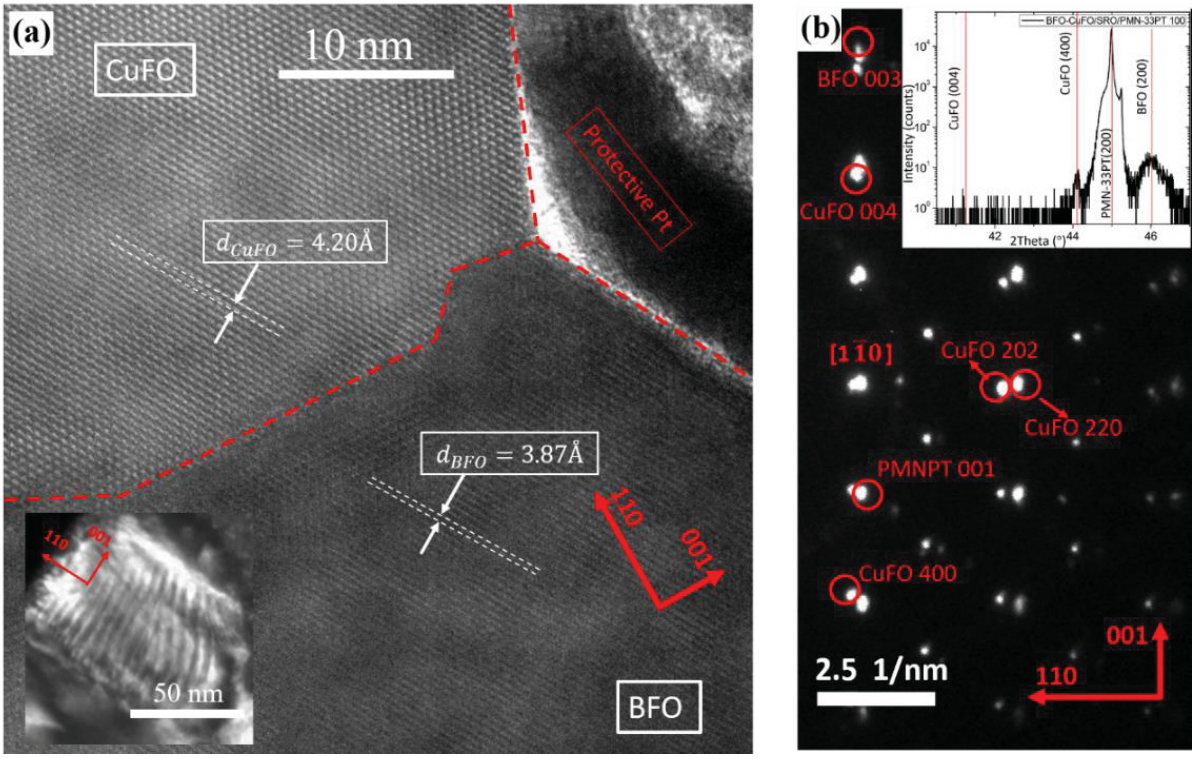

Figure 4.40. (a): Enlarged area of dashed circle in Fig.4 (a). White dashed line shows the interplanar spacing of both CuFO and BFO. Insert shows dark field images of this nanopillar, illustrating a periodical line structure. (b): Corresponding diffraction pattern of selected area.

Figure. 4.40 (b) shows a SADP taken from Fig. 4.39 (a) along the $[1\bar{1}0]$ zone axis. A splitting can be seen in the SADP, which evidences that the CuFO phase in the self-assembled layers had a tetragonal (T) structure. The lattice parameters of the CuFO phase was calculated from the SADP and determined to be $(a_{T-CuFO}, c_{T-CuFO}) \cong (8.20, 8.60)$Å. Compared to the bulk CuFO lattice parameters, a significant compressive strain was induced along the c-axis (~1.5%), which was noticeably larger than the strain in single CuFO layers (~0.68%), as mentioned above. A splitting

in the diffraction pattern was also found along the (003) BFO peak, as labeled in Fig. 4.40 (b). The lattice parameter was calculated to be $a_{BFO} = 3.95\text{Å}$, which is close to the bulk BFO value of the rhombohedral (R) phase ($\mathrm{d} = 3.96\text{Å}$). The insert in the upright corner of Fig. 4(b) shows a corresponding X-ray line scan. The BFO (200) peak was located at 46.07° ($a_{BFO} = 3.938\text{Å}$), and the CuFO (400) was found at 44.14° ($a_{T-CuFO} = 8.200\text{Å}$), yielding similar results to those determined by SADP. However, there was no evidence of the CuFO (004) peak (i.e., c_{T-CuFO}) in the XRD line scans.

One can presume that the self-assembly of the mixed nanostructure state is driven by the minimization of the elastic strain energy, similar to the relationship for vertically integrated nanopillar structures previously modeled by phase field theory[59]. This mixed morphology was distinctly different than that of CFO-BFO on SRO/STO or SRO/PMN-PT, where a nanopillar structure forms on (001) substrates and a nanobelt one on (110)[58]. This difference points to the potentially important role of the tetragonal lattice parameters of CuFO single crystals (large $\mathrm{c/a} \approx 1.06$), relative to the cubic ones for CFO, as a driving force for the mixed morphology.

4.7. Enhanced Magnetic Properties in BFO-CFO/PMN-PT Nanocomposite

Figure 4.41 (a) shows M-H loops taken along both the IP and OP directions by VSM. The saturation magnetization (M_s) was about 34 emu/cm^3 along both directions, and the remnant magnetization was $M_r = 11.3\ emu/cm^3$ and 9.7 emu/cm^3 along the OP and IP directions, respectively. Since the CuFO-BFO volume ratio was about 40:60 and since the antiferromagnetic BFO phase does not contribute to induced magnetization, the values of M_s and M_r of the CuFO nanopillars can be estimated to be about $50emu/cm^3$ ($1.5 \times 30emu/cm^3$) and $15emu/cm^3$ ($1.5 \times 7.5emu/cm^3$), respectively. These values are nearly equivalent to those previously reported for epitaxial CuFO films on MAO[97], and to values shown in Section 3.1 for CuFO/SRO/PMN-33PT. From Fig. 4.41 (a), the coercivity along the IP and OP directions was determined to be 430 Oe and 700 Oe, respectively. These values are significantly larger than those for single layer CuFO/SRO/PMN-33PT (see Fig. 4.36 (c)), but much lower than those previously reported for CFO-BFO/SRO/PMN-PT[10]. It was expected that the easy axis would be along the IP direction; instead it was found along the OP direction. This difference is undoubtedly due to nanobelt/nanopillar-induced changes in the magnetic shape anisotropy. A large shape anisotropy contribution can dominate magnetic anisotropy, changing the easy axis from IP to OP[39].

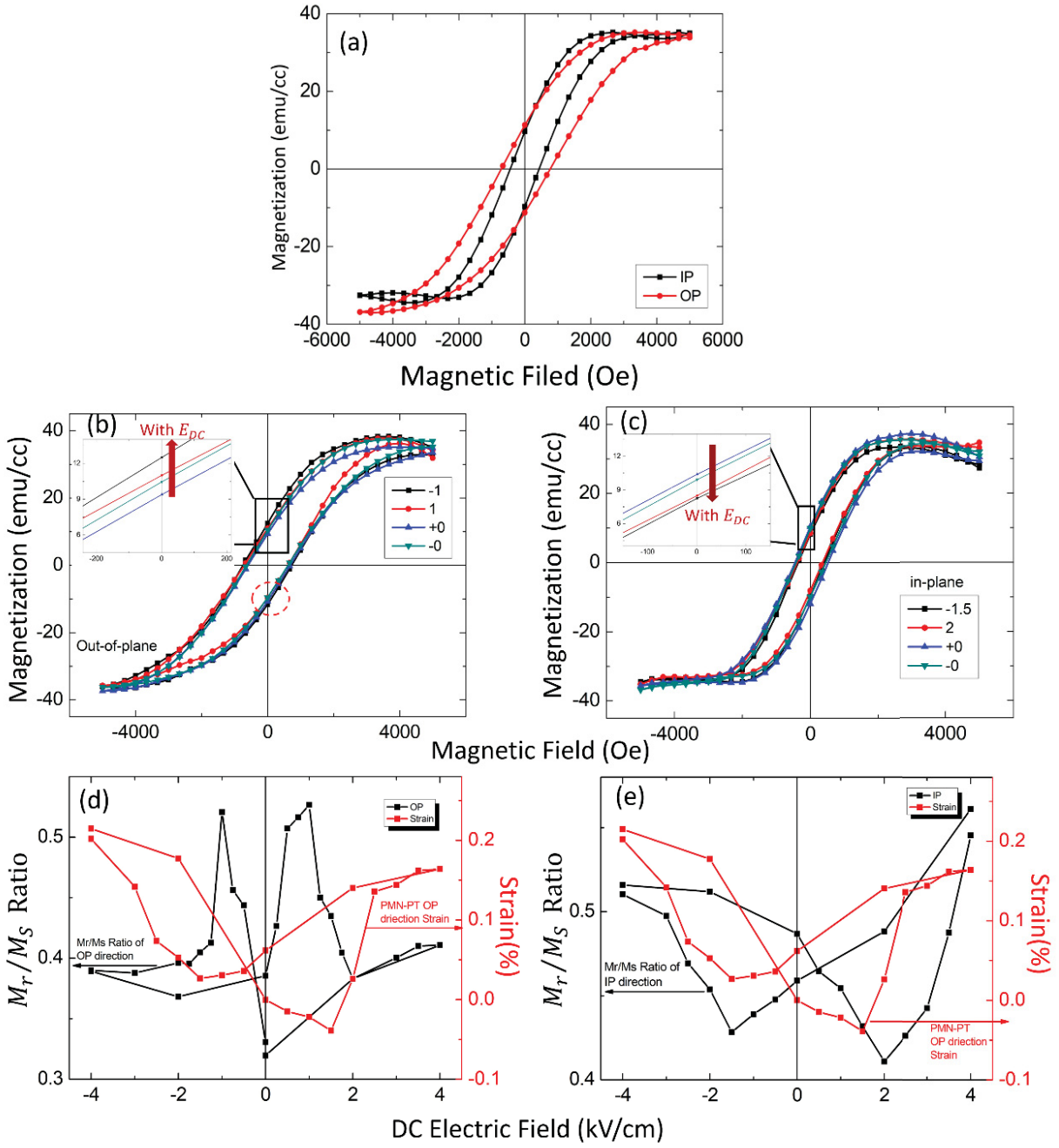

Figure 4.41. Magnetoelectric properties for both the IP and OP direction of BFO-CuFO/SRO/PMN-33PT. (a) M-H loop of both IP and OP. (b) M-H loop of OP direction under $\pm 1kV/cm$ *and* $0kV/cm$ E_{DC}*. The insert figure shows the IP and OP M-H loop together at 0 Oe. (c) M-H loop of IP direction under* $2kV/cm$*,* $-1.5kV/cm$ *and* $0kV/cm$ E_{DC}*. (d) and (e):* M_r/M_s *ratio sweep from* $-4kV/cm$ *to* $4kV/cm$ *of OP and IP directions, respectively.*

Figures 4.41 (b) and (c) show M-H loops under various applied E_{DC}, taken along OP and IP, respectively. The inserts in the figures show that M_r along the OP direction increased under $E_{DC} = \pm 1 kV/cm$; in contrast, M_r along the IP direction decreased under $E_{DC} = \pm 2\, kV/cm$. The specific values of E_{DC} provided in the inserts were chosen because they exhibited the largest magnetization changes. Similar to previously described BFO-CFO/PMN-PT heterostructures[10,66], the assumption here is that the magnetization changes were principally introduced by the anisotropy of the λ_{CuFO} and the piezoelectric coefficient of PMN-30PT. The heterostructure has an E-field-manipulated strain that occurs via the domain reorientation in the PMN-PT substrate, which means that the piezoelectric response and magnetic effect of BFO could be negligible[10,60,118]. This assumption significantly simplifies the analysis. According to Arai et al.[98], CuFO single crystals have a negative magnetostrictive coefficient ($\lambda_{CuFO} \sim -100 \times 10^{-6} m/A$), which is a modestly large λ when compared to CFO ($\lambda_{CFO} \sim -250 \times 10^{-6}$)[127]. The magnetostriction associated with CuFO imparts to CuFO/BFO/SRO/PMN-33PT heterostructures noteworthy magnetization changes under E_{DC} applied to PMN-PT. As shown in the right hand axis of Fig. 4.41 (d), the PMN-33PT substrate is placed under compressive strain along the OP direction by E, which subsequently induces the BFO-CuFO film to develop tensile strain along the IP direction. Rotation of the easy axis by compression along OP will cause M_r to be increased; in opposition, tension will cause M_r to decrease along the IP direction.

A remnant-to-saturation (M_r/M_s) magnetization ratio was then determined under various E_{DC} between $\pm$4kV/cm applied to the PMN-PT substrate. As can be seen on the left hand axis of Fig. 4.41 (d), the M_r/M_s ratio exhibited a butterfly-like shape, which is typical of a hysteresis loop of ferroic materials. The highest values were $M_r/M_s = 0.521$ under $E_{DC} = -1\, kV/cm$ and $M_r/M_s = 0.526$ under $E_{DC} = 1\, kV/cm$. The right hand axis of Fig. 5 (d) shows the corresponding

$\varepsilon - E$ curve for the PMN-33PT substrate. The $\varepsilon - E$ curve also exhibited a typical butterfly-like loop, where the highest compressive strain along OP was found under $E_{DC} = \pm 1.5\, kV/cm$, corresponding to the highest value of the M_r/M_s ratio on the left hand axis. Under higher E_{DC}, the M_r/M_s ratio became relatively constant with further increase of E_{DC}, reflecting saturation in the $\varepsilon - E$ curve. Please note that there was a large difference in the value of M_r/M_s under $E_{DC} = 0$ after positive and negative poling studies. This may be due to a combination of the remnant strain of PMN-PT (right hand axis) and pinning of the magnetic domain rotation in the CuFO nanopillars. Fig. 4.41 (e) shows similar M_r/M_s ratio data taken along the IP direction. Conversely, the values of M_r/M_s were decreased by compressive strain induced by applying E_{DC} to the PMN-PT substrate. The maximum decrease in M_r/M_s was found under E_{DC} of $-1.5\, kV/cm$ and $2\, kV/cm$.

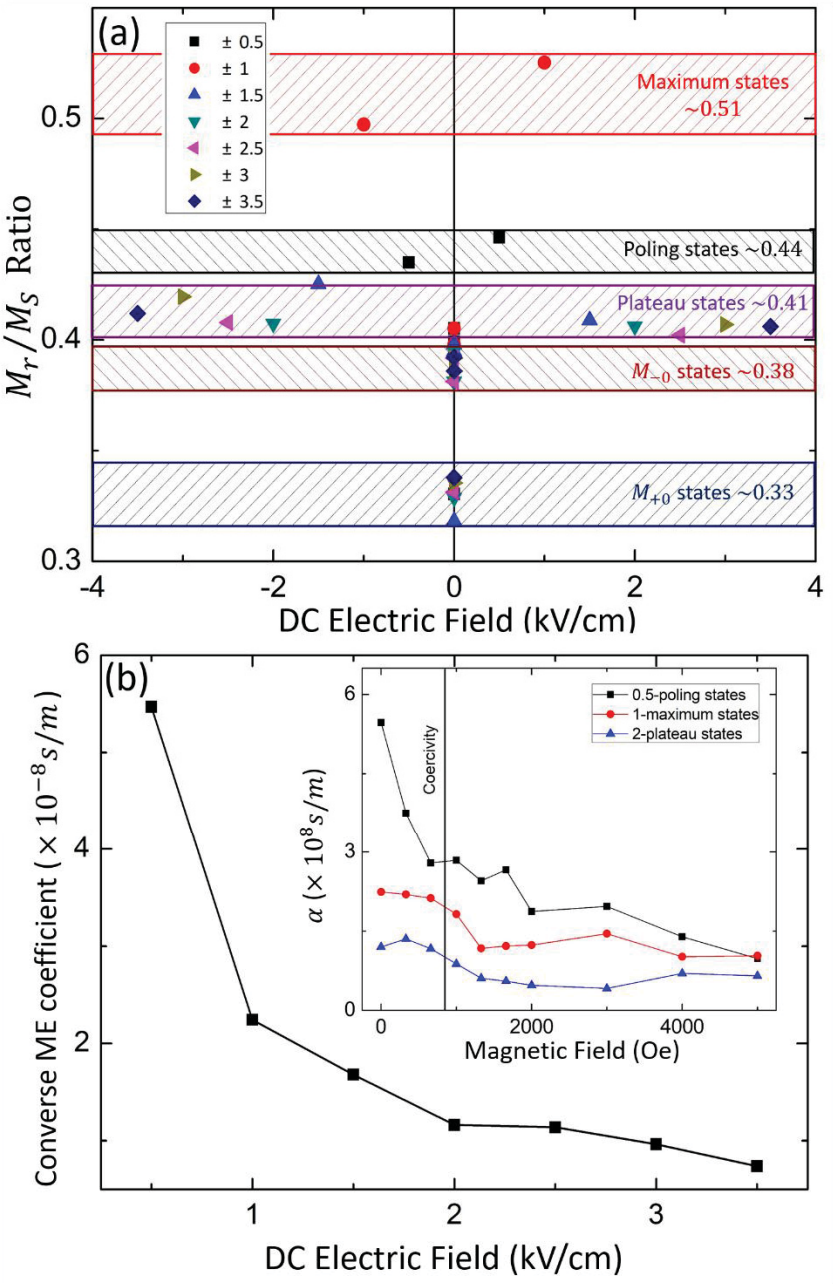

Figure 4.42. (a): Different magnetization states under varies E_{DC}. Different color bar showed 5 distinguishable magnetization states: maximum states, poling states, plateau states, M_{+0} and M_{-0} states. (b) α_{ME} under different E_{DC}. Insert at up right corner shows the α_{ME} of three representative magnetic states under different H_{DC}.

We then examined the E-field tunability of the magnetization states of the CuFO nanorods. Since their easy axis was along the out-of-plane direction, our measurements focused here on E-fields applied along that OP. Heterostructures were poled by different E_{DC}, and the M_r values recorded. Figure 4.42(a) clearly shows several different magnetic states. Under $E_{DC} = \pm 0.5 kV/cm$, the M_r/M_s ratio increased to ~0.44. This region is labeled in the figure as 'poling states'. Under E_{DC}=$\pm 1 kV/cm$, M_r/M_s reached a maximum values of 0.51. With further increases of E_{DC}, M_r/M_s fell back to ~0.41, which is designated as 'plateau states' in the figure. The values of M_r/M_s all corresponded to those in the left hand axis of Fig. 4.41(c). Upon removal of E_{DC}, two different values of M_r were found after positive and negative polings, which are labeled as M_{+0} and M_{-0}. The M_r/M_s values at M_{+0} and M_{-0} were found to be ~ 0.33 and ~ 0.38, respectively. These two values were similar to those for M_r/M_s under $E_{DC} = 0$ of the left hand axis of Fig. 4.41(c). The difference of M_r/M_s between M_{+0} and M_{-0} was ~0.05, which is smaller than that recently reported for BFO-CFO (~0.15)[10]. This difference is reasonable considering λ_{CuFO} is only ~1/3 of that for λ_{CFO}.

The E-field dependence of the magnetization demonstrates the presence of ME coupling in the CuFO-BFO/PMN-33PT heterostructures. To quantify this coupling, the converse ME coefficient (α) under different conditions was calculated by $\alpha = \mu_0 \times \Delta M/\Delta E$, as given in Fig. 4.42 (b); where μ_0 is the permeability of free space, ΔM is the magnetization change induce by DC electric field ΔE. The value of α was determined to be $\sim 5.5 \times 10^{-8}$s/m under $E_{DC} = 0.5 kV/cm$, which decreased to $\sim 1 \times 10^{-8}$ with increasing E_{DC}. The insert in the upper right corner in Fig. 4.42 (b) shows α for the three representative magnetic states (poling, maximum, and plateau) under different H-fields. As shown in the insert, α dramatically decreased for $H > H_C$, due to a high degree of magnetic-domain alignment. Compared to previous reported values for

vertically integrated BFO-CFO and STO and/or PMN-PT of $\alpha_{BFO-CuFO/STO} = 1 \times 10^{-10}\mathrm{s/m}$[118] and $\alpha_{BFO-CFO/PMN-PT} = 1.4 \times 10^{-7}\mathrm{s/m}$[10], the value for $\alpha_{BFO-CuFO/PMN-PT}$ can be seen to be significant. This result demonstrates good ME coupling between the CuFO nanopillars and PMN-PT substrate. These results are in distinct contrast to our findings for CuFO/SRO/PMN-33PT heterostructures.

4.8. Summary

In summary, self-assembled nanostructures of BFO-CuFO two-phase layers were deposited on SRO-buffered PMN-33PT (100) substrates utilizing SPLD. These self-assembled (1-3) heterostructures showed significant ME coefficient (α) values; in contrast, the single-layer CuFO ones had $\alpha \approx 0$. Accordingly, we can infer that the self-assembled nanostructure displayed significantly larger magnetostriction. The tetragonal lattice parameters were reasonably similar for the two types of layers as determined by XRD and SADP. The nanostructure of the self-assembled layer was unique, having a dense nanopillar/nanobelt mixed morphology as observed by AFM/MFM and TEM. The morphology was somewhat periodic. The mixed nanostructure undoubtedly formed to relax the elastic strain energy that emerged from the significant lattice mismatches between CuFO, BFO, and PMN-PT. Evidence of further relaxation was found by an extension of the top half nanostructure from the phase of the BFO matrix, as well as by the presence of a high density of nano twin walls in the CuFO phase. The saturation and remnant magnetizations were about equal, after accounting for the CuFO:BFO ratio of self-assembled layer. The CuFO/SRO/PMN-3PT heterostructure exhibited no evidence of magnetoelectric coupling; however, for the self-assembled heterostructures, magnetization changes under applied E_{DC} were found along the easy magnetization axis, where the M_r/M_s ratio exhibited a butterfly loop with

E_{DC}. Two remnant states (M_{+0} and M_{-0}) were found upon removal of E_{DC}. The converse magnetoelectric coefficient was calculated under different conditions, and the maximum was found to be $\alpha_{ME} = 5.5 \times 10^{-8}$s/m.

Clearly, nanostructure geometry plays a key role in the ME coupling of vertically-integrated CuFO-BFO layers—and by association the enhanced magnetostriction of these layers. However, this effect comes at a cost, as the hysteretic losses were increased relative to the corresponding CuFO single layer. These findings demonstrate a unique tradeoff of λ_m and Q that can be achieved by nanostructure design, offering an intriguing approach for improving ME coupling.

CHAPTER 5: NON-VOLATILITY USING MATERIALS WITH ONLY VOLATILE PROPERTIES: VERITCALLY INTEGRATED NANOPILLAR HETEROSTRUCTURE AND THEIR POTENTIAL FOR MULTI-LEVEL-CELL DEVICES

5.1. Overview of Pinned Rotation of by (1-3) Heterostructures

Most potential materials for use in magnetoelectric random access memory devices, such as Metglass[7,137] are potentially volatile and thus fail a critical requirement for use in such memory devices. To determine a solution for this deficiency, vertically-integrated nanopillars (designated as 1-3) heterostructures have previously been investigated, which combine magnetostrictive and piezoelectric phases with a dramatically higher ME couplings[39,58,60,61]. Previously, (1-3) nanopillar heterostructures of $BiFeO_3$-$CoFe_2O_4$ (BFO-CFO) or $BiFeO_3$-$CuFe_2O_4$ (BFO-CuFO) deposited on $Pb(Mg_{1/3}Nb_{2/3})_{1-x}Ti_xO_3$ (PMN-xPT) single-crystal substrates have been shown to have giant ME effects[10,65].

The PMN-xPT substrates described in these prior studies displayed a large piezoelectric response, where strain was transferred to deposited films. This approach shows promise for use in various tunable multifunctional applications[10]. However, the composition of PMN-xPT crystals can often suffer from problems with spatial uniformity. The strain-induced properties of PMN-xPT can be non-volatile ($x > 35\%$) or volatile ($x < 31\%$)[78]. In the vicinity of the morphotropic phase boundary or MPB ($x \approx 32\%$), a maximum piezoelectric response is associated with induced phase changes; however, the degree of volatile/non-volatile features can vary across a sample or between crystals of similar composition due to the various mixed phases[63]. This non-uniformity is due in part to the crystal growth process[138], and to the mixed B-site cation site. This non-uniformity results in unwanted variability in multifunctional layers deposited on PMNxPT, especially for non-volatility for memory or logic applications.

Previously, nanopillar structures of BFO-CFO vertically integrated layers have been shown to pin the rotation of magnetic domains[45]. This pinning enables the possibility for N>2 remnant magnetization states. In fact, there have been reports of N≥ 4 different magnetic states in BFO-CFO/PMN-PT upon removal of E[10,39,62,63]. This pinned domain rotation can result in non-volatile magnetization in CFO nanopillars. When the composition of PT in PMN-PT crystal locates near the MPB, the volatile properties become unpredictable. For example, single CFO layers deposited on PMN-30PT have been shown to display volatile magnetization changes[63], whereas Mn-doped CFO deposited on PMN-30PT exhibits non-volatile magnetization changes[64]. The unpredictability of these induced property changes hinders their potential for applications. Previously reported BFO-CuFO on PMN-33PT[65] and BFO-CFO on PMN-30PT[66] demonstrated non-volatile changes. Both PMN-33PT and PMN-30PT are close to the MPB, and thus these results indicate such (1-3) heterostructures might exhibit non-volatility, even though they consist of phases that individually are volatile.

Here, we report a self-assembling, two-phase, vertically integrated (1-3) heterostructure as illustrated in Figure 5.43 (a). Vertically integrated two-phase BFO-CFO and BFO-CuFO layers were epitaxially deposited on $SrRuO_3$-buffered (100) oriented $Pb(Mg_{1/3}Nb_{2/3})_{0.74}Ti_{0.26}O_3$ (SRO/PMN-26PT). These PMN-26PT substrates were found to possess relatively large but volatile strain changes with E_{DC}. Our results demonstrate that (1-3) heterostructures can hinder the rotation of magnetic domains, resulting in non-volatile E-field-induced magnetization changes, even on a piezoelectric substrate whose properties are clearly volatile. This characteristic enhances the likelihood that the heterostructures can be used in MLC memory devices.

5.2. Experiment Method

BFO-CFO thin films were epitaxially deposited on SRO-buffered (100) oriented PMN-26PT substrates by pulsed laser deposition (PLD). The BFO-CuFO thin films were deposited by switched PLD (SPLD)[65,106], which is a useful method for depositing vertically integrated ME heterostructures. The thickness of all films was 130nm. The targets were switched 10 times, creating a total thickness of 130nm. The thin films had electrodes attached to them, as illustrated in Fig. 5.43 (a).

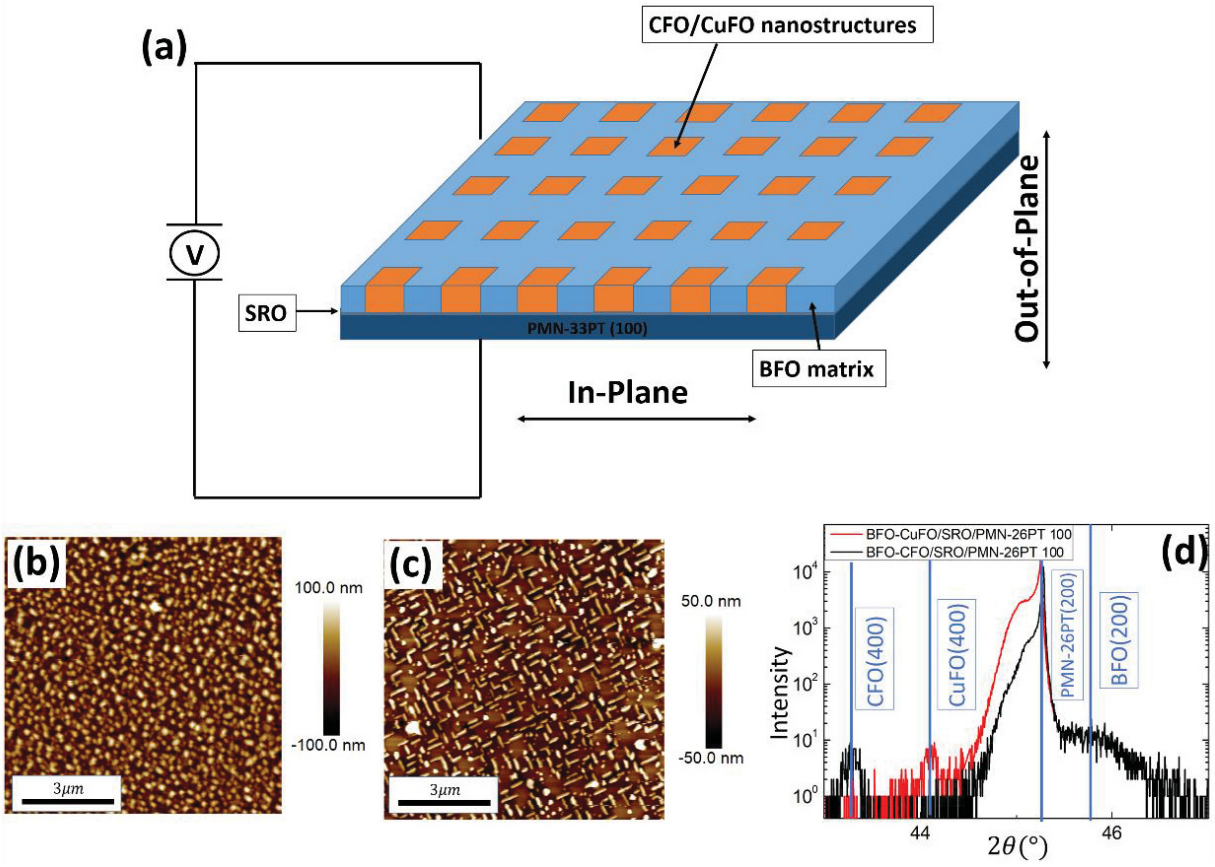

Figure 5.43. (a) Demonstration of (1-3) heterostructure of BFO-CFO(CuFO)/SRO/PMN-26PT, and direction of applied DC E-field. AFM images morphology of (b) BFO-CFO/SRO/PMN-26PT and (c) BFO-CuFO/SRO/PMN-26PT. (d) XRD line scan of both (1-3) heterostructures.

5.3. Non-volatility Established by (1-3) Heterostructures with individually volatile materials

Figures 5.43 (b) and (c) illustrate the morphology of both BFO-CFO and BFO-CuFO (1-3) heterostructures on PMN-26PT substrates. The BFO-CFO layer displayed a typical square-like nanopillar morphology, as previously shown[71]. BFO-CuFO exhibited a mixed nanopillar and nanobelt structure, as previous described in the literature[65]. Figure 5.43 (d) shows an XRD line scan for both heterostructures, revealing good epitaxial growth of both matrix (BFO) and nanostructure (CFO and CuFO) phases on the substrates.

A DC electric field (E_{DC}) was applied on the sample along the out-of-plane (OP) direction, as shown in Fig. 5.43 (a). Figure 5.44 shows how the ratio of the remnant (M_r)-to-saturation magnetizations (M_r/M_s) changed with applied E_{DC}. The value of M_r at E=0 was measured after E_{DC} was removed for $-6\text{kV/cm} \leq E_{DC} \leq 6\text{kV/cm}$. Figure 5.44 (a) provides data for BFO-CFO/SRO/PMN-26PT. As can be seen, the M_r/M_s ratio increased to about 0.58 after the application of $E_{DC} = \pm 1.5\text{kV/cm}$, and then gradually decreased to about 0.4 after removal of increasingly higher E_{DC}. These trends are similar to those recently reported for BFO-CFO heterostructures[10]. The values of M_r/M_s can be categorized into three stages: poling/de-poling (≈ 0.5), maximum (≈ 0.57), and plateau (≈ 0.41). After removal of E_{DC}, the M_r/M_s ratios were different, depending upon whether the E had previously been positive (M_{+0}~0.32) or negative (M_{-0}~0.39). Figure 2(b) shows $\frac{M_r}{M_s}\ vs.\ E_{DC}$ for heterostructures of BFO-CuFO/SRO/PMN-26PT. Similar results can be seen to those for BFO-CFO. The BFO-CuFO heterostructures exhibited multiple stages: poling/de-poling (≈ 0.44), maximum (≈ 0.51), plateau (≈ 0.41), M_{+0}~0.33 and M_{-0}~0.38. These results clearly confirm the non-volatile magnetization changes with individually volatile materials, which would meet the requirements for use in advanced industrial applications.

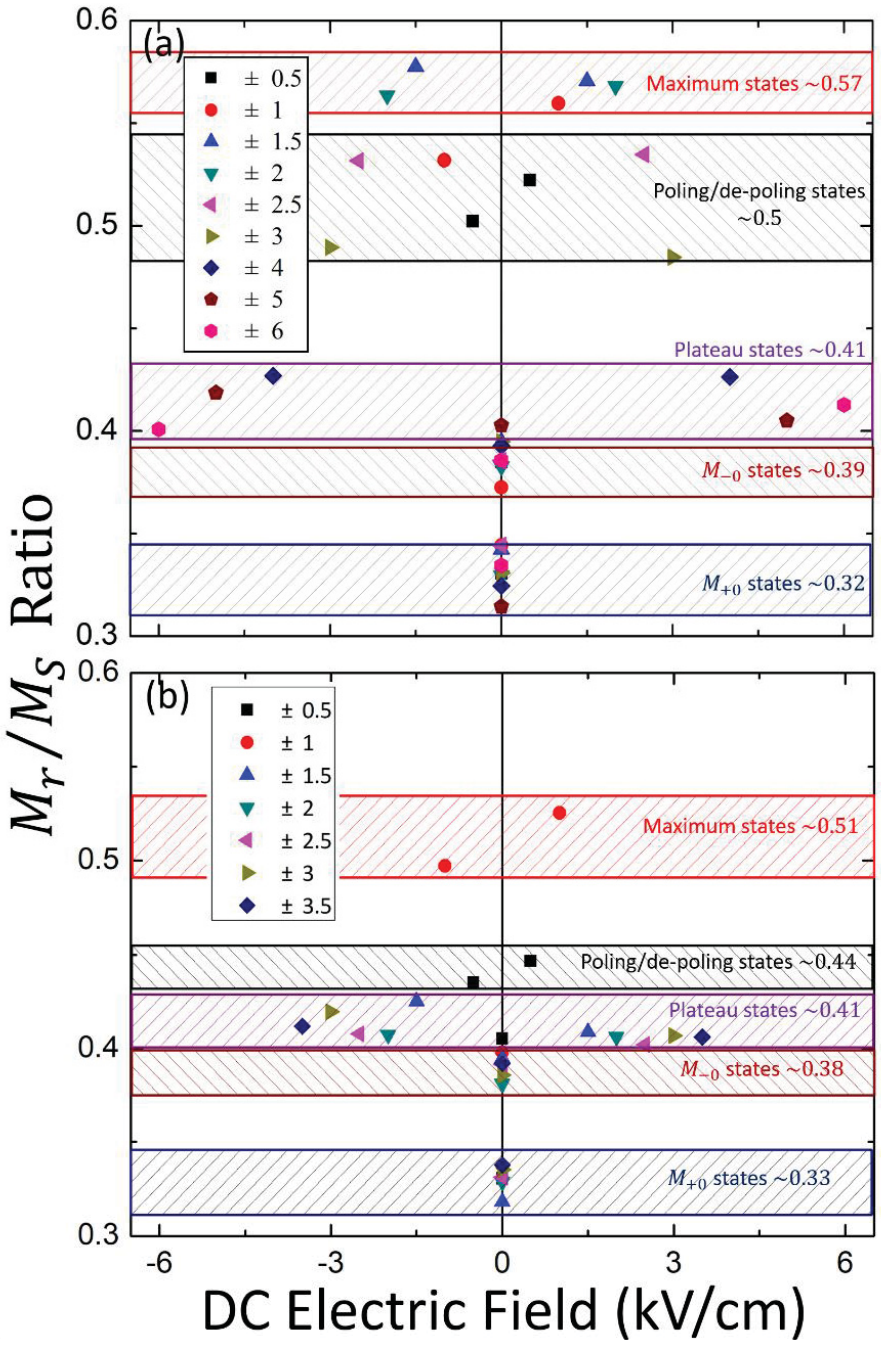

Figure 5.44. Schematic of magnetization outcomes using binary input: E-field and H-field. (a): Input E-field strength. (b) Input H-field strength. (c): Magnetization outcome of both BFO-CFO and BFO-CuFO heterostructure. Insert figure of (c) A schematic illustration of potential memory device application based on (1-3) heterostructure.

5.4. Achievable Magnetic States.

It is interesting to note that M_r/M_s was dependent on the polarity of the field that had previously been applied. Even though the E-induced strain of the PMN-26PT substrate was previously reported as being volatile[78], the value of M_r/M_s of our two-phase magnetic thin film was non-volatile. To date, such non-volatility has not been reported for heterostructures made solely of volatile materials. In fact, the piezoelectric response of PMN-30PT substrates has a volatile feature[78], as do the single-phase CFO layers deposited in their surface[64]. The (1-3) nanostructure hinders the rotation of the magnetic domains, creating unique multiple states upon removal of E_{DC}[10]. This approach may be able to circumvent the issue of variability in the non-volatility of the PMN-xPT substrate imparted to deposited layers. One, then, has the option to use a wide range of PMN-xPT compositions on the left of the MPB, which themselves have only volatile changes.

Table 5.6. Accessible input/output states for BFO-CuFO/SRO/PMN-26PT.

No.	**Input A (E-field)**		**Input B (H-field)**		**Output M**	
	kV/cm	Represent symbols	Oe	Represent symbols	M_r/M_s	Represent symbols
1	1	1	5000	1	0.3	11
2	-1	0	-5000	0	-0.4	00
3	1	1	-5000	0	-0.3	10
4	-1	0	5000	1	0.4	10

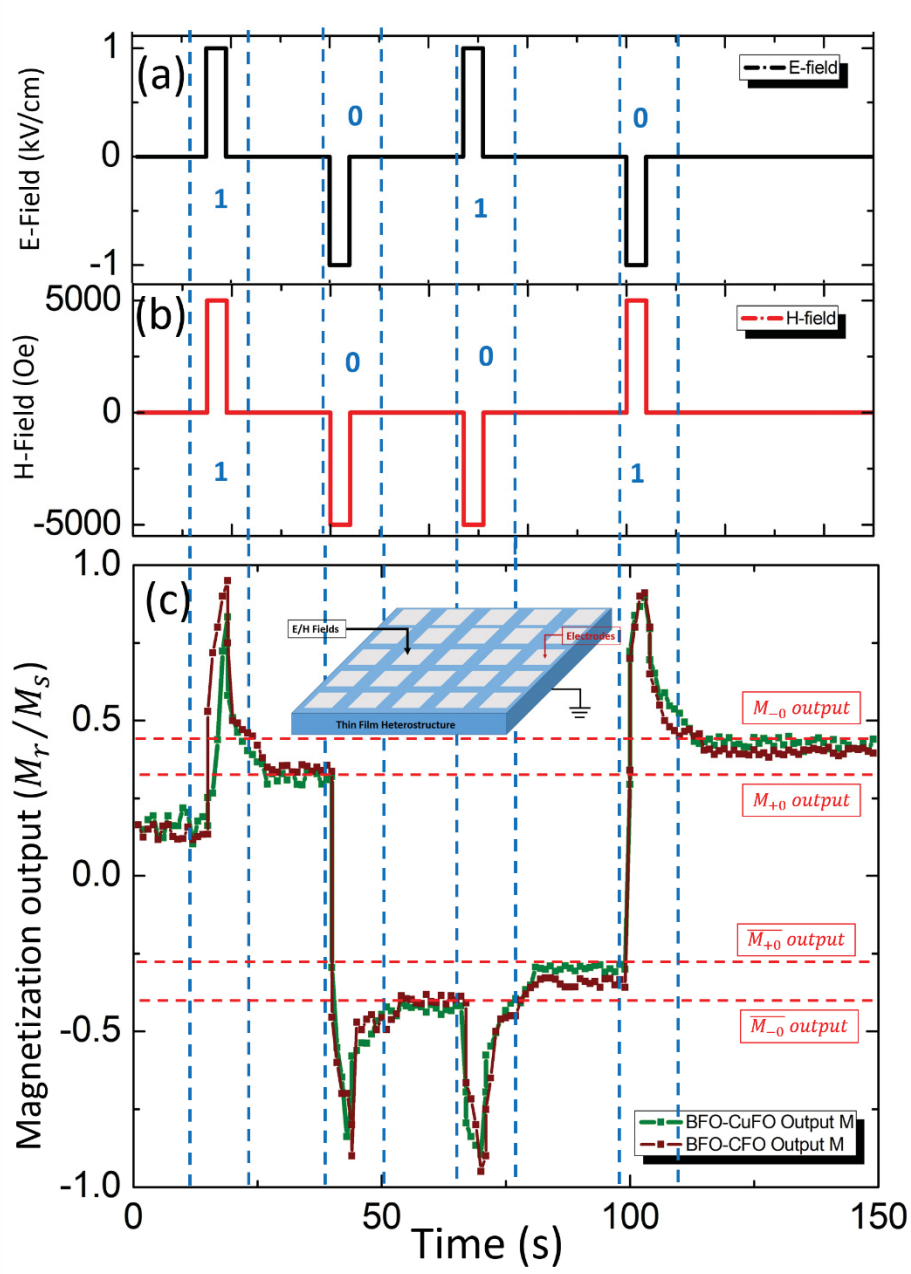

Figure 5.45. (a): Different magnetization states under varies E_{DC} of BFO-CFO/SRO/PMN-26PT heterostructure. Different color bar showed 5 distinguishable magnetization states: maximum states, poling states, plateau states, M_{+0} and M_{-0} states. (b) Different magnetization states under varies E_{DC} of BFO-CuFO/SRO/PMN-26PT heterostructure with similar multiple states.

The value of M_r/M_s depends on both E_{DC} and magnetic field (H). If the sign of E_{DC} is reversed, two remnant magnetic states are addressable for BFO-CFO/PMN-30PT (M_{+0}~0.32 and M_{-0}~0.39) and BFO-CuFO/PMN-26PT (M_{+0}~0.33 and M_{-0}~0.38). If the H-field was reversed, an additional two remnant magnetic states would become accessible. Figure 7.45 summarizes how this four-state memory was achieved. As can be seen in Parts (a) and (b), E_{DC} and H were both used as inputs. Input fields of $E_{DC} = \pm 1\text{kV/cm}$ (maximum M_r/M_s) and $\text{H} = \pm 5000$ Oe (saturation magnetization) were used. Four different dual-field input conditions are illustrated in Figures 7.45 (a) and (b). Using '1' to represent E_{DC} =1kV/cm and H=5000 Oe, and '0' for E_{DC} =–1kV/cm and H=-5000 Oe, there was a combination of four different input situations that we can designate as 11, 00, 10, 01. These four input combinations resulted in the corresponding magnetization outputs for both BFO-CFO and BFO-CuFO heterostructures, as shown in Fig. 7.45 (c). This clearly demonstrates four distinguishable remnant magnetization states: '11' input with $M_{+0} \approx 0.3$ output; '00' input with $\overline{M_{-0}} \approx -0.4$ output; '10' input with $\overline{M_{+0}} \approx -0.3$ output; and '01' input with $M_{-0} \approx 0.4$ output. Table 7.6 summarizes these different inputs and outputs.

5.5. Possible Applications: Multi-Level-Cell.

Traditional memory devices usually have only two remnant states, which are interoperated as '1' and '0'. However, these two-state memory devices suffer from deficiencies such as accumulated reading error, inability to corroborate with advanced algorithms, and low storage densities[139,140]. Recently, a new technique called Multi-Level-Cell (MLC) memory was proposed[100,140], which can store more than one bit of information inside a single cell, resulting in much higher storage density, and much lower cost-per-bit[101]. This MLC storage approach challenges conventional binary memory materials because it requires more than two states in one

unit to store information[101]. If the sample surface is segregated into different cells and coated with conductive electrodes layers, as illustrated in the insert of Fig. 3 (c), a multi-bit-per-cell memory device could be built, resulting in reduced reading errors and much higher storage densities. By introducing binary input H-field and E-field signals, multiple magnetic states ($N \geq 2$) could be accessed. In Figure 3(c) one can see that the outcomes for BFO-CFO and BFO-CuFO heterostructures were similar to each other. This similarity shows that the geometry of (1-3) heterostructures plays a determining role. Even though the substrate and magnetic materials (CFO or CuFO) are volatile, the shape anisotropy created by the BFO matrix forced the magnetic domains to remain along the poling direction, establishing stable magnetic states.

To date, different types of MLC devices using the ME coupling effect have been reported[141,142]. However, they have been limited either by the non-uniformity of the PMN-xPT substrates for compositions near the MPB[141], or by the use of traditional non-volatile materials[142]. However, the work presented herein allows one to choose a wide range of compositions of the PMN-PT MPB, and also for repeatable multi-magnetic memory states achieved when E is applied to the substrate.

5.6. Summary

In this work, BFO-CFO and BFO-CuFO (1-3) heterostructures were deposited on PMN-26PT substrates, and multiple magnetic states were found. Upon removal of E_{DC}, two remnant magnetization states were found to be stable. Applying an additional H-field input, two more different remnant magnetization states were found accessible and stable upon removal H and E. Our investigations confirmed the successful development of (1-3) heterostructures with non-volatility, even though the materials phases/substrates retained their volatile properties. This

expands the potential for enhancing the uniformity and repeatability of multifunctional layers deposited on PMN-PT crystal substrates. Additionally, this investigation confirmed the likelihood of a much wider compositional range for choice of the PMN-xPT substrates for magnetic multi-states memory devices. For $N \geq 4$ magnetic states, an MLC memory device could be easily built with high ME coupling and multiple magnetic states.

CHAPTER 6: SELF-ASSEMBLED EPITAXIAL BFO-NZAFO NANOBELT HETEROSTRUCTURES ON STO: CONTROL OF MAGENTIC ANISOTROPY, EASY AXIS AND COERCIVITY

6.1. Overview of BFO-NZAFO/STO Nanobelt Heterostructure.

The magnetic properties of materials with giant magnetostriction are largely dependent on their magnetic anisotropy[39]. To date, many applications have relied on the manipulation of the anisotropy in order to optimize properties[143-146]. Such approaches include moving the easy axis from the in-plane (IP) to the out-of-plane (OP) direction for electric reading[23], and forming 2D/3D arrays of easy axes for reconfigurable electronics[10,11,39]. Among the various contributions to magnetic anisotropy, shape anisotropy is the easiest one to access for manipulation[7,39]. A method that has been used to control the shape anisotropy of epitaxial layers is by employing self-assembling nanostructures of two phases[69,70], such as $BiFeO_3$-$CoFe_2O_4$ (BFO-CFO) that forms vertically integrated nanopillar structures on (100) $SrTiO_3$ (STO)-oriented substrates[10,147], and nanobelt structures on (110) substrates[72]. Recently, we have reported a self-assembled mixed nanopillar/nanobelt heterostructure layer of BFO-$CuFe_2O_4$ (BFO-CuFO)[65]. The magnetic anisotropy of the CuFO phase was altered by the mixed nanostructure, which enhanced the magnetoelectric (ME) effect.

Recently, Emori et al[99]. reported novel $Ni_{0.65}Zn_{0.35}Al_{0.8}Fe_{1.2}O_4$ (NZAFO) spinel layers that displayed large magnetostriction and small losses. Compared with conventional magnetic ferrites (such as CFO), the coercive filed (H_c) of NZAFO was notably smaller, imparting improved quality factors (Q)[89,91] and efficiencies[90,92]. The coercivity of NZAFO layers was small ($\sim$2 Oe), limiting its potential for applications requiring remanence. NZAFO, CFO, and CuFO are all spinel ferrites with similar lattice parameters and structures. Thus, it should be feasible to deposit self-assembling

two-phase BFO-NZAFO layers, thus augmenting the potential for tuning their magnetic anisotropies and coercivities. Switched pulsed laser deposition (SPLD) is a technique that uses alternating targets during deposition, creating self-assembled heterostructures[56,106]. Here, we report a BFO-NZAFO nanobelt composite epitaxially deposited on (110) STO. Following an investigation of their magnetic anisotropy characteristics, we were able to manipulate H_c via nanostructural control.

6.2. Experiment Method

$BiFeO_3$ (from Kurt Lesker)-NZAFO (from Toshima Manufacturing Co., Ltd.) two-phase layers were epitaxially deposited by SPLD on (110) STO (from Crystech). Prior to deposition, the substrates were cleaned with acetone and alcohol via ultrasonication. Self-assembled BFO-NZAFO layers were deposited at a volume fraction of about 60:40. First, a BFO single layer was deposited at 650℃ using an energy density of 1.2 J/cm^2 and an O_2 atmosphere of 150 mTorr for 2 min 45s. The target was then switched to NZAFO. Deposition was done for 2min 15s at 650℃, 1.2 J/cm^2 and 150 mTorr to form a bilayer structure. This procedure was repeated 10 times, resulting in a layer with a total thickness of about 100nm. The samples were then annealed at 700℃ and 100 Torr O_2. AFM images were obtained (Dimension 3100, Vecco). Cross-sectional images, selected area electron diffraction patterns (SADP), and energy dispersive x-ray spectra (EDS) were obtained using transmission electron microscopy (JEOL 2100). The crystal structures were determined by X-ray diffraction (Philips X'Pert system) and SADP. Magnetic hysteresis curves were recorded using a vibrating sample magnetometer (Microsense, EZ-9).

6.3. Morphology & Composition of the BFO-NZAFO/STO Nanobelt Heterostructure.

Figure 6.46 illustrates the surface topography of a BFO-NZAFO/STO (110) heterostructure. Part (a) shows the cross-sectional TEM image, revealing a nanobelt structure, and Part (b) shows the surface morphology of the nanobelt structure itself. One can see that the nanobelts are oriented along the $[1\bar{1}0]$ direction, similar to that previously reported for BFO-CFO on (110) STO[39]. This result indicates that the surface tension of NZAFO is similar to that of CFO, which favors $[1\bar{1}0]$ nanobelt formation[70]. The cross-sectional image reveals a clear edge line between the BFO and NZAFO, demonstrating that the nanobelt morphology extends throughout the entire thickness from the top surface of the film to the substrate. It should be noted that the NZAFO nanobelts consisted of a dense array of nanotwin walls at the interface to the BFO matrix, which have also been observed in BFO-CuFO heterostructures[65]. Parts (c)-(f) provides EDS mappings of Zn, Bi, Al, and Ti elements. The traces of Zn and Al displayed good overlap with each other, indicating the formation of NZAFO. The trace of Bi was found mostly in the matrix, demonstrating that it was well constrained to the BFO phase. Part (f) shows the trace of Ti, which revealed that it was constrained to the STO substrate. Overall, the EDS mapping confirmed that the nanobelts were the NZAFO phase, and that the matrix the BFO.

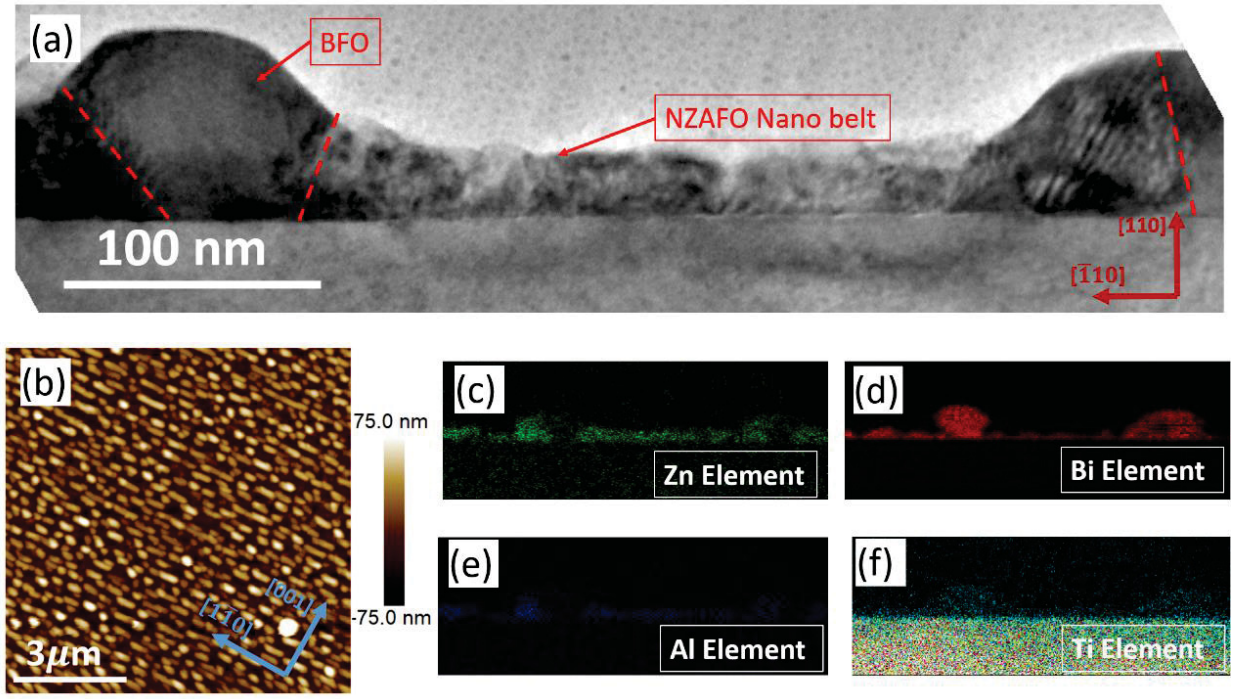

Figure 6.46 (a): Cross-sectional image of BFO-NZAFO heterostructure on (110)-oriented STO substrate. (b): AFM image of surface of BFO-NZAFO heterostructure. (c) - (f): EDS mapping of cross-sectional image, different figures show different elements.

6.4. Epitaxy of the BFO-NZAFO/STO Nanobelt Heterostructure.

Figure 6.47 shows a XRD line scan for BFO-NZAFO/STO. The data clearly demonstrate the epitaxial growth of NZAFO and BFO on (110) STO. The lattice parameters were calculated from the scan: BFO (110) had a peak at 31.49° and a lattice parameter of 4.00Å, and NZAFO (220) had a peak at 30.46° and a lattice parameter of 8.29Å. Along the OP direction, compared to bulk lattice parameters, the BFO phase had a tensile strain of about 1% ($a_{BFO-Bulk} = 3.96$Å[70]), and NZAFO had a compressive strain ($a_{NZAFO-Bulk} = 8.36$Å) of -1.2%. The insert in Fig. 6.47 shows a SADP

taken from the image in Fig. 6.46(a). The calculated lattice parameters from the insert were $a_{BFO-DP} = 4.01$Å and $a_{NZAFO-DP} = 8.30$Å, both consistent with that obtained by XRD.

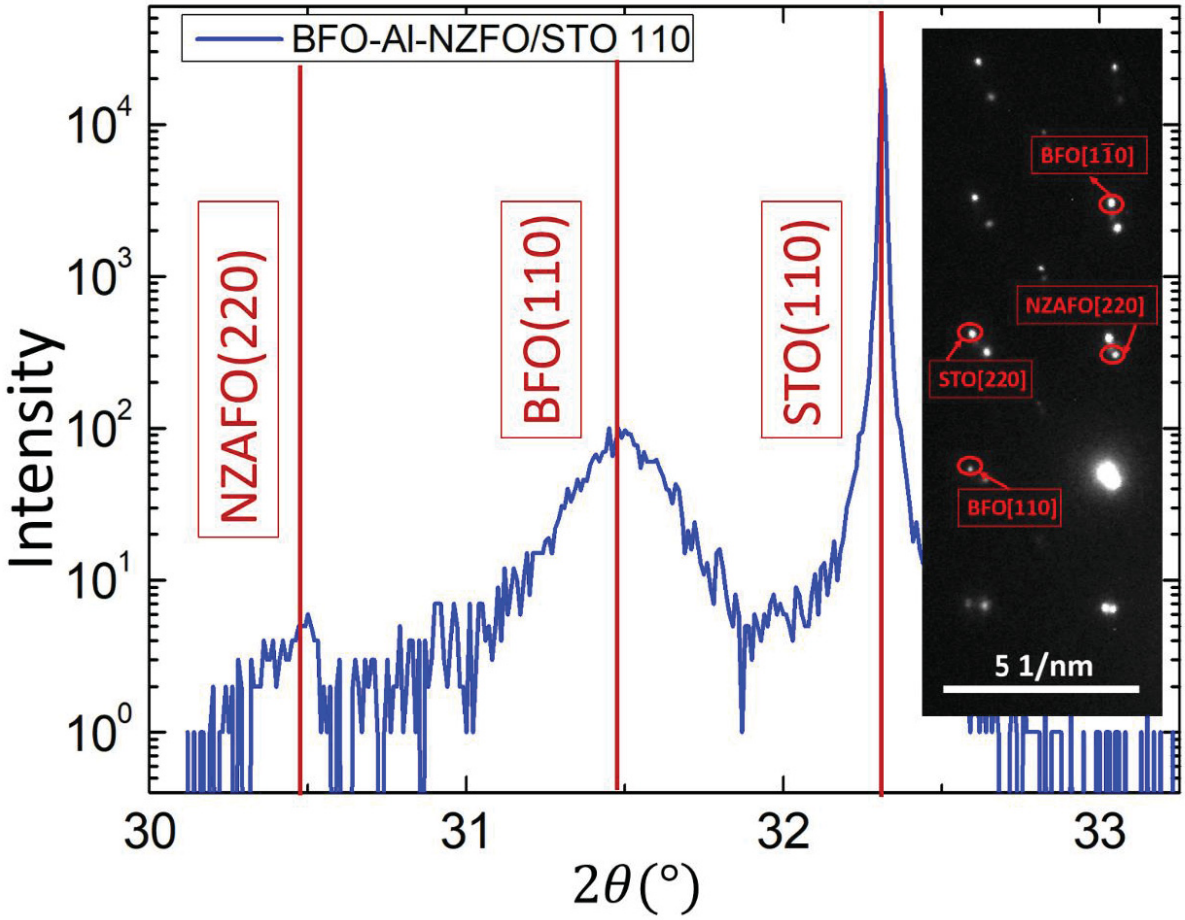

Figure 6.47. XRD line scan of the BFO-NZAFO/(110) STO. The insert figure shows diffraction pattern of cross-sectional area shown in Fig. 1(a).

6.5. Magnetic Anisotropy of the BFO-NZAFO/STO Nanobelt Heterostructure along IP/OP

Figure 6.48 (a) shows a magnetic hysteresis loop for a BFO-NZAFO heterostructure along both the in-plane (IP) and out-of-plane (OP) directions. From the figure, one can see that the easy axis lies along the IP direction. This was expected, as the magnetic shape anisotropy lies along the IP, due to the fact that the nanobelts are oriented along the $[1\bar{1}0]$ direction (see Fig. 6.46(b)). The insert in the lower right corner shows an enlarged figure for the remnant magnetization (M_r) and coercivity (H_c). One can see that $M_{r-IP} = 9emu/cc$ and $M_{r-OP} = 8emu/cc$, with coercivities of about $H_{c-IP} = 37\ Oe$ and $H_{c-OP} = 47\ Oe$. Because the atomic percentage of BFO:NZAFO was about 0.6:0.4, it can be inferred that a single phase NZAFO would have M_{r-IP} M_{r-OP} values of 23 and 20 emu/cc, respectively. This M_{r-OP} value is similar to that previous reported for NZAFO[99]. In contrast, the M_{r-IP} was much smaller, which may be attributed to the fact that the nanobelt-shape anisotropy results in the easy axis not lying along the [001] direction, which is the measurement orientation in Fig. 6.46(a). Also, the magnetic coercivity was ~45 Oe, which is notably larger than the recently reported value of 2 Oe[99] for epitaxial single phase NZAFO layers. The shape anisotropy energy density of a NZAFO cylinder should be given by $\varepsilon_{shape} = 2\pi(N_x - N_z){M_s}^2$, where $N_x = (1 - N_z)/2$[69] and N_z is a demagnetization factor related to the aspect ratio. From Figs. 6.46(a) and (b), the average aspect ratio can be determined to be 1.5. According to Beleggia et al.[148], the value of N_z~0.28 results when the aspect ratio is ~1.5. Considering that $H_{shape} = 2\varepsilon_{shape}/M_s$, the coercivity induced by the shape anisotropy (H_{shape}) can be determined to be $H_{shape-IP} = 50\ Oe$ and $H_{shape-OP} = 60\ Oe$ for the IP and OP directions, respectively. This value of $H_{shape-IP}$ is close to the measured data shown in Fig. 6.46(a), confirming that magnetic shape anisotropy contributes significantly to the coercive field. The results described herein

demonstrate an important method by which these small values of H_c for NZAFO epitaxial layers can be manipulated.

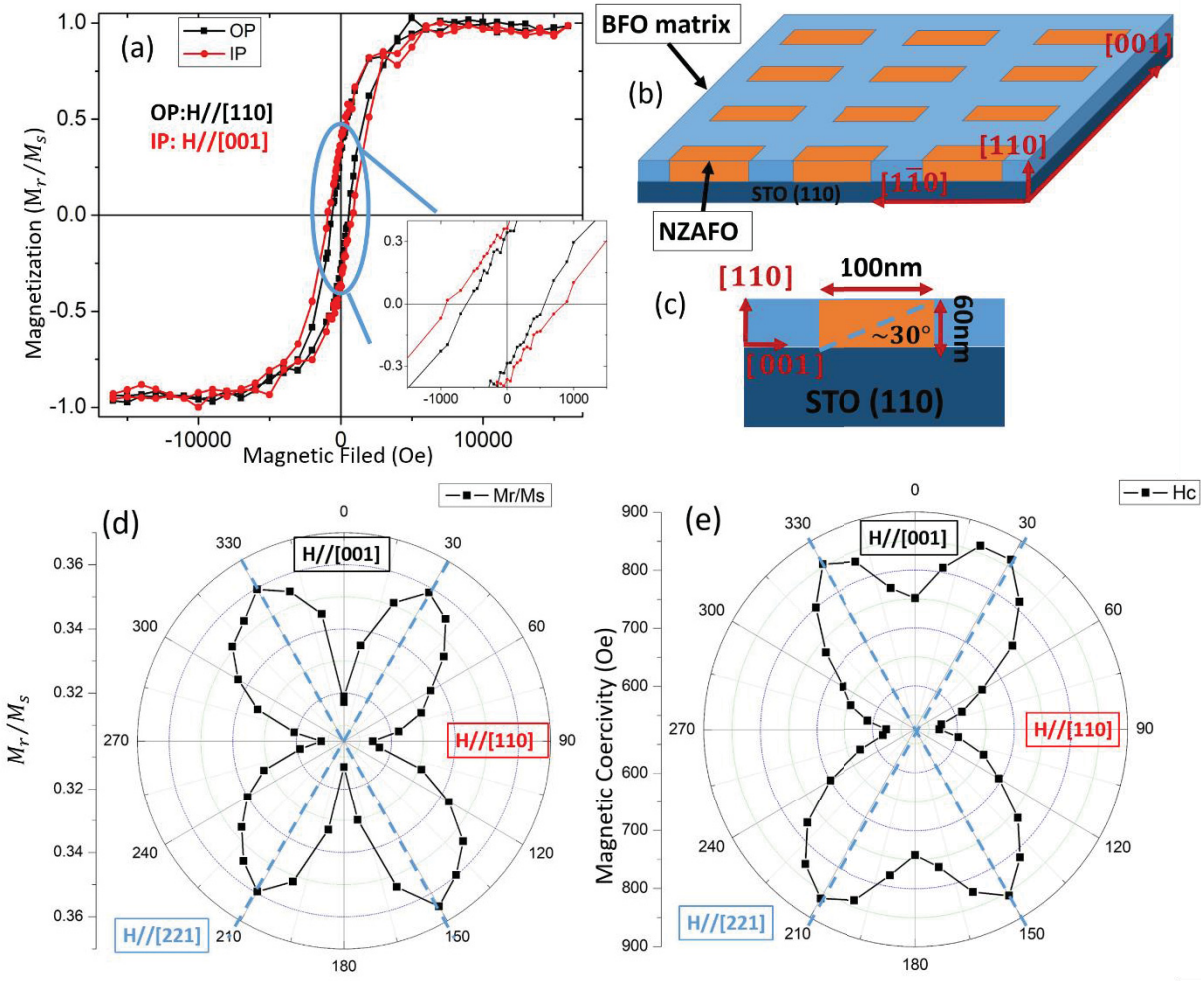

Figure 6.48. Magnetic hysteresis loop of BFO-NZAFO/(110) STO. (a) M-H loop of in-plane and out-of-plane direction. Insert figure of downright comer shows the enlarged area of coercivity and remnant magnetization. (b): Schematic figure of BFO-NZAFO nanobelt heterostructure with orientation labeled. (c): Schematic figure of BFO-NZAFO unit cutting along the [1$\bar{1}$0] direction. (c): M_r/M_s in response of angular, orientation of H filed was labeled. (d): Hc in response of angular, orientation of H filed was labeled.

Figures 6.48(d) and 6.48(e) show M_r and H_c as a function of rotation angle (θ) between the [001] and [110] directions. The magnetic easy and hard axes of the BFO-NZAFO/STO heterostructure can readily be identified in the figure. Smaller values of M_r and H_c can be seen along the [110] direction ($\theta = 90°$), which is the OP direction. This finding indicates that the hard axis lies along the [110] direction ($\theta = 90°$). Interestingly, the highest values were not found along the IP direction ([001], $\theta = 0°$), which is the traditional easy axis for the thin films. Rather, the highest values for M_r and H_c were located at $\theta = \pm 30°$, yielding two easy axes for the BFO-NZAFO heterostructures. These two orientations were the directions of the nanobelt length (see Figure 6.46(c)) with respect to the IP. According to Emori et al.[99], when under a compressive epitaxial strain, NZAFO single-phase layers have an easy axis along the face diagonal of the lattice. In the NZAFO nanobelts, the face diagonal is about 30° from the [001] direction (along the [221] direction), as can be determined by considering the length and height of the nanobelts in the heterostructure. Therefore, the values of M_r and H_c along the $\pm 30°$ from IP direction were the highest, and indicates that they are the easy axes.

As noted in the previous section, the difference of M_r is not significant between the IP and OP directions, as shown in Fig. 6.48 (a), due to the fact that the IP measurements were taken along the [001] direction. In the heterostructure, nanobelts form along the $[1\bar{1}0]$ direction, and the easy axis of the plane that is parallel to the IP direction should be oriented along the nanobelt, due to its dominant shape anisotropy contribution. Therefore, rotation about the IP (e.g., along [110]) was performed during VSM measurements, as shown in Figure 6.49. The results demonstrate that the IP magnetic anisotropy easy axis is along the $[1\bar{1}0]$ direction, which is the orientation of the nanobelts. This IP magnetic anisotropy displays easy axes along both the $[1\bar{1}0]$ and $[\bar{1}10]$ directions. As shown in Fig. 6.49, two points are circled by blue and red labels, which illustrate

when M-H loops were measured, as indicated in the insert in the lower right corner. The red and blue points designate the easy and hard axes, respectively. The M-H loops for these two points show a significant difference in both M_r and H_c, indicating a large induced magnetic shape anisotropy.

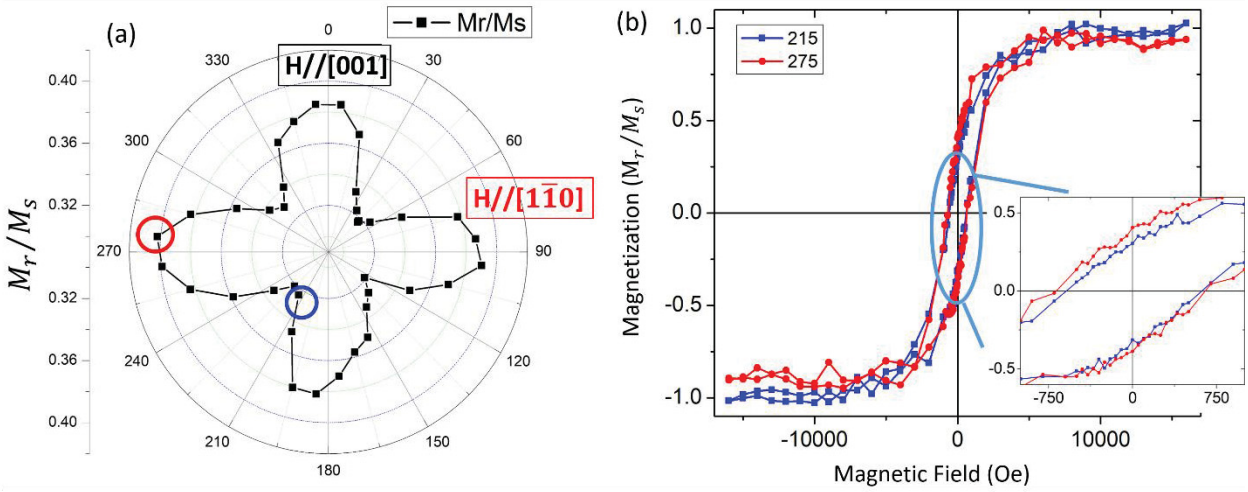

Figure 6.49. In-plane angle induced magnetic anisotropy of BFO-NZAFO/(110) STO heterostructure. The insert shows the M-H loops of chosen points, as shown in the blue and red circled dot in main figure.

6.6. Summary

In summary, a BFO-NZAFO nanobelt heterostructure was epitaxially grown on (110) STO by SPLD. This nanobelt structure extended throughout the entire film thickness, forming a BFO matrix embedded with the NZAFO nanobelts, as confirmed by TEM cross-sectional imaging and EDS mapping. This self-assembled layer displayed good epitaxy, as shown by XRD and SADP. M-H loop measurements revealed that the magnetic anisotropy favored an easy axis along the IP, and a dramatically increased magnetic shape anisotropy. The enhanced shape anisotropy enabled control of the coercivity, from 2 Oe (single NZAFO film) to about 50 Oe (self-assembled BFO-NZAFO). Rotation along the $[1\bar{1}0]$ direction resulted in a [001] hard axis, and the shape of the nanobelt created two different easy axes along $\theta = \pm 30°$. An IP rotation of about [110] demonstrated an easy axes along the $[1\bar{1}0]$ direction, which aligned with the nanobelt orientation. These findings confirm that a reliable approach exists for altering the coercivity and anisotropy of low-loss spinel ferrites by self-assembling nanostructures.

CHAPTER 7: STUDY OF CFO-SRO/PMN-PT NANOPILLAR HETEROSTRUCTURE: PATTERNED NANOGRATED ELECTRODES FOR ENHANCED FUNCTIONAL PROPERTIES WITH POLAR NANO-REGIONS REORIENTATION

7.1. Overview of CFO-SRO/PMN-PT Nanopillar Heterostructure

$Pb(Mg_{1/3}Nb_{2/3})_{0.70}Ti_{0.30}O_3$ (PMN-30PT) single crystals have been widely studied as an important type of piezoelectric material with a giant piezoelectric response[18,71,149-151]. Notably, this characteristic means that they are often incorporated in multiferroic heterostructures[152-155]. The enhanced piezoelectric properties of PMN-PT are attributed to its proximity to a morphotropic phase boundary (MPB)[156,157], which is a special regional phase boundary between the tetragonal (T) and rhombohedral (R) ferroelectric phases[78,158]. For PMN-PT compositions near the MPB, mixed phases have also been reported where structurally bridging monoclinic (M) states to the T and R ones[11] result in significant piezoelectricity[62], as well as enhanced dielectric properties[158,159].

Previous studies have revealed polar nano-regions (PNRs)[160] with a high density of twin walls in PMN-PT, which can then self-assemble along different crystallographically equivalent directions into hierarchical domain structures[158]. The redistribution of PNRs under an E field within the hierarchical domain structures serves to enhance the electromechanical properties of PMN-PT. A recent study has shown that patterned nano-electrodes (Au/MnO_x) fabricated on one side of PMN-PT single crystals did enhance the piezoelectric d_{33} and dielectric constants[158]. Specifically, an electric field gradient was coupled to the PNRs, thereby enhancing stored mechanical energy density and resulting dielectric properties. The patterning of Au/MnO_x nano-electrodes was achieved using Lloyd's mirror interference lithography (LIL), a process that is known to be complex and expensive.

A $CoFe_2O_4$-$SrRuO_3$ (CFO-SRO) nanopillar heterostructure was recently reported, which consisted of CFO nanopillars within a SRO matrix[159]. In this heterostructure, the SRO serves as the conductive material and the CFO as an insulating ceramic oxide. This unique conductive/insulated heterostructure can then be deposited on PMN-PT single crystals, creating patterned electrodes. Also important to the current investigation is that switched pulsed laser deposition (SPLD), which is a method that uses alternating targets during deposition, can simplify the fabrication of self-assembled heterostructures[56,106].

Herein we report the fabrication of self-assembled CFO-SRO nanopillar heterostructure layers deposited on (110) oriented PMN-30PT single crystal substrates. The CFO nanopillar was then embedded in a SRO matrix, creating a unique nano-patterned electrode on PMN-PT that evidenced enhanced piezoelectric and dielectric constants.

7.2. Experiment Method

Two different targets, SRO and CFO (purity>99.9%), were obtained from the Kurt J. Lesker Company. Substrates of (100) PMN-30PT were grow by the Shanghai Institute of Ceramics at the Chinese Academy Sciences. Prior to deposition, the substrates were ultra-sonicated with acetone and alcohol. The atomic fraction of CFO to SRO was controlled to be approximately 1:3. These two targets were epitaxially deposited using the SPLD technique, resulting in a bilayer structure. First, an SRO single layer was deposited at 700℃ using an energy density of 1.2 J/cm^2 and an O_2 atmosphere of 150 mTorr for 2 min. The target was then switched to CFO, which was deposited for 3 min at 700℃, 1.2 J/cm^2 and 150 mTorr. This procedure was repeated 10 times. The samples were then annealed at 700℃ and 100 Torr O_2. Atomic force microscopy (AFM) images were obtained (Dimension 3100, Vecco). Cross-sectional samples were fabricated using the focused ion

beam technique (FIB, FEI Helios 600 NanoLab). Cross-sectional images, selected area electron diffraction patterns (SADP), and x-ray spectra (EDS) were measured using transmission electron microscopy (TEM, JEOL 2100). The crystal structures were determined by X-ray diffraction (XRD; Philips X'Pert system) and SADP. Magnetic hysteresis curves were recorded using a vibrating sample magnetometer (Microsense, EZ-9). The dielectric constant was measured at 1kHz by a precision impedance analyzer (Agilent, 4249A). The samples were poled by an applied electric field (E) prior to obtaining measurements, and then subsequently annealed for 2 hours at 250℃ for de-poling.

7.3. Morphology, Composition & Epitaxy of CFO-SRO/PMN-PT Nanopillar Heterostructure

Figure 7.50 (b) show the topography of a CFO-SRO/PMN-30PT vertically integrated heterostructure obtained from AFM scans. The surface exhibits a dense nanopillar structure. The nanopillar were square in shape, with an average size of ~20nm, which corresponds with prior literature findings[159,161].

In order to determine whether the nanopillars of CFO were fully self-assembled, cross-sectional TEM images were obtained, as shown in Figure 7.50 (a). As denoted by the red-dashed boxes, the formation of nanopillars can be seen clearly. The total film thickness was about 30nm, which was significantly thinner compared to prior reports (~150nm)[159]. It should also be noted that the nanopillars extended out from the surface. The aspect ratio of the CFO nanopillar was about 4. To determine the epitaxial quality of the vertically integrated nanopillar structure, both SADP and X-ray diffraction (XRD) line scans were obtained, as given in Figures 7.50 (c) and (d). The SADP clearly shows the diffraction patterns of SRO (100), CFO (400), and PMN-30PT (100).

The d-spacings of these peaks were recorded to be $d_{SRO} = 3.944\text{Å}$, $d_{CFO} = 2.083\text{Å}$, and $d_{PMN-30PT} = 4.032\text{Å}$, respectively. As shown in Figure 1(d), the XRD line scans shows similar CFO (400), SRO (200), and PMN-30PT (200) peaks. The CFO (400) peak located near 43.52°, yielding a lattice parameter of $a_{CFO} = 8.312\text{Å}$, had a compressive strain of ~-0.95% compared to bulk CFO ($a_{CFO-Bulk} = 8.392\text{Å}$[11]). The SRO (200) peak was near 46.29°, yielding $a_{SRO} = 3.919$ Å with a tensile strain of ~0.23% ($a_{SRO-Bulk} = 3.910\text{Å}$[11]). Finally, the PMN-30PT (200) peaks were around 44.99°, indicating mixed phases, similar to prior reports[71,156]. The peaks measured from XRD line scans corroborated the diffraction patterns from TEM, illustrating good epitaxy of the heterostructures.

Figure 7.50 (e) shows a high-resolution TEM (HRTEM) image in the vicinity of the CFO nanopillar. The d-spacing calculated from the HRTEM image was ~2.08Å, which is consistent with that of CFO (Fig. 7.50 (c)). The d-spacing of the matrix phase of the heterostructure was determined to be ~3.93Å, while that of the substrate was ~4.03Å, which correspond to the SRO matrix and the PMN-30PT substrate, respectively. Obtained HRTEM images confirmed the presence of the SRO matrix and CFO nanopillar phases within the heterostructural layer. Clearly, a self-assembled structure has successfully been formed.

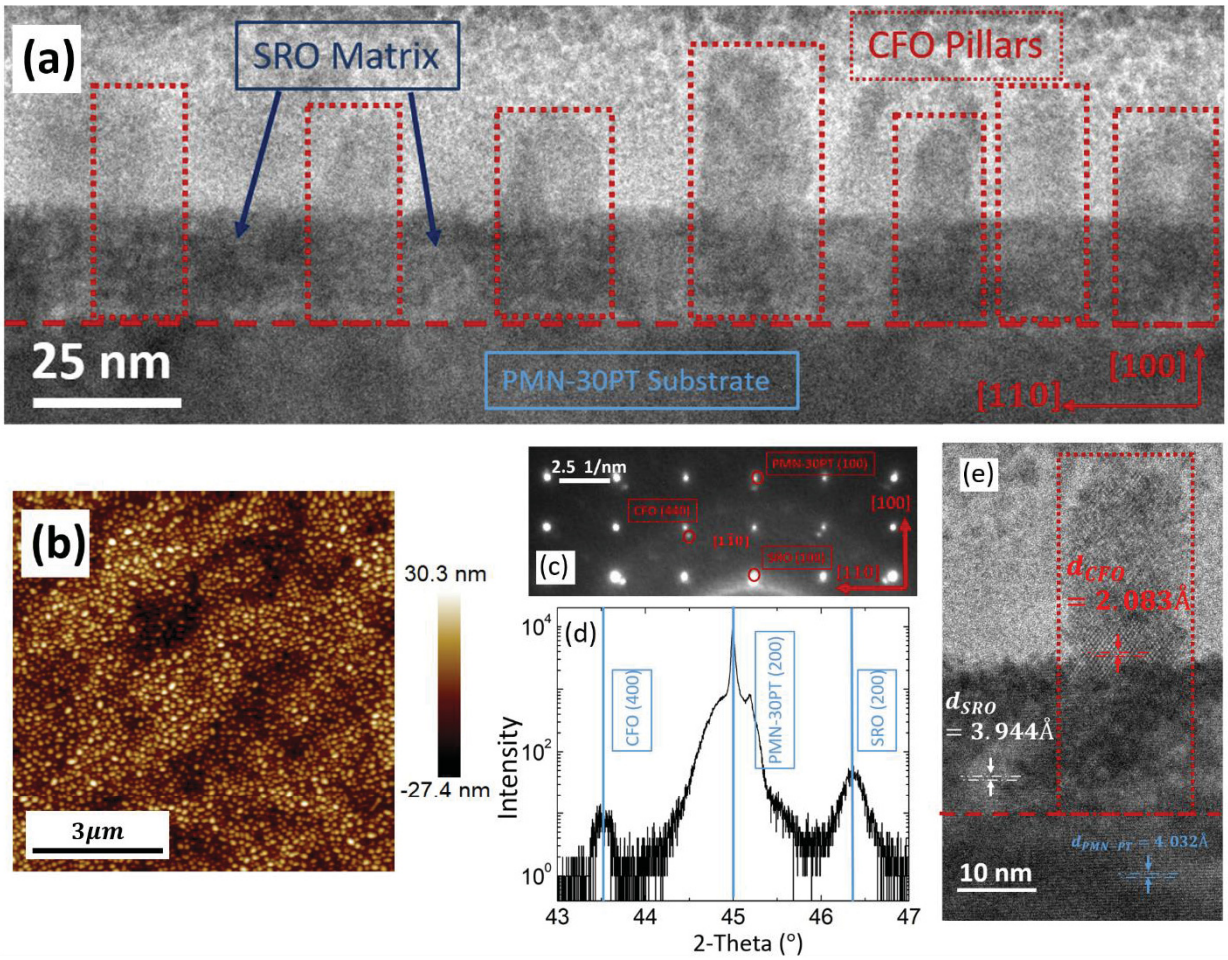

Figure 7.50. Structural studies of SRO-CFO/PMN-30PT nanopillar heterostructures (a): Cross-sectional TEM images. (b): AFM image. (c) & (d): SADP & XRD line scan. (e) HR-TEM of a CFO nanopillar embedded in SRO matrix.

7.4. Magnetic Properties of the CFO-SRO/PMN-PT Nanopillar Heterostructure

Figure 7.51 (a) shows an M-H loops along both the in-plane (IP) and out-of-plane (OP) directions. As can be seen from the figure, the easy axis was altered from lying along the IP, which is the normal easy axis of films, to the OP direction. This change can be attributed to the magnetic shape anisotropy of the CFO nanopillar structure[39]. Figure 7.51 (b) shows a rotation measurement of magnetic coercivity (H_c), confirming the significantly larger value for the OP direction (H_{c-OP}~3800 Oe) and the smaller value for the IP direction (H_{c-IP}~300 Oe), which contradicts analogous data for single phase magnetic film heterostructures[11]. According to Wang et al.[39], magnetic coercivity is impacted by magnetic shape anisotropy, as described by $H_{shape} = 2\varepsilon_{shape}/M_s$: where $\varepsilon_{shape} = 2\pi(N_x - N_z){M_s}^2$, N_z is a demagnetization factor related to the aspect ratio, and $N_x = (1 - N_z)/2$[69]. Based on calculations from Beleggia et al.[148], the value of N_z is ~0.05 when the aspect ratio equals 4. Therefore, the difference in the calculated coercivity between IP and OP should be about 3.4 kOe. Note that the assessed values for coercivity, as indicated in in Figure 7.51 (a), confirms that the coercivity along the OP direction was ~3800 Oe, and ~300 Oe along the IP direction, demonstrating a coercivity difference of 3500 Oe. These data corroborate both experimental results and predicted values. Clearly, the dominant contribution to magnetic coercivity was due to magnetic shape anisotropy.

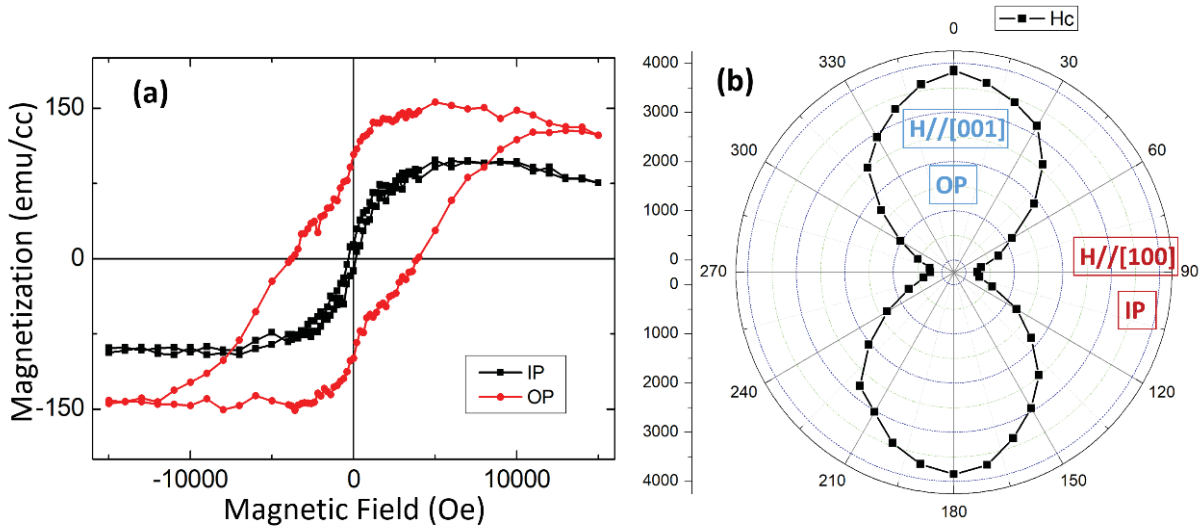

Figure 7.51. Magnetic properties of SRO-CFO/PMN-30PT heterostructures. (a): M-H loop, both along IP and the OP directions. (b): Magnetic coercivity as function of angular rotation along [110] direction.

7.5. RSM Peak Splitting of CFO-SRO/PMN-PT Nanopillar Heterostructure

Figure 7.52 shows RSM (reciprocal space mapping) results for both a PMN-PT substrates and a CFO-SRO/PMN-30PT heterostructure taken along the (100) zone axis. Images (a)-(d) refer to RSM results for CFO-SRO/PMN-30PT heterostructures under different E. Note that a single sharp peak along (00L) begins to split into two peaks with increasing E between 0 and 2kV/cm, as shown in Images (a) and (b). When E was increased to 6 kV/cm (Image (c)), the peaks became narrower along the longitudinal direction (00L), but much broader along the transverse direction (H00). With the removal of E (Image (d)), the broadness of the peak along the (H00) direction was retained. Images (e)-(h) refer to RSM results under a similar E-field history obtained along the (110) zone axis. Under an E-field of 2 kV/cm, as shown in Image (e), the original parallel peaks along both the (0LL) and (H00) directions began to split, creating a multiple-peak orientation, as

indicated by the blue- and red-dashed lines. This splitting and broadening pattern continued under higher E-fields (Image (c)), and persisted upon removal of E (Image (d)). This peak broadening with E for the CFO-SRO/PMN-30PT heterostructures proved to be similar to prior reports using nanograted Au/MnO_x patterned electrodes[158].

Peak broadening along the (100) zone axis can be attributed to the coupling of a gradient in the electric field induced by nanograted electrodes and PNR distribution. Moreover, PNR distribution tends to become maladjusted by the field gradient, resulting in an excess of stored elastic energy[158,160,162,163]. According to Gao et al.[158], the E gradient is stronger along [011] and [$0\bar{1}1$]. Consequently, for the (011) zone axis, the gradients of E creates two types of R macro domains, leading to the observed splitting and broadening of the multiple parallel peaks. To demonstrate the effects of the nano-electrodes, similar RSM measurements were obtained for PMN-30PT single crystals, as shown in Figure 7.53. When a similar E history was applied on the PMN-30PT single crystals, peak broadening and splitting did not occur, which contrasted with our results for the CFO-SRO/PMN-30PT heterostructure. These findings confirm that nanograted electrodes play an important role in PNR distribution.

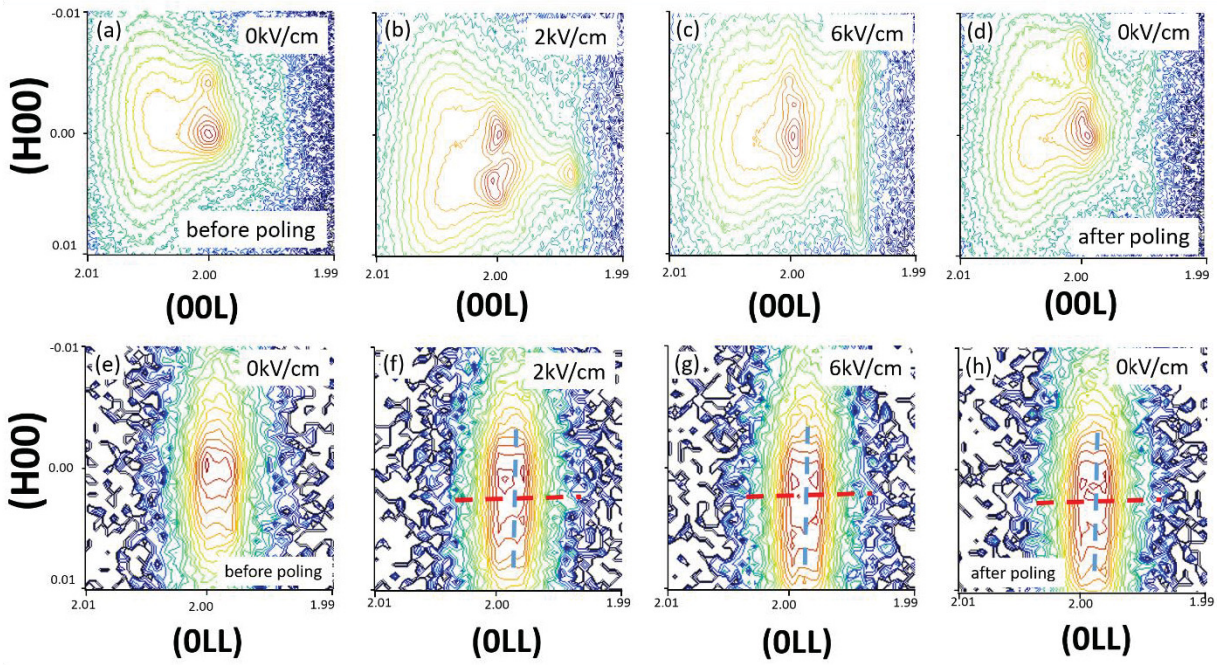

Figure 7.52. RSM images of SRO-CFO/PMN-30PT heterostructures. (a)-(d) Along the (100) zone axis under different E-fields. (e)-(h) Along the (110) zone axis under different E-fields.

Figure 7.53 provides RSM results for the PMN-30PT under the same E history utilized for the CFO-SRO/PMN-30PT heterostructure.

Images (a)-(d) present RSM results for the PMN-PT substrate along the (100) zone axis. Note the absence of peak broadening along the transverse direction. Images (e)-(h) provide analogous RSM results for the (110) zone axis. Similarly to Fig. 7.53 (a)-(d), the broadening and splitting did not occurred when a similar E-field history was applied.

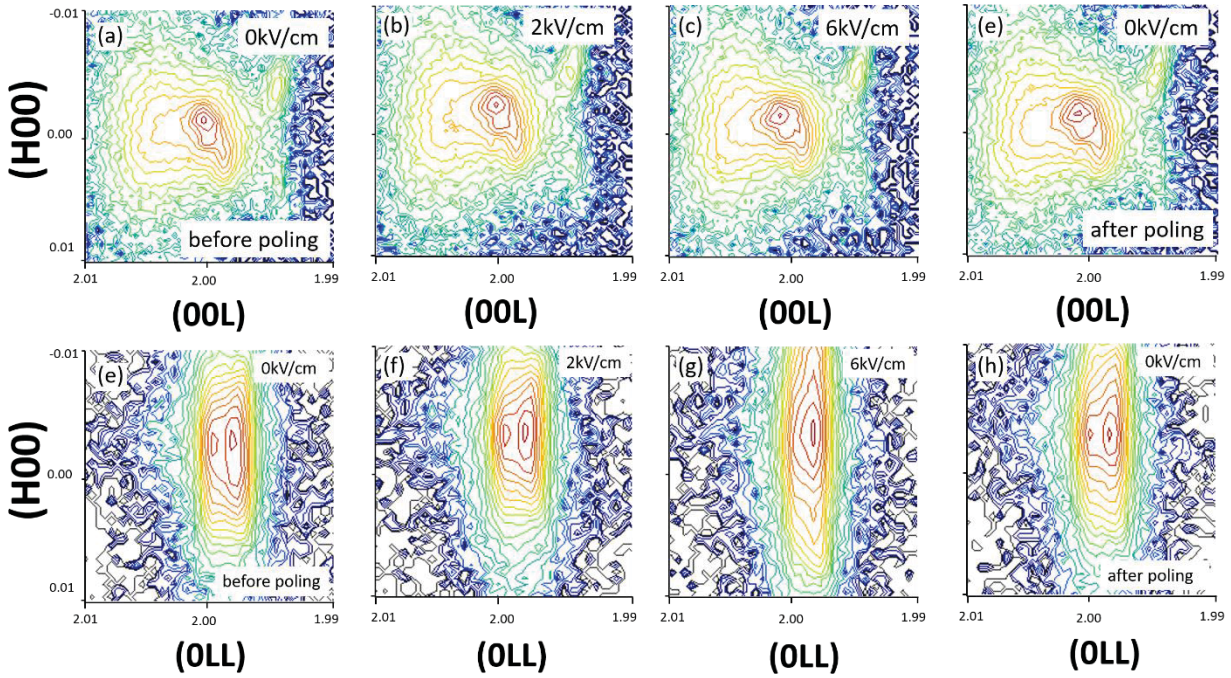

Figure 7.53. RSM images of PMN-30PT. (a)-(d) Along (100) zone axis under different E-fields. (e)-(h) Along (110) zone axis under different E-fields.

7.6. Dielectric Constant Enhancement of CFO-SRO/PMN-PT Nanopillar Heterostructure

Figure 7.54 (a) shows the dielectric constant (K) for both a PMN-PT substrate and a CFO-SRO/PMN-PT heterostructure as a function of E, taken at a frequency of 1 kHz. Note that K begins to be enhanced with increasing E above 2kV/cm for CFO-SRO/PMN-30PT, reaching a plateau for E>4 kV/cm; the value of K then increased from ~3500 to ~6500. These results are similar to previous reports for PMN-PT crystals with nanograted electrodes (Au/MnO_x) [158], where K reached ~7000 after poling. For the PMN-30PT sample without a vertically integrated nanopillar structure, the dielectric constant was only ~5200 after poling. Figure 4 (b) shows the strain as a function of E for a CFO-SRO/PMN-30PT heterostructure and a PMN-30PT crystal substrate. These data were

calculated from XRD scans. The coercivity of the PMN-30PT crystal was reduced, and its induced strain o was increased by depositing a self-assembled nano-patterned CFO-SRO layer. These data clearly demonstrate that the piezoelectric properties of the PMN-30PT crystal could be increased through the addition of a CFO-SRO layer, while its hysteretic losses significantly decreased.

Our results confirmed that enhanced dielectric and piezoelectric properties can be induced by the incorporation of CFO-SRO nano-patterned electrodes on a PMN-30PT substrate. Although this approach is similar to the one used for the development of Au/MnO_x nanograted electrodes, in this instance the deposition process is simpler and thus has greater significance for next-generation devices and applications.

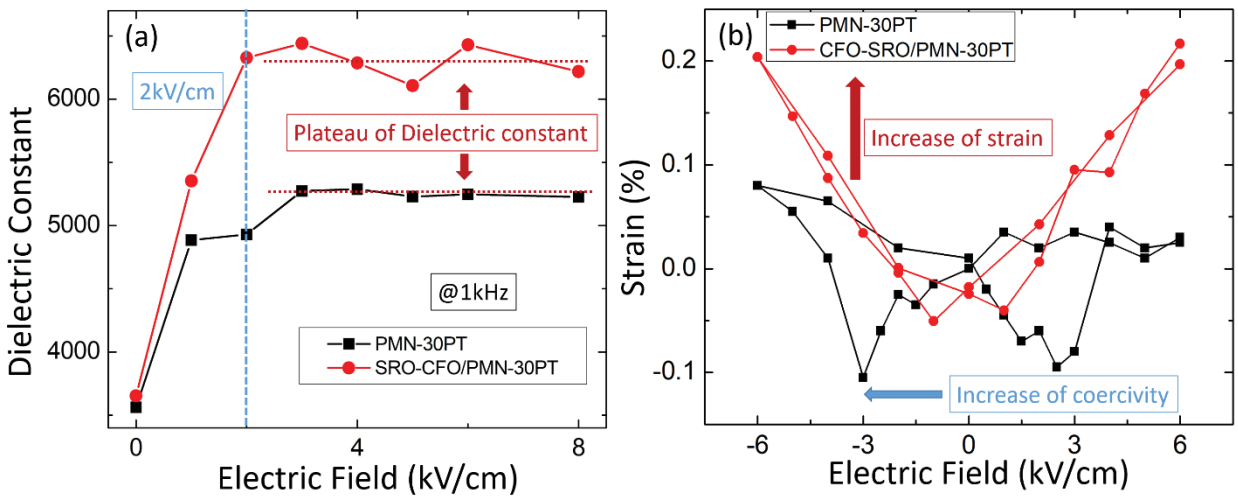

Figure 7.54. Dielectric constant of both a PMN-30PT substrate and a SRO-CFO/PMN-30PT heterostructure as a function of E-field.

7.7. Summary

The findings obtained from this investigation demonstrate the feasibility of developing vertically integrated self-assembled SRO-CFO nanopillar heterostructures epitaxially grown on a PMN-PT substrate. Accordingly, by controlling the nanopillar heterostructures and conductivity of SRO, nano-patterned electrodes could be created. The CFO-SRO self-assembled nanopillar structure represents a simplified method for fabricating nano-patterned electrodes than previously reported methods. Moreover, this approach has been shown to result in higher dielectric and piezoelectric properties, offering greater potential for enhancing magnetoelectric effects in integrated systems.

CHAPTER 8: SUMMARY

In this project, we explored the ME coupling of different piezoelectric/magnetostrictive materials. By introducing self-assembled nanostructures—(1-3) vertically integrated and (3-1) horizontally integrated nanostructures—notably enhanced coupling coefficients were achieved, resulting in improved magnetoelectricity, magnetostriction, and piezoelectricity.

Firstly, after introducing PMN-xPT (x=33, 35.5, 38) single crystal substrates, the resulting nanopillar BFO-CFO two-phase layers were found to exhibit increased ME coupling . Specifically, the value of $\Delta M/M_{rDC}$ was found to be ~90%, which is about 1.5 times larger than reported in prior studies. The converse magnetoelectric coupling coefficient was calculated to be 1.3×10^{-7} s/m, representing a threefold magnitude increase in comparison to signal-layer heterostructures on PMN-PT. Multiple stable magnetization states ($N \geq 4$) were found upon the removal of the E field.

Secondly, CuFO, which has smaller loss and higher quality factor, was introduced into the self-assembled nanopillar heterostructures with a BFO matrix. These self-assembled (1-3) heterostructures exhibited significantly higher ME coefficient (α) values in comparison with $\alpha \approx 0$ for the single-layer CuFO ones. These findings illustrate a desirable balance between quality factor enhancements and magnetostriction. Moreover, our data indicate that the introduced nanopillar heterostructures have the potential to enhance the magnetoelectricity of materials with weak magnetostriction, while maintaining their utility for advanced applications but higher quality factors.

Thirdly, we investigated stable magnetization states for the self-assembled nanostructures; specifically, we showed that when (1-3) heterostructures were introduced, magnetization levels

increased to 4. Therefore, we investigated stable magnetization states for these vertically integrated heterostructures. Experimental results shows that both BFO-CFO and BFO-CuFO (1-3) heterostructures have two remnant magnetization states upon removal of E_{DC}. If an additional H-field input was induced, two additional remnant magnetization states were accessible. These findings also demonstrated the non-volatility of typically volatile materials. In summary, these experimental assays were useful in eliminating the uncertainty and non-uniformity of the PMN-PT substrates, as well as helped to identify a much broader compositional range for choice of the PMN-xPT single crystal substrates. Moreover, multi-bit in a cell is possible if this heterostructures are introduced into the devices and applications.

Fourthly, a new ferrite material demonstrating much smaller losses and improved performance was studied and then self-assembled with a BFO matrix to form a nano-belt heterostructures. Specifically, a BFO-NZAFO nanobelt heterostructure was epitaxially grown on (110) STO. By introducing the BFO matrix, a NZAFO nanobelt was formed; moreover, the magnetic anisotropy and easy axis were altered by the induced magnetic shape anisotropy, and the shape of the nanobelt created two different easy axes along $\theta = \pm 30°$ from the IP direction. These findings confirm that a reliable approach exists for altering the coercivity and anisotropy of low-loss spinel ferrites through the incorporation of self-assembling nanostructures.

Finally, we investigated self-assembled SRO-CFO nanopillar heterostructures epitaxially grown on PMN-PT substrates. By controlling the nanopillar heterostructures and conductivity of SRO, nano-patterned electrodes were fabricated. The resulting CFO-SRO self-assembled nanopillar structure for a higher piezoelectric and dielectric constant, and demonstrates a simplified method for making nano-patterned electrodes in comparison to previously reported methods. Additionally, the deposition of magnetostrictive materials on these patterned nano

electrodes will likely evidence higher ME coupling, which will be important for next-generation devices and applications.

In summary, this investigation confirmed the potential of self-assembled vertically/horizontally integrated heterostructures that show enhanced ME properties, multiple stable magnetization states, altered magnetic anisotropy, and enhanced piezoelectric properties. Based on the field input source (E field versus H field), one can manipulate the resulting states or properties without physically changing the devices or applications. Additionally, self-assembled vertically/horizontally heterostructures have the potential to create multiple stable states ($N \geq 4$), which could be used for the fabrication of logic or multi-bit memory devices. These advantages all have significant promise for the development of reconfigurable electronic approaches and devices.

PUBLICATIONS

1. Tang, X., Viswan, R., Gao, M., Leung, C. M., Folger, C., Luo, H., ... & Viehland, D. (2018). Nanopillars with E-field accessible multi-state (N≥ 4) magnetization having giant magnetization changes in self-assembled BiFeO 3-CoFe 2 O 4/Pb (Mg 1/3 Nb 2/3)-38at% PbTiO 3 heterostructures. *Scientific reports*, *8*(1), 1628
2. Tang, X., Gao, M., Leung, C. M., Luo, H., Li, J., & Viehland, D. (2019). Non-volatility using materials with only volatile properties: Vertically integrated magnetoelectric heterostructures and their potential for multi-level-cell devices. *Applied Physics Letters*, *114*(24), 242903.
3. Tang, X., Leung, C. M., Gao, M., Winkler, C., Luo, H., Li, J., & Viehland, D. (2019). Nanostructure-enhanced magnetoelectric/magnetostrictive properties and reduced losses in self-assembled epitaxial CuFe2O4–BiFeO3 layers on Pb (Mg1/3Nb2/3) O3–33at% PbTiO3 crystals. *Journal of the American Ceramic Society*, *102*(9), 5192-5202.
4. Gao, M., Viswan, R., Tang, X., Leung, C. M., Li, J., & Viehland, D. (2018). Magnetoelectricity of CoFe 2 O 4 and tetragonal phase BiFeO 3 nanocomposites prepared by pulsed laser deposition. *Scientific reports*, *8*(1), 323.
5. Gao, M., Viswan, R., Tang, X., Leung, C. M., Li, J., & Viehland, D. (2017). E-field controlled phase transformation in bismuth ferrite thin films, and effect of laser energy density. *Applied Physics Letters*, *111*(15), 152905.
6. Gao, M., Tang, X., Leung, C. M., Dai, S., Li, J., & Viehland, D. D. (2019). Phase transition and energy storage behavior of antiferroelectric PLZT thin films epitaxially deposited on SRO buffered STO single crystal substrates. *Journal of the American Ceramic Society*.

7. Gao, M., Tang, X., Dai, S., Li, J., & Viehland, D. (2019). Depth dependent ferroelectric to incommensurate/commensurate antiferroelectric phase transition in epitaxial lanthanum modified lead zirconate titanate thin films. *Applied Physics Letters*, *115*(7), 072901.
8. Leung, C. M., Zhuang, X., Gao, M., Tang, X., Xu, J., Li, J., ... & Viehland, D. (2017). Enhanced stability of magnetoelectric gyrators under high power conditions. *Applied Physics Letters*, *111*(18), 182901.
9. Leung, C. M., Sreenivasulu, G., Zhuang, X., Gao, M., Tang, X., Xu, J., ... & Viehland, D. (2018). Stability enhancement of yttrium substituted nickel zinc ferrite/PZT magnetoelectric gyrators under high power conditions. *Applied Physics Letters*, *112*(24), 242901.
10. Leung, C. M., Sreenivasulu, G., Zhuang, X., Tang, X., Gao, M., Xu, J., ... & Viehland, D. (2018). A Highly Efficient Self-Biased Nickel-Zinc Ferrite/Metglas/PZT Magnetoelectric Gyrator. *physica status solidi (RRL)–Rapid Research Letters*, *12*(5), 1800043.
11. Leung, C. M., Zhuang, X., Xu, J., Gao, M., Tang, X., Li, J., ... & Viehland, D. (2018). A dual-output magnetoelectric gyrator. *Journal of Physics D: Applied Physics*, *52*(6), 065003.

REFERENCES

1 Kimura, T. *et al.* Magnetocapacitance effect in multiferroicBiMnO3. *Physical Review B* **67**, doi:10.1103/PhysRevB.67.180401 (2003).

2 Galdi, A. *Magnetic, orbital and transport properties in LaMnO3 based heterostructures*, Université de Caen; Università degli studi di Salerno, (2011).

3 Eerenstein, W., Mathur, N. D. & Scott, J. F. Multiferroic and magnetoelectric materials. *Nature* **442**, 759-765, doi:10.1038/nature05023 (2006).

4 Nan, C. W., Bichurin, M. I., Dong, S. X., Viehland, D. & Srinivasan, G. Multiferroic magnetoelectric composites: Historical perspective, status, and future directions. *Journal of Applied Physics* **103**, 031101, doi:10.1063/1.2836410 (2008).

5 Scott, J. F. Data storage. Multiferroic memories. *Nat Mater* **6**, 256-257, doi:10.1038/nmat1868 (2007).

6 Velev, J. P., Jaswal, S. S. & Tsymbal, E. Y. Multi-ferroic and magnetoelectric materials and interfaces. *Philos Trans A Math Phys Eng Sci* **369**, 3069-3097, doi:10.1098/rsta.2010.0344 (2011).

7 Ma, J., Hu, J., Li, Z. & Nan, C. W. Recent progress in multiferroic magnetoelectric composites: from bulk to thin films. *Adv Mater* **23**, 1062-1087, doi:10.1002/adma.201003636 (2011).

8 Chu, Y. H. *et al.* Electric-field control of local ferromagnetism using a magnetoelectric multiferroic. *Nat Mater* **7**, 478-482, doi:10.1038/nmat2184 (2008).

9 Schmid, H. Multi-ferroic magnetoelectrics. *Ferroelectrics* **162**, 317-338, doi:10.1080/00150199408245120 (1994).

10 Tang, X. *et al.* Nanopillars with E-field accessible multi-state (N >/= 4) magnetization having giant magnetization changes in self-assembled BiFeO3-CoFe2O4/Pb(Mg1/3Nb2/3)-38at%PbTiO3 heterostructures. *Sci Rep* **8**, 1628, doi:10.1038/s41598-018-19673-8 (2018).

11 Gao, M. *et al.* E-field controlled phase transformation in bismuth ferrite thin films, and effect of laser energy density. *Applied Physics Letters* **111**, 152905, doi:Artn 152905 10.1063/1.4997017 (2017).

12 Tokunaga, Y. *et al.* Composite domain walls in a multiferroic perovskite ferrite. *Nat Mater* **8**, 558-562, doi:10.1038/nmat2469 (2009).

13 Dong, S., Liu, J. M., Cheong, S. W. & Ren, Z. F. Multiferroic materials and magnetoelectric physics: symmetry, entanglement, excitation, and topology. *Advances in Physics* **64**, 519-626, doi:10.1080/00018732.2015.1114338 (2015).

14 Goodenough, J. B. Direct Cation-Cation Interactions in Primarily Ionic Solids. *Journal of Applied Physics* **31**, S359-S361, doi:Doi 10.1063/1.1984748 (1960).

15 Goodenough, J. B. Metallic oxides. *Progress in solid state chemistry* **5**, 145-399 (1971).

16 Supryadkina, I. A., Abgaryan, K. K., Bazhanov, D. I. & Mutigullin, I. V. Study of the Polarizations of (Al,Ga,AlGa)N Nitride Compounds and the Charge Density of Various Interfaces Based on Them. *Semiconductors* **47**, 1621-1625, doi:10.1134/S106378261312018x (2013).

17 Jeong, Y. K., Bark, C. W., Ryu, S., Lee, J. H. & Jang, H. M. R3c-R3m Octahedron-tilting Transition in Rhombohedrally-distorted BiFeO3 Multiferroics. *Journal of the Korean Physical Society* **58**, 817-820, doi:10.3938/jkps.58.817 (2011).

18 Gao, M. *et al.* Magnetoelectricity of CoFe 2 O 4 and tetragonal phase BiFeO 3 nanocomposites prepared by pulsed laser deposition. *Scientific reports* **8**, 323 (2018).
19 Wang, W. G., Li, M., Hageman, S. & Chien, C. L. Electric-field-assisted switching in magnetic tunnel junctions. *Nat Mater* **11**, 64-68, doi:10.1038/nmat3171 (2011).
20 Khalili Amiri, P. *et al.* Electric-Field-Controlled Magnetoelectric RAM: Progress, Challenges, and Scaling. *IEEE Transactions on Magnetics* **51**, 1-7, doi:10.1109/tmag.2015.2443124 (2015).
21 Nan, T. *et al.* Quantification of strain and charge co-mediated magnetoelectric coupling on ultra-thin Permalloy/PMN-PT interface. *Sci Rep* **4**, 3688, doi:10.1038/srep03688 (2014).
22 Zhang, C. *et al.* Electric field mediated non-volatile tuning magnetism at the single-crystalline Fe/Pb(Mg1/3Nb2/3)0.7Ti0.3O3 interface. *Nanoscale* **7**, 4187-4192, doi:10.1039/c4nr05847j (2015).
23 Wei, Y. *et al.* Four-state memory based on a giant and non-volatile converse magnetoelectric effect in FeAl/PIN-PMN-PT structure. *Sci Rep* **6**, 30002, doi:10.1038/srep30002 (2016).
24 Zhang, S. *et al.* Giant electrical modulation of magnetization in Co40Fe40B20/Pb(Mg1/3Nb2/3)0.7Ti0.3O3(011) heterostructure. *Sci Rep* **4**, 3727, doi:10.1038/srep03727 (2014).
25 Khitun, A., Bao, M. Q. & Wang, K. L. Spin wave magnetic nanofabric: A new approach to spin-based logic circuitry. *Ieee Transactions on Magnetics* **44**, 2141-2152, doi:10.1109/Tmag.2008.2000812 (2008).
26 Boyn, S. *et al.* Learning through ferroelectric domain dynamics in solid-state synapses. *Nat Commun* **8**, 14736, doi:10.1038/ncomms14736 (2017).
27 Al'Shin, B., Astrov, D., Tishchenko, A. & Petrov, S. Magnetoelectric effect in BaCoF4. *ZhETF Pisma Redaktsiiu* **12**, 206 (1970).
28 Ascher, E., Rieder, H., Schmid, H. & Stössel, H. Some Properties of Ferromagnetoelectric Nickel‐Iodine Boracite, Ni3B7O13I. *Journal of Applied Physics* **37**, 1404-1405 (1966).
29 Astrov, D. N. The Magnetoelectric Effect in Antiferromagnetics. *Soviet Physics Jetp-Ussr* **11**, 708-709 (1960).
30 Dzyaloshinskii, I. E. On the Magneto-Electrical Effect in Antiferromagnets. *Soviet Physics Jetp-Ussr* **10**, 628-629 (1960).
31 Folen, V., Rado, G. & Stalder, E. Anisotropy of the magnetoelectric effect in Cr 2 O 3. *Physical Review Letters* **6**, 607 (1961).
32 Hulin, N. *Physique et humanités scientifiques: Autour de la réforme de l'enseignement de 1902. Études et Documents*. (Presses Univ. Septentrion, 2000).
33 Hosseini, S. A. & Tafreshi, H. V. On the importance of fibers' cross-sectional shape for air filters operating in the slip flow regime. *Powder Technology* **212**, 425-431, doi:10.1016/j.powtec.2011.06.025 (2011).
34 Kim, J. K., Kim, S. S. & Kim, W.-J. Sol–gel synthesis and properties of multiferroic BiFeO3. *Materials Letters* **59**, 4006-4009 (2005).
35 Pradhan, A. K. *et al.* Magnetic and electrical properties of single-phase multiferroic BiFeO 3. *Journal of Applied Physics* **97**, 093903 (2005).
36 Wang, J. *et al.* Epitaxial BiFeO3 multiferroic thin film heterostructures. *Science* **299**, 1719-1722, doi:10.1126/science.1080615 (2003).

37 Li, J. *et al.* Self-assembled multiferroic nanostructures in the Co Fe 2 O 4-Pb Ti O 3 system. *Applied Physics Letters* **87**, 072909 (2005).
38 Nan, C.-W., Liu, G. & Lin, Y. Influence of interfacial bonding on giant magnetoelectric response of multiferroic laminated composites of Tb 1− x Dy x Fe 2 and PbZr x Ti 1− x O 3. *Applied Physics Letters* **83**, 4366-4368 (2003).
39 Wang, Z. *et al.* Engineered Magnetic Shape Anisotropy in BiFeO3–CoFe2O4 Self-Assembled Thin Films. *Acs Nano* **7**, 3447-3456 (2013).
40 Jin, T. L. *et al.* The E-Field-Induced Volatile and Nonvolatile Magnetization Switching of CoNi Thin Films in CoNi/PMN-PT Heterostructures. *Ieee Transactions on Magnetics* **51**, 1-3, doi:10.1109/Tmag.2015.2443179 (2015).
41 Leung, C. M. *et al.* Power conversion efficiency and resistance tunability in coil-magnetoelectric gyrators. *Applied Physics Letters* **109**, 202907, doi:10.1063/1.4967846 (2016).
42 Wang, F., Zhou, C., Gesang, D. & Jiang, C. Electric field control of magnetization reorientation in Co/Pb (Mg1/3Nb2/3)-PbTiO3 heterostructure. *Nanoscale Res Lett* **12**, 104, doi:10.1186/s11671-017-1866-6 (2017).
43 Ortega, N., Kumar, A., Scott, J. F. & Katiyar, R. S. Multifunctional magnetoelectric materials for device applications. *J Phys Condens Matter* **27**, 504002, doi:10.1088/0953-8984/27/50/504002 (2015).
44 Akbashev, A. R. & Kaul, A. R. Structural and chemical aspects of the design of multiferroic materials. *Russian Chemical Reviews* **80**, 1159-1177, doi:10.1070/RC2011v080n12ABEH004239 (2011).
45 Li, Y. *et al.* Magnetoelectric quasi-(0-3) nanocomposite heterostructures. *Nat Commun* **6**, 6680, doi:10.1038/ncomms7680 (2015).
46 Zhang, Y. *Magnetoelectric Thin Film Heterostructures and Electric Field Manipulation of Magnetization*, Virginia Tech, (2015).
47 Phan, T. L., Zhang, Y. D., Yu, S. C., Khiem, N. V. & Phuc, N. X. Electron-spin-resonance study of Y-doped Nd0.7Sr0.3MnO3 ceramics. *Journal of Applied Physics* **111**, 07E114, doi:10.1063/1.3671796 (2012).
48 Wong, Z. M., Cheng, H., Yang, S.-W., Tan, T. L. & Xu, G. Q. Computational Design of Perovskite Ba x Sr1–x SnO3 Alloys as Transparent Conductors and Photocatalysts. *The Journal of Physical Chemistry C* **121**, 26446-26456 (2017).
49 Choudhary, R., Pradhan, D. K., Tirado, C., Bonilla, G. & Katiyar, R. Impedance characteristics of Pb (Fe2/3W1/3) O3–BiFeO3 composites. *physica status solidi (b)* **244**, 2254-2266 (2007).
50 Blake, G. *et al.* Spin structure and magnetic frustration in multiferroic R Mn 2 O 5 (R= Tb, Ho, Dy). *Physical Review B* **71**, 214402 (2005).
51 Wang, C., Guo, G. C. & He, L. Ferroelectricity driven by the noncentrosymmetric magnetic ordering in multiferroic TbMn(2)O(5): a first-principles study. *Phys Rev Lett* **99**, 177202, doi:10.1103/PhysRevLett.99.177202 (2007).
52 Leung, C. M. *et al.* Highly efficient solid state magnetoelectric gyrators. *Applied Physics Letters* **111**, 122904, doi:10.1063/1.4996242 (2017).
53 Zhang, N., Ke, W., Schneider, T. & Srinivasan, G. Dependence of the magnetoelectric coupling in NZFO–PZT laminate composites on ferrite compactness. *Journal of Physics: Condensed Matter* **18**, 11013 (2006).

54 Ma, Y., Cheng, W., Ning, M. & Ong, C. Magnetoelectric effect in epitaxial Pb (Zr 0.52 Ti 0.48) O 3 ⁄ La 0.7 Sr 0.3 Mn O 3 composite thin film. *Applied Physics Letters* **90**, 152911 (2007).
55 Kim, D. H. *et al.* Combinatorial pulsed laser deposition of Fe, Cr, Mn, and Ni-substituted SrTiO3 films on Si substrates. *ACS Comb Sci* **14**, 179-190, doi:10.1021/co2001185 (2012).
56 Aimon, N. M., Kim, D. H., Choi, H. K. & Ross, C. A. Deposition of epitaxial BiFeO3/CoFe2O4 nanocomposites on (001) SrTiO3 by combinatorial pulsed laser deposition. *Applied Physics Letters* **100**, 092901, doi:10.1063/1.3690957 (2012).
57 Dong, G. H. *et al.* The phase transition and superior multiferroic properties of (Mn, Co) co-doped BiFeO3/CoFe2O4 double-layer films. *Journal of Alloys and Compounds* **654**, 419-423, doi:10.1016/j.jallcom.2015.09.144 (2016).
58 Yan, L. *et al.* Review of magnetoelectric perovskite–spinel self-assembled nano-composite thin films. *Journal of Materials Science* **44**, 5080-5094, doi:10.1007/s10853-009-3679-1 (2009).
59 Wang, Y., Hu, J. M., Lin, Y. H. & Nan, C. W. Multiferroic magnetoelectric composite nanostructures. *Npg Asia Materials* **2**, 61-68, doi:10.1038/asiamat.2010.32 (2010).
60 MacManus-Driscoll, J. L. *et al.* Strain control and spontaneous phase ordering in vertical nanocomposite heteroepitaxial thin films. *Nat Mater* **7**, 314-320, doi:10.1038/nmat2124 (2008).
61 Wang, Z. G. *et al.* Electrical and thermal control of magnetic coercive field in ferromagnetic/ferroelectric heterostructures. *Physical Review B* **89**, 035118, doi:ARTN 035118 10.1103/PhysRevB.89.035118 (2014).
62 Wang, Z. *et al.* Domain rotation induced strain effect on the magnetic and magneto-electric response in CoFe2O4/Pb(Mg,Nb)O3-PbTiO3 heterostructures. *Journal of Applied Physics* **111**, 034108, doi:10.1063/1.3684546 (2012).
63 Wang, Z., Wang, Y., Luo, H., Li, J. & Viehland, D. Crafting the strain state in epitaxial thin films: A case study of CoFe 2 O 4 films on Pb (Mg, Nb) O 3− PbTiO 3. *Physical Review B* **90**, 134103 (2014).
64 Wang, Z., Wang, Y., Ge, W., Li, J. & Viehland, D. Volatile and nonvolatile magnetic easy-axis rotation in epitaxial ferromagnetic thin films on ferroelectric single crystal substrates. *Applied Physics Letters* **103**, 132909, doi:Unsp 132909 10.1063/1.4823539 (2013).
65 Tang, X. *et al.* Nanostructure-enhanced magnetoelectric/magnetostrictive properties and reduced losses in self-assembled epitaxial CuFe2O4-BiFeO3 layers on Pb(Mg1/3Nb2/3)O3-33at%PbTiO3 crystals. *Journal of the American Ceramic Society* **0**, doi:10.1111/jace.16387 (2019).
66 Wang, Z., Yang, Y., Viswan, R., Li, J. & Viehland, D. Giant electric field controlled magnetic anisotropy in epitaxial BiFeO3-CoFe2O4 thin film heterostructures on single crystal Pb(Mg1/3Nb2/3)0.7Ti0.3O3 substrate. *Applied Physics Letters* **99**, 043110, doi:10.1063/1.3619836 (2011).
67 Yan, L. *Two phase magnetoelectric epitaxial composite thin films*, Virginia Tech, (2009).
68 Wu, M. H., Park, C. & Whitesides, G. M. Generation of submicrometer structures by photolithography using arrays of spherical microlenses. *Journal of Colloid and Interface Science* **265**, 304-309, doi:10.1016/S0021-9797(03)00311-4 (2003).

69 Zheng, H., Kreisel, J., Chu, Y.-H., Ramesh, R. & Salamanca-Riba, L. Heteroepitaxially enhanced magnetic anisotropy in BaTiO3–CoFe2O4 nanostructures. *Applied Physics Letters* **90**, 113113, doi:10.1063/1.2713131 (2007).
70 Zheng, H. *et al.* Multiferroic BaTiO3-CoFe2O4 Nanostructures. *Science* **303**, 661-663, doi:10.1126/science.1094207 (2004).
71 Tang, X. *et al.* Nanopillars with E-field accessible multi-state (N⩾ 4) magnetization having giant magnetization changes in self-assembled BiFeO 3-CoFe 2 O 4/Pb (Mg 1/3 Nb 2/3)-38at% PbTiO 3 heterostructures. *Scientific reports* **8**, 1628 (2018).
72 Yan, L., Bai, F. M., Li, J. F. & Viehland, D. Nanobelt Structure in Perovskite-Spinel Composite Thin Films. *Journal of the American Ceramic Society* **92**, 17-20, doi:10.1111/j.1551-2916.2008.02825.x (2009).
73 Gruverman, A., Auciello, O. & Tokumoto, H. Nanoscale investigation of fatigue effects in Pb(Zr,Ti)O3 films. *Applied Physics Letters* **69**, 3191-3193, doi:10.1063/1.117957 (1996).
74 Yi, G., Wu, Z. & Sayer, M. Preparation of Pb(Zr,Ti)O3 thin films by sol gel processing: Electrical, optical, and electro‐optic properties. *Journal of Applied Physics* **64**, 2717-2724, doi:10.1063/1.341613 (1988).
75 Yue, Z. *et al.* Resistive Switching and the Local Electric Field in Bi0.85-xPr0.15RExFe0.97Mn0.03O3/CuFe2O4 (RE = Sr, Dy) Bilayered Thin Films. *ACS Appl Mater Interfaces* **9**, 20205-20212, doi:10.1021/acsami.7b03579 (2017).
76 Shrout, T. R. & Fielding, J. in *Ultrasonics Symposium, 1990. Proceedings., IEEE 1990.* 711-720 (IEEE).
77 Park, S. E. & Shrout, T. R. Ultrahigh strain and piezoelectric behavior in relaxor based ferroelectric single crystals. *Journal of Applied Physics* **82**, 1804-1811, doi:Doi 10.1063/1.365983 (1997).
78 McLaughlin, E. A., Liu, T. Q. & Lynch, C. S. Relaxor ferroelectric PMN-32%PT crystals under stress and electric field loading: I-32 mode measurements. *Acta Materialia* **52**, 3849-3857, doi:10.1016/j.actamat.2004.04.034 (2004).
79 Li, J.-B. *et al.* Structural transition in unpoled (1−x)PMN–xPT ceramics near the morphotropic boundary. *Journal of Alloys and Compounds* **425**, 373-378, doi:10.1016/j.jallcom.2006.01.041 (2006).
80 Chu, Y. H., Martin, L. W., Holcomb, M. B. & Ramesh, R. Controlling magnetism with multiferroics. *Materials Today* **10**, 16-23, doi:Doi 10.1016/S1369-7021(07)70241-9 (2007).
81 Yang, W., Tan, G. Q., Yan, X., Ren, H. J. & Xia, A. Study on the multiferroic properties of 2-2 type of BiFeO3-CuFe2O4 thin films. *Materials Science in Semiconductor Processing* **53**, 13-17, doi:10.1016/j.mssp.2016.05.019 (2016).
82 Zhou, D. X. *et al.* Electrophoretic deposition of multiferroic BaTiO3/CoFe2O4 bilayer films. *Materials Chemistry and Physics* **127**, 316-321, doi:10.1016/j.matchemphys.2011.02.004 (2011).
83 Zavaliche, F. *et al.* Electric field-induced magnetization switching in epitaxial columnar nanostructures. *Nano letters* **5**, 1793-1796 (2005).
84 Zhao, T. *et al.* Electrical control of antiferromagnetic domains in multiferroic BiFeO3 films at room temperature. *Nat Mater* **5**, 823-829, doi:10.1038/nmat1731 (2006).
85 Seidel, J. *et al.* Conduction at domain walls in oxide multiferroics. *Nat Mater* **8**, 229-234, doi:10.1038/nmat2373 (2009).

86 CDTi. <http://www.cdti.com/spinel/> (
87 Sickafus, K. E., Wills, J. M. & Grimes, N. W. Structure of Spinel. *Journal of the American Ceramic Society* **82**, 3279-3292, doi:10.1111/j.1151-2916.1999.tb02241.x (2004).
88 Hu, G., Choi, J. H., Eom, C. B., Harris, V. G. & Suzuki, Y. Structural tuning of the magnetic behavior in spinel-structure ferrite thin films. *Physical Review B* **62**, R779-R782, doi:DOI 10.1103/PhysRevB.62.R779 (2000).
89 Bian, L. X., Wen, Y. M., Li, P., Gao, Q. L. & Zheng, M. Magnetoelectric transducer with high quality factor for wireless power receiving. *Sensors and Actuators a-Physical* **150**, 207-211, doi:10.1016/j.sna.2009.01.003 (2009).
90 George, S. & Sebastian, M. T. Microwave dielectric properties of novel temperature stable high Q Li2Mg1−xZnxTi3O8 and Li2A1−xCaxTi3O8 (A=Mg, Zn) ceramics. *Journal of the European Ceramic Society* **30**, 2585-2592, doi:10.1016/j.jeurceramsoc.2010.05.010 (2010).
91 Ohnuma, S., Kobayashi, N., Masumoto, T., Mitani, S. & Fujimori, H. Magnetostriction and soft magnetic properties of (Co1−xFex)–Al–O granular films with high electrical resistivity. *Journal of Applied Physics* **85**, 4574-4576, doi:10.1063/1.370412 (1999).
92 Tay, K. W. & Wu, W. F. Pure Oxygen Atmosphere Sintering Behavior and Microwave Dielectric Properties of x(Mg0.96Co0.04)TiO3 - (1-x)SrTiO3 Ceramics. *Iumrs International Conference in Asia 2011* **36**, 462-467, doi:10.1016/j.proeng.2012.03.067 (2012).
93 Kim, D. H., Aimon, N. M., Sun, X. Y. & Ross, C. A. Compositionally Modulated Magnetic Epitaxial Spinel/Perovskite Nanocomposite Thin Films. *Advanced Functional Materials* **24**, 2334-2342, doi:10.1002/adfm.201302844 (2014).
94 Balagurov, A. M., Bobrikov, I. A., Maschenko, M. S., Sangaa, D. & Simkin, V. G. Structural phase transition in CuFe2O4 spinel. *Crystallography Reports* **58**, 710-717, doi:10.1134/S1063774513040044 (2013).
95 Kumar, M. & Yadav, K. L. Synthesis of nanocrystalline xCuFe2O4–(1−x)BiFeO3 magnetoelectric composite by chemical method. *Materials Letters* **61**, 2089-2092, doi:10.1016/j.matlet.2006.08.020 (2007).
96 Hwang, S. O. *et al.* Magnetoelectric properties of magnetic/ferroelectric multilayer thin films. *Journal of the Korean Physical Society* **65**, 229-233, doi:10.3938/jkps.65.229 (2014).
97 Zhang, R. Y. *et al.* High-performance CuFe2O4 epitaxial thin films with enhanced ferromagnetic resonance properties. *Rsc Advances* **6**, 100108-100114, doi:10.1039/c6ra22016a (2016).
98 Arai, K. I. & Tsuya, N. Observation of Magnetostriction in Cu Ferrite Single-Crystals. *Physica Status Solidi B-Basic Research* **66**, 547-552, doi:DOI 10.1002/pssb.2220660217 (1974).
99 Emori, S. *et al.* Coexistence of Low Damping and Strong Magnetoelastic Coupling in Epitaxial Spinel Ferrite Thin Films. *Adv Mater* **29**, doi:10.1002/adma.201701130 (2017).
100 Avci, C. O., Mann, M., Tan, A. J., Gambardella, P. & Beach, G. S. D. A multi-state memory device based on the unidirectional spin Hall magnetoresistance. *Applied Physics Letters* **110**, 203506, doi:Artn 203506 10.1063/1.4983784 (2017).

101 Bedeschi, F. *et al.* A Bipolar-Selected Phase Change Memory Featuring Multi-Level Cell Storage. *Ieee Journal of Solid-State Circuits* **44**, 217-227, doi:10.1109/Jssc.2008.2006439 (2009).
102 Limaye, M. V. *et al.* High coercivity of oleic acid capped CoFe2O4 nanoparticles at room temperature. *J Phys Chem B* **113**, 9070-9076, doi:10.1021/jp810975v (2009).
103 Burr, G. W. *et al.* Recent Progress in Phase-ChangeMemory Technology. *IEEE Journal on Emerging and Selected Topics in Circuits and Systems* **6**, 146-162, doi:10.1109/jetcas.2016.2547718 (2016).
104 Buehler. <https://www.buehler.com/minimet-1000-semi-automatic-grinder-polisher.php> (
105 Chan, N.-y. *Study of barium strontium zirconate titanate thin films and their microwave device applications*, The Hong Kong Polytechnic University, (2010).
106 Li, L. *et al.* Direct Observation of Magnetic Field Induced Ferroelectric Domain Evolution in Self-Assembled Quasi (0-3) BiFeO3-CoFe2O4 Thin Films. *ACS Appl Mater Interfaces* **8**, 442-448, doi:10.1021/acsami.5b09265 (2016).
107 Giessibl, F. J. Advances in atomic force microscopy. *Reviews of Modern Physics* **75**, 949-983, doi:DOI 10.1103/RevModPhys.75.949 (2003).
108 Hartmann, U. Magnetic force microscopy. *Annual review of materials science* **29**, 53-87 (1999).
109 Idigoras, O. *et al.* FEBID fabrication and magnetic characterization of individual nano-scale and micro-scale Co structures. *Nanofabrication* **1**, 23-34, doi:10.2478/nanofab-2014-0003 (2014).
110 Cullity, B. D. & Stock, S. R. *Elements of X-ray Diffraction*. (Pearson Education, 2014).
111 Dodd, J. L., Yazami, R. & Fultz, B. Phase diagram of Li(x)FePO4. *Electrochem Solid St* **9**, A151-A155, doi:10.1149/1.2164548 (2006).
112 Foner, S. Versatile and sensitive vibrating ‐ sample magnetometer. *Review of Scientific Instruments* **30**, 548-557 (1959).
113 Rafique, M. *Study of the Magnetoelectric Properties of Multiferroic Thin Films and Composites for Device Applications*, COMSATS Institute of Information Technology, Islamabad-Pakistan, (2014).
114 Wang, Z. (ACS Publications, 2000).
115 Yang, J. J. *et al.* Electric field manipulation of magnetization at room temperature in multiferroic CoFe2O4/Pb(Mg1/3Nb2/3)0.7Ti0.3O3 heterostructures. *Applied Physics Letters* **94**, 212504, doi:10.1063/1.3143622 (2009).
116 Dix, N. *et al.* On the strain coupling across vertical interfaces of switchable BiFeO3–CoFe2O4 multiferroic nanostructures. *Applied Physics Letters* **95**, 062907, doi:10.1063/1.3204464 (2009).
117 Li, Y. X. *et al.* Controlled growth of epitaxial BiFeO3 films using self-assembled BiFeO3-CoFe2O4 multiferroic heterostructures as a template. *Applied Physics Letters* **101**, 022905, doi:10.1063/1.4734508 (2012).
118 Zavaliche, F. *et al.* Electric field-induced magnetization switching in epitaxial columnar nanostructures. *Nano Lett* **5**, 1793-1796, doi:10.1021/nl051406i (2005).
119 Levin, I., Li, J. H., Slutsker, J. & Roytburd, A. L. Design of self-assembled multiferroic nanostructures in epitaxial films. *Advanced Materials* **18**, 2044-+, doi:10.1002/adma.200600288 (2006).

120 Wang, Z. G. *et al.* Electrical and thermal control of magnetic coercive field in ferromagnetic/ferroelectric heterostructures. *Physical Review B* **89**, doi:ARTN 035118 10.1103/PhysRevB.89.035118 (2014).
121 Zavaliche, F. *et al.* Electrically assisted magnetic recording in multiferroic nanostructures. *Nano Lett* **7**, 1586-1590, doi:10.1021/nl070465o (2007).
122 Zhao, T. *et al.* Nanoscale x-ray magnetic circular dichroism probing of electric-field-induced magnetic switching in multiferroic nanostructures. *Applied Physics Letters* **90**, 123104, doi:10.1063/1.2714201 (2007).
123 Wang, J. *et al.* Switchable voltage control of the magnetic coercive field via magnetoelectric effect. *Journal of Applied Physics* **110**, 043919, doi:10.1063/1.3626748 (2011).
124 Eerenstein, W., Wiora, M., Prieto, J. L., Scott, J. F. & Mathur, N. D. Giant sharp and persistent converse magnetoelectric effects in multiferroic epitaxial heterostructures. *Nat Mater* **6**, 348-351, doi:10.1038/nmat1886 (2007).
125 Liu, Y. *et al.* Electric-Field Control of Magnetism in Co40Fe40B20/(1-x)Pb(Mg1/3Nb2/3)O3-xPbTiO3 Multiferroic Heterostructures with Different Ferroelectric Phases. *ACS Appl Mater Interfaces* **8**, 3784-3791, doi:10.1021/acsami.5b10233 (2016).
126 Wongmaneerung, R., Guo, R., Bhalla, A., Yimnirun, R. & Ananta, S. Thermal expansion properties of PMN–PT ceramics. *Journal of Alloys and Compounds* **461**, 565-569, doi:10.1016/j.jallcom.2007.07.086 (2008).
127 Fritsch, D. & Ederer, C. First-principles calculation of magnetoelastic coefficients and magnetostriction in the spinel ferrites CoFe$\{\}_\{2\}$O$\{\}_\{4\}$ and NiFe$\{\}_\{2\}$O$\{\}_\{4\}$. *Physical Review B* **86**, 014406 (2012).
128 Fritsch, D. & Ederer, C. First-principles calculation of magnetoelastic coefficients and magnetostriction in the spinel ferrites CoFe 2 O 4 and NiFe 2 O 4. *Physical Review B* **86**, 014406 (2012).
129 Su, H. *et al.* Electric-field tuning of non-volatile magnetization modulation in NiZn ferrite/PZT multiferroic heterostructure. *Journal of Alloys and Compounds* **695**, 3722-3726, doi:10.1016/j.jallcom.2016.11.325 (2017).
130 Weisheit, M. *et al.* Electric field-induced modification of magnetism in thin-film ferromagnets. *Science* **315**, 349-351, doi:10.1126/science.1136629 (2007).
131 Chinnasamy, C. N. *et al.* Unusually high coercivity and critical single-domain size of nearly monodispersed CoFe2O4 nanoparticles. *Applied Physics Letters* **83**, 2862-2864, doi:10.1063/1.1616655 (2003).
132 Prince, E. & Treuting, R. G. The Structure of Tetragonal Copper Ferrite. *Acta Crystallographica* **9**, 1025-1028, doi:Doi 10.1107/S0365110x56002977 (1956).
133 Goya, G. F., Rechenberg, H. R. & Jiang, J. Z. Structural and magnetic properties of ball milled copper ferrite. *Journal of Applied Physics* **84**, 1101-1108, doi:Doi 10.1063/1.368109 (1998).
134 Kim, D. H. *et al.* Integration of Self-Assembled Epitaxial BiFeO3-CoFe2O4Multiferroic Nanocomposites on Silicon Substrates. *Advanced Functional Materials* **24**, 5889-5896, doi:10.1002/adfm.201401458 (2014).
135 Mark, C., Martin, T. D. & Ekhard, K. H. S. Trapping of oxygen vacancies on twin walls of CaTiO 3 : a computer simulation study. *Journal of Physics: Condensed Matter* **15**, 2301 (2003).

136 Viehland, D. D. & Salje, E. K. H. Domain boundary-dominated systems: adaptive structures and functional twin boundaries. *Advances in Physics* **63**, 267-326, doi:10.1080/00018732.2014.974304 (2014).
137 Bibes, M. & Barthelemy, A. Multiferroics: towards a magnetoelectric memory. *Nat Mater* **7**, 425-426, doi:10.1038/nmat2189 (2008).
138 Lim, L., Shanthi, M., Rajan, K. K. & Lim, C. Flux growth of high-homogeneity PMN–PT single crystals and their property characterization. *Journal of crystal growth* **282**, 330-342 (2005).
139 Soares, B. F., Jonsson, F. & Zheludev, N. I. All-optical phase-change memory in a single gallium nanoparticle. *Phys Rev Lett* **98**, 153905, doi:10.1103/PhysRevLett.98.153905 (2007).
140 Zheludev, N. I. & Kivshar, Y. S. From metamaterials to metadevices. *Nat Mater* **11**, 917-924, doi:10.1038/nmat3431 (2012).
141 Shen, J. *et al.* A multilevel nonvolatile magnetoelectric memory. *Sci Rep* **6**, 34473, doi:10.1038/srep34473 (2016).
142 Yao, Y. P. *et al.* Multi-state resistive switching memory with secure information storage in Au/BiFe0.95Mn0.05O3/La5/8Ca3/8MnO3 heterostructure. *Applied Physics Letters* **100**, 193504, doi:Artn 193504 10.1063/1.4714514 (2012).
143 Brivio, S., Petti, D., Bertacco, R. & Cezar, J. C. Electric field control of magnetic anisotropies and magnetic coercivity in Fe/BaTiO3(001) heterostructures. *Applied Physics Letters* **98**, 092505, doi:Artn 092505 10.1063/1.3554432 (2011).
144 Geprags, S., Brandlmaier, A., Opel, M., Gross, R. & Goennenwein, S. T. B. Electric field controlled manipulation of the magnetization in Ni/BaTiO3 hybrid structures. *Applied Physics Letters* **96**, 142509, doi:Artn 142509 10.1063/1.3377923 (2010).
145 Venkataiah, G., Shirahata, Y., Itoh, M. & Taniyama, T. Manipulation of magnetic coercivity of Fe film in Fe/BaTiO3 heterostructure by electric field. *Applied Physics Letters* **99**, 102506, doi:10.1063/1.3628464 (2011).
146 Zhang, W. R. *et al.* Strain relaxation and enhanced perpendicular magnetic anisotropy in BiFeO3:CoFe2O4 vertically aligned nanocomposite thin films. *Applied Physics Letters* **104**, 062402, doi:Artn 062402 10.1063/1.4864405 (2014).
147 Rafique, M., Herklotz, A., Dorr, K. & Manzoor, S. Giant room temperature magnetoelectric response in strain controlled nanocomposites. *Applied Physics Letters* **110**, 202902, doi:Artn 202902 10.1063/1.4983357 (2017).
148 Beleggia, M., De Graef, M. & Millev, Y. T. The equivalent ellipsoid of a magnetized body. *Journal of Physics D-Applied Physics* **39**, 891-899, doi:10.1088/0022-3727/39/5/001 (2006).
149 Bai, F. *et al.* X-ray and neutron diffraction investigations of the structural phase transformation sequence under electric field in 0.7 Pb (Mg 1 ／ 3 Nb 2 ／ 3)-0.3 PbTiO 3 crystal. *Journal of Applied Physics* **96**, 1620-1627 (2004).
150 Zhang, S. & Li, F. High performance ferroelectric relaxor-PbTiO3 single crystals: Status and perspective. *Journal of Applied Physics* **111**, 2 (2012).
151 Gao, M., Tang, X., Dai, S., Li, J. & Viehland, D. Depth dependent ferroelectric to incommensurate/commensurate antiferroelectric phase transition in epitaxial lanthanum modified lead zirconate titanate thin films. *Applied Physics Letters* **115**, 072901, doi:10.1063/1.5113720 (2019).

152 Leung, C. M. *et al.* Enhanced stability of magnetoelectric gyrators under high power conditions. *Applied Physics Letters* **111**, 182901 (2017).
153 Leung, C. M. *et al.* Stability enhancement of yttrium substituted nickel zinc ferrite/PZT magnetoelectric gyrators under high power conditions. *Applied Physics Letters* **112**, 242901 (2018).
154 Leung, C. M. *et al.* A Highly Efficient Self‐Biased Nickel‐Zinc Ferrite/Metglas/PZT Magnetoelectric Gyrator. *physica status solidi (RRL) ‐Rapid Research Letters* **12**, 1800043 (2018).
155 Leung, C. M. *et al.* A dual-output magnetoelectric gyrator. *Journal of Physics D: Applied Physics* **52**, 065003 (2018).
156 Tang, X. *et al.* Nanostructure-enhanced magnetoelectric/magnetostrictive properties and reduced losses in self-assembled epitaxial CuFe2O4–BiFeO3 layers on Pb(Mg1/3Nb2/3)O3–33at%PbTiO3 crystals. *Journal of the American Ceramic Society* **0**, 1-11, doi:doi:10.1111/jace.16387 (2019).
157 Tang, X. *et al.* Non-volatility using materials with only volatile properties: Vertically integrated magnetoelectric heterostructures and their potential for multi-level-cell devices. *Applied Physics Letters* **114**, 242903, doi:10.1063/1.5094430 (2019).
158 Gao, M. *et al.* Apparent phase stability and domain distribution of PMN-30PT single crystals with nanograted Au/MnOx electrodes. *Acta Materialia* **169**, 28-35, doi:https://doi.org/10.1016/j.actamat.2019.02.039 (2019).
159 Liu, H. J. *et al.* Large Magnetoresistance in Magnetically Coupled SrRuO3‐CoFe2O4 Self‐Assembled Nanostructures. *Advanced Materials* **25**, 4753-4759 (2013).
160 Chang, W.-Y. *et al.* Patterned nano-domains in PMN-PT single crystals. *Acta Materialia* **143**, 166-173 (2018).
161 Liu, H.-J. *et al.* Epitaxial photostriction–magnetostriction coupled self-assembled nanostructures. *Acs Nano* **6**, 6952-6959 (2012).
162 Zhang, S. *et al.* Advantages and challenges of relaxor-PbTiO3 ferroelectric crystals for electroacoustic transducers–A review. *Progress in materials science* **68**, 1-66 (2015).
163 Yamamoto, N., Itsumi, K. & Hosono, Y. Effects of manganese oxides/gold composite electrode on piezoelectric properties of lead magnesium niobate titanate single crystal. *Japanese Journal of Applied Physics* **50**, 09NC05 (2011).